The Circum- and Intergalactic Medium and its Connection to the Large Scale Structure in the Nearby Universe

Sietske Bouma
Universität Potsdam

Supervisor: Prof. Dr. Philipp Richter

Dissertation

zur Erlangung des akademischen Grades
doctor rerum naturalium (Dr. rer. nat.)
in der Wissenschaftsdisziplin Physik

Eingereicht an der Mathematisch-Naturwissenschaftlichen Fakultät
Institut für Physik und Astronomie
der Universität Potsdam

Potsdam, 16.09.2021

Supervisor: Prof. Dr. Philipp Richter/ Prof. Dr. Lutz Wisotzki

Referee 1: Prof. Dr. Philipp Richter
Universität Potsdam

Referee 2: Prof. Dr. Lutz Wisotzki
Leibniz-Institut für Astrophysik Potsdam

Referee 3: Prof. Dr. Jane Charlton
Pennsylvania State University

Published online on the
Publication Server of the University of Potsdam:
https://doi.org/10.25932/publishup-52085
https://nbn-resolving.org/urn:nbn:de:kobv:517-opus4-520852

Contents

Summary

The majority of baryons in the Universe is believed to reside not in collapsed structures like galaxies, but in the intergalactic medium (IGM). This makes the IGM an important component in understanding cosmological structure formation. It is expected to trace the same dark matter distribution as galaxies, forming structures like filaments and clusters. However, whereas galaxies can be observed to be arranged along these large-scale structures, the spatial distribution of the diffuse IGM is not as easily unveiled. Absorption line studies of quasar (QSO) spectra can help with mapping the IGM, as well as the boundary layer between IGM and galaxies: the circumgalactic medium (CGM). Despite these studies, many open questions yet remain. By studying gas in the Local Group, as well as in the IGM, this study aims to get a better understanding of how the gas is linked to the large-scale structure of the local Universe and the galaxies residing in that structure.

Chapter 1 gives an introduction to the CGM and IGM, while the methods used in this study are explained in Chapter 2. Chapter 3 starts on a relatively small cosmological scale, namely that of our Local Group, which includes i.a. the Milky Way (MW) and the Andromeda galaxy (M31). Within the CGM of the MW, there exist denser clouds, some of which are infalling while others are moving away from the Galactic disc. To study these CGM clouds, 29 QSO spectra obtained with the Cosmic Origins Spectrograph (COS) aboard the *Hubble Space Telescope* (*HST*) were analysed. Abundances of Si II, Si III, Si IV, C II, and C IV were measured for 69 HVCs belonging to two samples: one in the direction of the LG's barycentre and the other in the anti-barycentre direction. Their velocities range from $-100 \lesssim v_{\rm LSR} \lesssim -400$ km s^{-1} for the barycentre sample and between $+100 \lesssim v_{\rm LSR} \lesssim +300$ km s^{-1} for the anti-barycentre sample. By using Cloudy models, these data could then be used to derive gas volume densities for the HVCs. Because of the relationship between density and pressure of the ambient medium, which is in turn determined by the Galactic radiation field, the distances of the HVCs could be estimated. From this, a subsample of absorbers located in the direction of M31 was found to exist outside of the MW's virial radius, their low densities ($\log n_{\rm H} \leq -3.54$) making it likely for them to be part of the gas in between the MW and M31. No such low-density absorbers were found in the anti-barycentre sample. Our results thus hint at gas following the dark matter potential, which would be deeper between the MW and M31 as they are by far the most massive members of the LG.

From this bridge of gas in the LG, this study zooms out to the large-scale structure of the local Universe ($z = 0$) in Chapter 4. A combination of galaxy data from the V8k catalogue and QSO spectra from COS was used to study the relation between the galaxies tracing large-scale filaments and the gas existing outside of those galaxies. Several filaments in the local Universe have been defined in Courtois et al. (2013) and this study used the galaxies assigned to each filament to establish filament axes. A total of 587 Lyman α (Lyα) absorbers were found in the 302 QSO spectra in the velocity range $1070 - 6700$ km s^{-1}. After selecting sightlines passing through or close to these filaments, model spectra were made for 91 sightlines and 215 (227) Lyα absorbers (components) were measured in this sample. Since the gas tracing the filaments is expected to have velocities similar to those of the galaxies, the velocity gradient along each filament was calculated and 74 absorbers were found within 1000 km s^{-1} of the nearest filament segment.

In order to find whether the absorbers are more tied to galaxies or to the large-scale structure, equivalent widths of the Lyα absorbers were plotted against both galaxy and filament impact parameters. While stronger absorbers do tend to be closer to either galaxies or filaments, there is a large scatter in this relation. Despite this large scatter, this study found that the absorbers do not follow a random distribution either. They cluster less strongly around filaments than galaxies, but stronger than random distributions, as confirmed by a Kolmogorov-Smirnov test.

Furthermore, the column density distribution function found in this study has a slope of $-\beta = -1.63 \pm 0.12$ for the total sample and $-\beta = -1.47 \pm 0.24$ for the absorbers within 1000 km s^{-1} of a filament. The shallower slope for the latter subsample could indicate an excess of denser absorbers within the filament, but they are consistent within errors. These values are in agreement with values found in e.g. Lehner et al. (2007); Danforth et al. (2016).

The picture that emerges from this study regarding the relation between the IGM and the large-scale structure in the local Universe fits with what is found in other studies: while at least part of the gas traces the same filamentary structure as galaxies, the relation is complex. This study has shown that by taking a large sample of sightlines and comparing the data gathered from those with galaxy data, it is possible to study the gaseous large-scale structure. This approach can be used in the future together with simulations to get a better understanding of structure formation and evolution in the Universe.

Zusammenfassung

Sterne und Galaxien, die das Universum füllen, haben sich alle aus Gas gebildet. Bis heute bleibt der Großteil der baryonischen Materie im Universum im gasförmigen Zustand, und nur ein geringer Anteil davon ist kollabiert, um Sterne und Galaxien entstehen zu lassen. Der Gravitationskollaps folgt den Potentialtöpfen der Dunklen Materie, wodurch sich die großräumige Struktur (large-scale structures, LSS) des Universums formt. Die Galaxien innerhalb dieser Struktur ordnen sich entlang der Schichten, Filamenten und um die Knotenpunkte, wobei die Regionen niedriger Dichte (Voids) dazwischen liegen. Das diffuse Gas füllt diese Strukturen ebenfalls und stellt somit ein Reservoir der baryonischen Materie den Galaxien für die weitere Sternbildung zur Verfügung. Galaxien wiederum reichen das umgebende diffuse Gas an. Darum spielt das Gas um und zwischen Galaxien, das zirkum- bzw. intergalaktisches Medium (circum-/intergalactic medium, CGM/IGM), eine wichtige Rolle in der Entstehung und Entwicklung der Galaxien und LSS im Universum. Ziel dieses Promotionsprojektes ist es, ein besseres Verständnis über die Zusammenhänge zwischen dem intergalaktischen Gas und LSS mit darin befindlichen Galaxien im lokalen Universum zu erhalten.

Die Verteilung de Gases im IGM ist aufgrund der diffusen Beschaffenheit schwer nachzuweisen. Eine der Möglichkeiten es zu untersuchen, ist die Betrachtung der Absorptionsmerkmale in den Spektren der weitentfernten Quasare (QSOs). IGM, das vom Licht dieser QSOs auf dem Weg zum Beobachter durchquert wird, hinterlässt im Spektrum die charakteristischen Absoprtionslinien. Wir analysieren in diesem Promotionsprojekt eine große Anzahl von QSO-Spektren, die vom Cosmic Origin Spectrograph an Bord des Hubble-Weltraumteleskop stammen, um den physikalischen Zustand des intervenierenden intergalaktischen und zirkumgalaktischen Gas im nahen Universum zu untersuchen.

Im ersten Teil dieser Dissertation untersuchen wir anhand der sogenannten Hochgeschwindigkeitswolken (high-velocity clouds, HVCs) das CGM um die Milchstraße in Richtung des Baryzentrums und Anti-Baryzentrums der Galaxien der Lokalen Gruppe (LG). Die HVCs haben Radialgeschwindigkeiten von über 80 $\mathrm{km\,s^{-1}}$ und können sehr unterschiedliche Herkunft haben. Wir vermessen die Häufigkeiten verschiedener Ionen von Si und C für 69 HVCs sowie deren Kinematik. Daraus werden physikalische Eigenschaften der Wolken abgeleitet, die auf eine Teilstichprobe besonders interessanter Absorber in Richtung des Baryzentrums hinweisen. Diese Teilstichprobe besteht aus HVCs mit sehr geringen Gasdichten (log n(H) < -3.54), was darauf hindeutet, dass diese Wolken sich höchstwahrscheinlich außerhalb des Virialradius der Milchstraße in der gasförmigen Brücke befinden, die die Milchstraße und die Nachbargalaxie M31 verbindet.

Ausgehend von dieser gasförmigen Brücke in unserer LG zoomen wir im zweiten Teil des Dissertation heraus, um einen Überblick über die Gasverteilung im lokalen Universum auf größeren Skalen zu erhalten. Wir analysieren die Lyman-α (Lyα) -Absorption des neutralen Wasserstoffs (H I) in 302 QSO-Spektren aus allen Himmelsrichtungen und kombinieren diese Daten mit denen von Galaxiefilamenten, die im V8k Katalog von Courtois et al. (2013) identifiziert wurden. Von den 587 H I Lyα-Absorptionssystemen befinden sich 215 in der Nähe von Galaxiefilamenten. Die stärkeren Absorber befinden sich häufig in der Nähe von Galaxien oder näher an den Mittelachsen der Filamente, aber diese Beziehung zeigt eine große Streuung. Die Lyα-Absorber neigen dazu, sich stärker um die Filamentachsen zu gruppieren im Vergleich zu einer zufälligen Population von Absorbern, wenn auch nicht so stark wie Galaxien. Dies weist darauf hin, dass die Lyα-Absorber zwar der großräumigen Struktur folgen, jedoch auf ihre eigene Weise. Schließlich zeigt eine statistische Analyse der Absorberstärken, dass sich die Verteilung der H I-Säulendichten von Region außerhalb zu Regionen innerhalb der Filamente ändert, was die grundsätzlich höhere Dichte der Materie in letzteren widerspiegelt.

Das Gesamtergebnis dieser Dissertation stimmt gut mit den Ergebnissen anderer Studien überein: auch wenn ein Teil des intergalaktischen Gases denselben kosmologischen Filamentstrukturen wie Galaxien folgt, bleibt die Beziehung zwischen Gas, Galaxien und großräumigen Struktur komplex. Die hochauflösende kosmologische Simulationen zusammen mit den zukünftigen Beobachtungen werden helfen diesen Zusammenhang besser zu verstehen.

1 Introduction

A hint of gold where the moon will be;
Through the flocking clouds just a star or two

— **Angelina Weld Grimké**
(The Want of You)

The multitude of stars piercing the night sky make for an awe-inspiring view, one that becomes even more impressive when considering there are so many more things hidden in the dark patches between those shining points. Stars only form the first clues to unravelling the mysteries of the Universe. More difficult to observe, but no less important is the gas that resides in between stars and galaxies. The majority of baryons is thought to reside in this intergalactic medium (IGM), which is connected to galaxies through the circumgalactic medium (CGM).

In order to understand the connection between the IGM/CGM and galaxies, we have to look back to the early days of the Universe, to the point where there were not yet any stars or galaxies, just gas. Some of this gas would form the luminous structures we can observe today, while the rest remains as diffuse gas scattered around and in between galaxies. Models and observations supplement each other in obtaining the complete picture of how the Universe evolves and will continue to evolve.

1.1 Structure formation

The starting point for studying the evolution of the Universe is the Big Bang. The idea of the Universe having a starting point, instead of being static, emerged at the beginning of the 20th century. From measuring the distances and velocities of galaxies ("nebulae" at the time), Hubble concluded that the Universe was expanding (Hubble 1929). This theory of an evolving universe was not readily accepted, however. A competing model was the steady-state model of which Bondi, Gold and Hoyle were influential proponents (see e.g. Bondi 1952). As the name implies, the steady-state model assumes the large scale structure of the universe remains constant, despite the expansion of the universe. To keep the overall density constant, matter must be created continuously. Using this model as a starting point, Sciama (1955) postulated a theory that new galaxies could form from density perturbation of the IGM caused by pre-existing galaxies. In the same paper,

Sciama criticised Gamow's theory that the Universe started out hot and dense and would cool as it expended, allowing protogalaxies to form (Gamow 1953).

Some ten years later, however, evidence for Gamow's idea of a hot early universe was found in the form of a thermal radiation background: the Cosmic Microwave Background (CMB, Penzias & Wilson 1965). This radiation is a leftover from the epoch of recombination. Before this time, free electrons and protons made up a plasma that continuously scattered photons, making the universe opaque. When the universe cooled enough to form neutral hydrogen atoms, photons could travel for much larger distances without interacting and these photons give rise to the CMB which we can measure to this day.

Following this discovery, Peebles studied the influence of this thermal radiation on the formation of galaxies and found that the CMB would prevent gravitationally bound systems from forming until a certain critical epoch (Peebles 1965). According to his calculations, gas clouds of the order of 10^7 $M_\odot$ would form and cluster together because of gravitational interaction and continue to form galaxies. Density fluctuations in the early Universe would function as "seeds" from which those clouds could form with the passing of time (e.g. Peebles 1967). This process of forming galaxies from small initial perturbations is the so-called bottom-up model for galaxy formation. However, while the link between the evolution of the Universe and galaxy formation was firmly established, there was no consensus yet that this was the correct evolutionary path for the formation of galaxies.

Competing with the bottom-up scenario was the top-down model, in which condensations occur on a large scale first. Eggen et al. (1962) studied the kinematics and combined this with metallicity derived from measurements of the stars in the ultraviolet (UV) and blue parts of the spectrum. They found that the oldest, most metal-poor stars, were found at different heights above the galactic plane, while the younger stars were all formed near the plane. From this, they concluded that those old stars formed from gas that was collapsing onto the plane, at a time when the galaxy was not yet in its current equilibrium state. The galaxy thus started out as a larger protogalaxy which then collapsed, with smaller condensations occurring forming globular clusters. This model was further supported when Silk (1968) discovered the "Silk damping" effect. Silk concluded that primordial fluctuations below a certain amplitude would be optically thick and radiative diffusion would dampen them on relatively short timescales. This meant that the first galaxies would have to have a mass of at least $5 \cdot 10^{11}$ $M_\odot$ as smaller structures would not have survived long enough to form galaxies.

Eventually, a strong case for the bottom-up, or hierarchical, model came from Press & Schechter (1974). In their model, small condensations cluster into larger structures. This model only works for purely self-gravitating particles – dark matter – however. For baryonic matter, other physical processes have to be taken into account.

A model that combines both dark matter and baryons was proposed by White & Rees (1978). White and Reese base their model on the findings that, on large scales, the distribution of galaxies can be explained by models that only include gravitational effects, while individual galaxy characteristics like mass and size cannot be reproduced by dissipationless models. Their model starts with hierarchical clustering of dark matter, where small perturbations grow as time goes on. This creates potential wells within which baryons accumulate. The gas clouds that are formed this way will either remain as clouds if their characteristic cooling time is larger than the Hubble time, reach

hydrostatic equilibrium, or dissipate their energy and collapse. The last scenario is only possible if the characteristic cooling time is lower than both the Hubble time and the dynamical time. First to form will be low-mass systems consisting of luminous stars. These small systems will merge to form larger galaxies, with residual gas collapsing to form the inner parts of galaxies. They argue that about half of the residual gas can be found in luminous galaxies, while the other half is in the IGM. The predictions derived from simulations using this hierarchical clustering model are in reasonable agreement with observed galaxy properties, like luminosity, gas content and star formation rate (e.g. Kauffmann et al. 1993; Baugh et al. 1998). Different formation histories give rise to various types of galaxies. For example, galaxy discs appear to be the result of cool gas being deposited at the centre of dark matter haloes, while the bulge component forms when this gas is stirred during merger events (Steinmetz & Navarro 2002).

Whereas White & Rees (1978) describe a galaxy formation model using so-called hot-mode accretion, where gas is shock heated to the virial temperature before cooling down and collapsing, Kereš et al. (2005) show that for lower mass galaxies (below baryonic mass of $\sim 10^{10.3}$ $M_\odot$), another accretion path might be more important. In their cold-mode accretion, gas is never shock-heated to high temperatures, but instead radiates its gravitational energy away at lower temperatures. This gas is accreted from filamentary structures extending beyond the galaxy's virial radius. Since it is the dominant accretion path for low mass galaxies, it is important mainly at high redshift. At lower redshift, the more massive galaxies accrete gas via hot-mode accretion. These models already show how galaxies and their surrounding gas are intertwined.

With the aid of galaxy catalogues, it has become possible to study not only how galaxies have formed from primordial gas, but also how those galaxies are clustered together in large-scale structures like filaments and sheets. While the dark matter creating the initial potential wells cannot be detected directly, it can be studied by looking at the baryonic matter tracing its structures. Gas will flow into those potential wells and part of this gas will collapse to form (proto)galaxies, which follow the structures outlined by dark matter. The densest regions will form galaxy clusters, while matter will flow away from underdense regions, creating voids that contain few galaxies. Gas will collapse if the pressure of the cloud can no longer withstand gravitational collapse, so that the cloud is no longer in hydrostatic equilibrium. Heating and cooling processes as well as gravitational interactions play a role in the state of baryonic matter, which is why it is of interest to study gas in different environments. The Millennium II simulation is one of several projects to model the formation of structure in the Universe. Fig. 1.1 shows results from this simulation at different scales, going from filaments and voids to galaxy clusters and eventually individual galaxies.

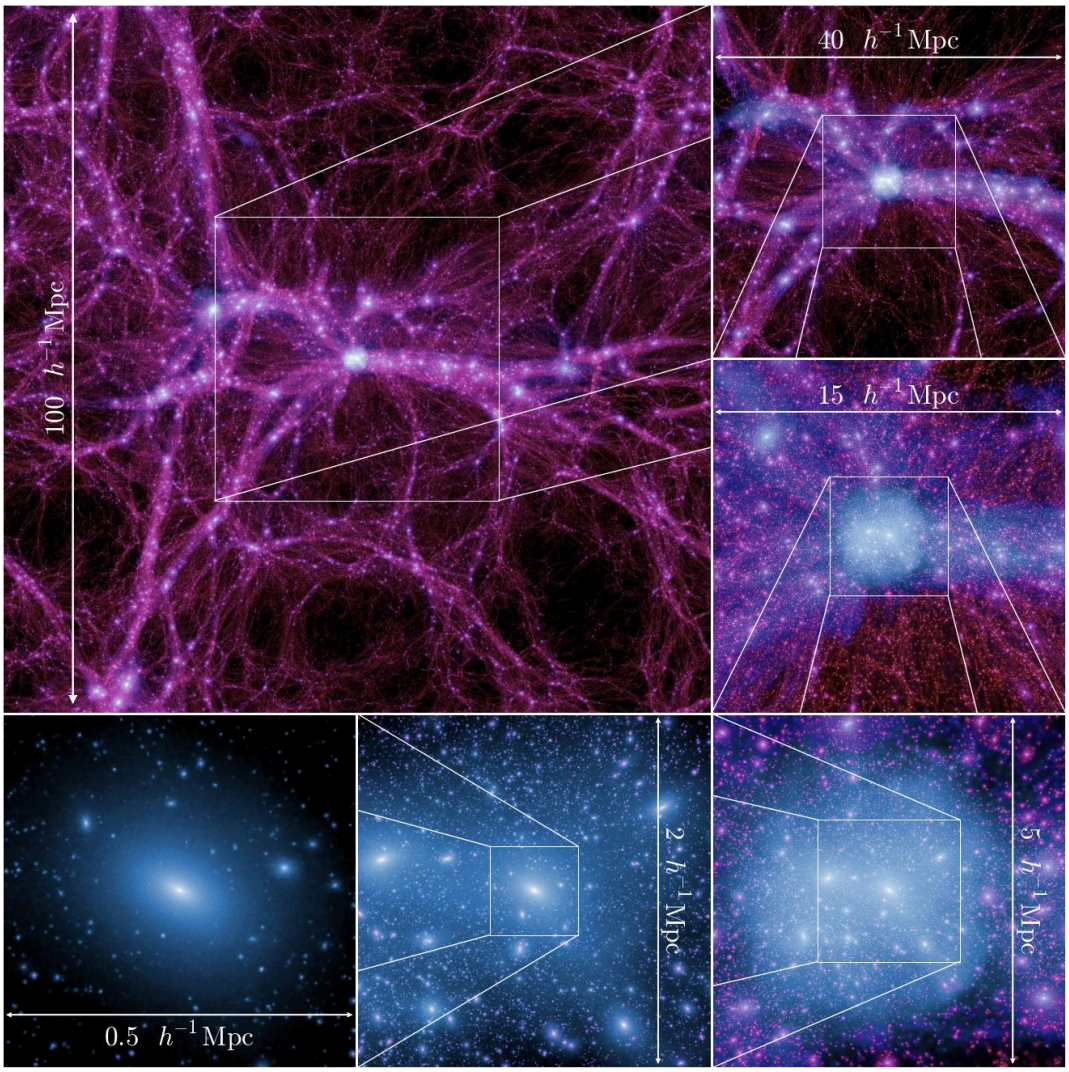

Figure 1.1 — Large-scale structure of the dark matter distribution of the Universe as seen in the Millennium II simulation (Fig. 1, Boylan-Kolchin et al. 2009).

1.2 The IGM as a reservoir of baryons

While the model from White & Rees (1978) shows roughly where the baryons in the Universe went, the exact number of baryons present in galaxies, in the CGM and in the IGM is a matter of debate. Persic & Salucci (1992) concluded that less than 10% of the baryons predicted by primordial nucleosynthesis was in the form of galaxies and hot gas in galaxy groups and clusters. The remainder of baryons has to be found somewhere else. This is known as the missing baryon problem. Other baryon reservoirs could, for example, be the halos of spiral galaxies, or the ionised IGM. Similarly, Fukugita et al. (1998) showed that only a small fraction of baryons (~17%) is in stars and stellar remnants. More recently, Shull et al. (2012) provided a baryon census taking into account not only galaxies and the CGM, but also the warm-hot IGM (WHIM) and the Lyα forest. Summarising different studies, they find that some $60-70\%$ of baryons can be found in various states of the IGM. This WHIM (10^5-10^7 K) is difficult to detect compared to hot and cold components. It is usually too diffuse to emit in optical (21 cm) emission like cold gas, while not being hot and dense enough to emit in X-ray, like the hot gas at the centre of clusters. This will be discussed in more detail later in this Section.

The fraction of baryons in the different IGM phases changes over time, as matter collapses into large-scale structures like filaments and on a smaller scale into galaxies. This has been visualised by different cosmological simulations. Fig. 1.2 is from the Illustris simulation (Haider et al. 2016) and shows that the fraction of baryons in diffuse, photoionised intergalactic gas decreases over time, as expected. The fraction in the WHIM increases rapidly after $z\sim2$ until a fraction of ~0.55 at $z=0$, making it the largest reservoir of baryons at the current time. The fraction of gas condensed into galaxy halos at $z=0$ is ~0.2. Over time, diffuse gas can be seen to collapse into galaxies and stars, but the increasing baryonic mass fractions of the WHIM and hot gas ($T>10^7$ K) show that heating processes also start to play an important role.

The first important reservoir of baryons in the IGM are photoionised Lyα absorbers at T $\lesssim 10^4$ K. They have column densities $\log N(\mathrm{H\,I}) \lesssim 10^{16}$ cm^{-2}, with the majority of absorbers having low densities, $\log N(\mathrm{H\,I}) \leq 10^{14}$ cm^{-2} (Lehner et al. 2007). The first Lyα absorption lines were discovered in a spectra of quasars (QSOs) at $z>2$ (Gunn & Peterson 1965; Lynds 1971), but it took several more years before Lyα absorption lines from gas at low-z could be measured, due to their location in the far-ultraviolet (FUV). With the *Hubble Space Telescope* (*HST*), it became possible to trace Lyα at low-z. It was found that the number of Lyα absorbers at low-z exceeded the number expected from extrapolation from high-z (e.g. Weymann et al. 1998). This break in the number of absorbers as a function of redshift bin seems to occur at $z=1.7$ and could be due to two different populations of Lyα absorbers being dominant at different redshifts (Davé et al. 1999). Several works (e.g. Morris et al. 1993; Bahcall et al. 1996) made

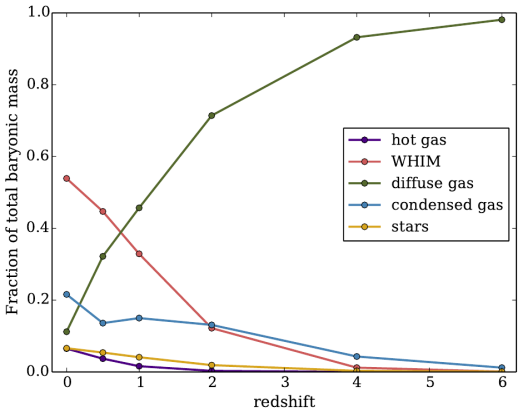

Figure 1.2 — Baryonic mass distribution function as a function of redshift as found in the Illustris simulation (Fig. 15, Haider et al. 2016).

a distinction between these two types, stating that the higher equivalent width (EW) absorbers dominant at low-z are closely associated with galaxies and slowly evolving, while the absorbers that dominate at high-z are rapidly evolving and are not closely associated with galaxies. Not all Lyα absorbers at low-z are associated with galaxies, however. Morris et al. (1993) found that Lyα absorbers clustered less strongly around galaxies than galaxies clustered among themselves. They concluded that, even at low-z, there was no close correlation between Lyα absorbers and galaxies. This could be explained by the absorbers being a mix of the two different populations, thus showing clustering that is more correlated to galaxies than a random population would be, but not as strongly correlated as galaxies cluster among each other.

Some studies, however, do not support the idea of distinct populations of Lyα absorbers. Penton et al. (2000), for example, concluded that their data did not support a different evolution with redshift between high and low EW absorbers. They estimate the total number of baryons found in the Lyα forest at low-z to be around 20%. Lehner et al. (2007) conclude this may even be 30% and that at least 20% of baryons may be found in the highly ionised IGM as broad Lyα absorbers.

Another reservoir of baryons at low-z is the WHIM. As filaments and sheets form larger structures, accretion shocks heat the IGM to temperatures between 10^5 to 10^7 K. Important tracers of the WHIM are highly ionised states of N, O and Ne, as well as broad Lyα absorbers (BLAs). Absorption lines with Doppler-parameters $b > 40$ km s^{-1} trace gas with T > 10^5 K, but these broad absorbers are difficult to detect because of blending, not a high enough signal-to-noise and uncertainties in the placement of the continuum (Richter et al. 2004). Furthermore, the measured b parameter of an absorption line is no more than an upper limit on the thermal line width, as there are non-thermal processes that can also play a role in the broadening. These difficulties in detection and analysis lead to large uncertainties on the total number of baryons present in the WHIM. An analysis of O VI and BLAs led Danforth et al. (2010) to conclude that about 20% of the baryons at low-z was in the WHIM (see also Tilton et al. 2012; Kovács et al. 2019). Simulations (Davé et al. 2001; Martizzi et al. 2019) estimate this fraction to be between 40 and 50%.

After taking different reservoirs of baryons into account, Shull et al. (2012) end up with ~ 29% of baryons that is still not accounted for. This missing mass was claimed to be found in the WHIM by Nicastro et al. (2005, 2018), but, as will be discussed later, these observations are controversial. By studying the regions between galaxy pairs, de Graaff et al. (2019); Tanimura et al. (2019) found more evidence that these missing baryons indeed exist in galaxy filaments. The following section will go into more detail about methods to study the CGM/IGM to possibly detect those missing baryons.

1.3 Studying the CGM and IGM by observations

While stars have been studied for ages, observations of gas are more recent. Some of the first detections of gas around the Milky Way (MW) were Na I and Ca II lines in stellar spectra (Münch & Zirin 1961). Based on these observations, Spitzer proposed the existence of a galactic corona filled with hot gas in 1956 (Spitzer 1956) [1]. The origin of this corona was theorised to be primeval, or perhaps the result of gas ejected by stars. Spitzer also mentioned that, from time to time, gas from this corona could cool and collapse onto

[1] Münch showed the data to Spitzer before publication.

the spiral arms of the MW to form stars. Since then, different techniques to observe the CGM and IGM have been used.

The most obvious approach is to detect the gas of the CGM and IGM in emission, but as its emission is weak, it is difficult to detect. The WHIM, where many baryons reside, is not hot enough to emit in the X-ray regime and while denser parts of the IGM that are metal-enriched might be detected, background radiation will obscure emission coming from the low-density IGM (Furlanetto et al. 2004). There are several strategies that can be used to measure emission despite this, for example by looking at gas near a bright QSO (e.g. Cantalupo et al. 2014; Hennawi et al. 2015; Borisova et al. 2016; Mackenzie et al. 2020). The emission coming from the QSO can boost the Lyα emission of nearby gas up to a detectable brightness and in this way, the CGM of high-z galaxies has been detected (Wisotzki et al. 2018). This method is limited to the high-z Universe and optical, however.

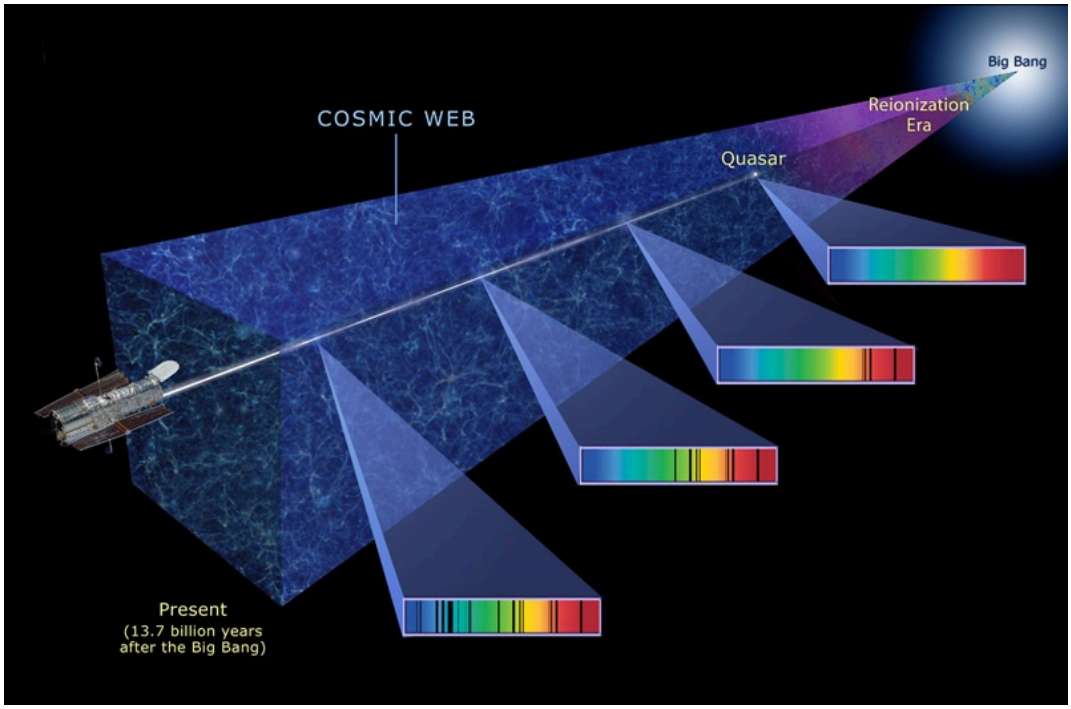

Figure 1.3 — Intervening matter causing absorption lines in the spectrum of a QSO (credit: NASA, ESA, and A. Feild (STScI))

Intergalactic gas is often studied in absorption, with the help of bright background objects like QSOs. These extremely bright objects were first discovered by Schmidt (1963). Based on the location of broad absorption lines in the spectrum of the object 3C 273, Schmidt (1963) concluded that the QSO was located far outside the MW, at a redshift of 0.158. Since then, many more QSOs have been discovered, with the most distant one to date being located at $z = 7.642$ (Wang et al. 2021).

Gas lying between the QSO and the observer will show as absorption in the spectrum measured by the observer (see Fig. 1.3). Doppler shift will cause the lines to be shifted with respect to their rest frame wavelength and from this, a cosmological distance can be inferred for a given cosmological model. As hydrogen is the most abundant element in the Universe, Lyα absorption will be easiest to detect, but stronger absorption systems

might also show metal absorption like Si III and O VI. These metals have been deposited there by feedback processes from galaxies.

For low z, Lyα absorption will be in the UV range of the spectrum at 1216 Å, meaning a satellite is needed to gather data. After ground-breaking studies on galaxy halos done with the *HST* in the '90's using Lyα absorption as well as various metal lines, the Cosmic Origins Spectrograph (COS) was installed on *HST* in 2009 with the aim of studying the role of gas in large-scale structure formation.

One of the most important initiatives to study the CGM of galaxies is the COS-Halos project. This project studied the halos of 44 galaxies at $z = 0.15-0.35$ by using background QSOs (Tumlinson et al. 2013). All sightlines passed within 150 physical kpc of the galaxy and Lyα was detected in all star-forming galaxies. For passive galaxies, the Lyα detection rate was 75%. This absorption traces gas with temperatures of about 10^5 K, indicating that some cooler gas remains even when the halo gas is expected to be shock-heated to temperatures $\sim 10^6$ K.

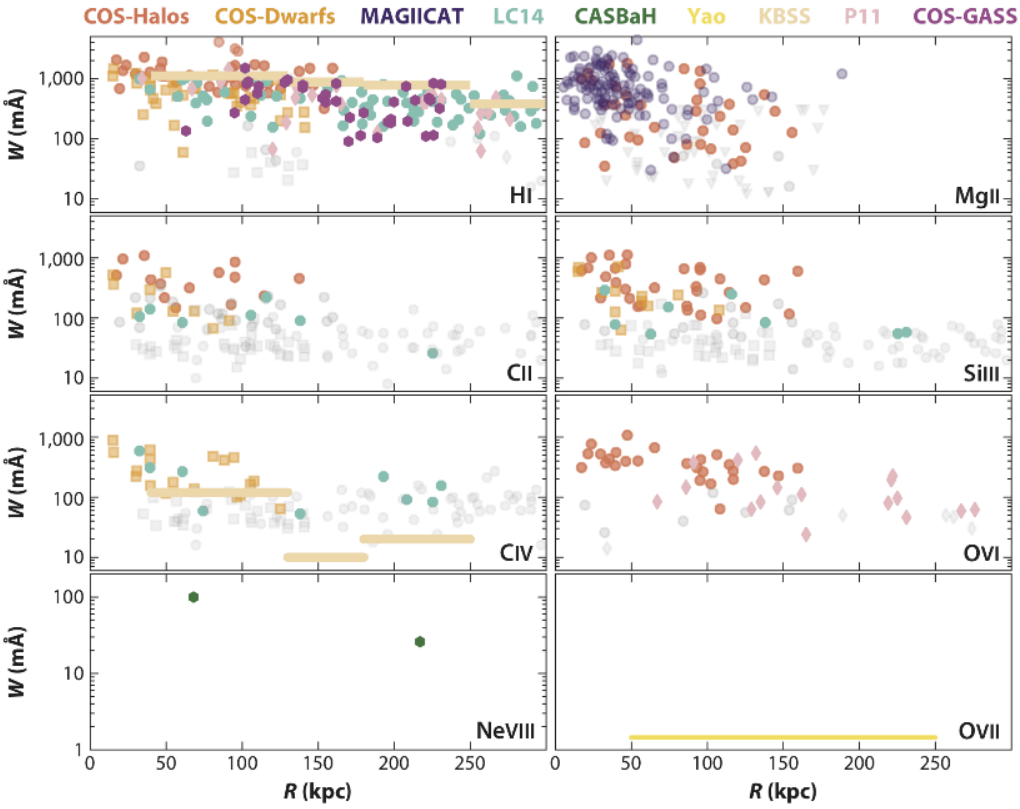

Figure 1.4 — Equivalent width measurements from various surveys (Fig. 4, Tumlinson et al. 2017).

Figure 1.4 shows equivalent width measurements for various ions. Since these ions trace gas at different temperatures, these measurements reflect the multi-phase structure of the CGM. This multi-phase structure is the result of the different processes described in Sect. 1.5, with cooler clouds traced by, for example, H I and C II, amidst the hot halo gas detected in higher ions like O VI.

For gas residing in the CGM of the MW, Lyα absorption of individual clouds falls within the Galactic absorption trough, making it impossible to use Lyα as a tracer.

However, because of the proximity of this gas, velocity shifted metal lines can be used to trace the CGM. To get distance estimates, it is possible to look at spectra from stars close to each other on the sky but at different, known distances in the Galactic halo. If the absorption is present in the spectrum of the more distant star, but not in the nearby star, this means the gas is located between the two. This is called the "bracketing" method (e.g. Wakker et al. 2007).

The disadvantage of this method is that it is limited by suitable background sources and it only gives information on the gas residing in that particular area. By combining data from a larger number of sightlines, a more complete picture can be made. This is what was done for the studies presented in this thesis.

Embedded in the hot Galactic halo exist high-velocity clouds (HVCs), whose velocities of $|v_{LSR}| \geq 80$ km s^{-1} distinguish them from the rest of the CGM. Individual HVCs have been shown to have a multi-phase structure (e.g. Giovanelli et al. 1973; Cram & Giovanelli 1976; Kalberla & Haud 2006). This structure was first discovered by Giovanelli et al. (1973), who found two populations of absorption components in their spectra: one with narrow lines (~ 10 km s^{-1}) and the other with broader lines (~ 25 km s^{-1}). This indicates a colder condensation cores within more extended, warm envelopes.

Absorption line spectroscopy is not the only tool at our disposal to study the CGM around the MW. Muller et al. (1963) were the first to detect 21-cm emission coming from the Galactic halo and noted the high velocity dispersion. Since then, large progress has been made in mapping HVCs, resulting in detailed maps showing the intricate network of H I gas around the MW (e.g. Westmeier 2018). H I emission shows that about 20% of HVCs have a head-tail structure, with a gradient in both column density and velocity (Brüns et al. 2000). The front part of HVCs (its "head") has the highest density and velocity, while the gas from the tail is stripped away by the surrounding medium.

The hot gas that surrounds the HVCs can be seen to interact with can be observed in X-ray emission. This gas has temperatures $T \gtrsim 10^6$ K and while early-type galaxies are more luminous in X-ray emission, late-type galaxies do also show extended emission (e.g. Anderson et al. 2013). Around early-type galaxies, the spectra show metallicities that are super-solar, indicating that it is enriched and it does not originate from the IGM (Mathews & Brighenti 2003, and references therein).

The above already showed that the CGM and the IGM do not stand on their own, but are connected to galaxies. The following section will focus on the large-scale structures outlined by dark matter and traced by galaxies.

1.4 Structure of the local Universe

To find whether the structures found in simulations are in agreement with those found in the Universe, galaxy surveys play a crucial role. One of the most important surveys was the National Geographic Society Palomar Observatory Sky Survey, which mapped the entire sky above a declination of 33°. Another survey which had a major impact is the Sloan Digital Sky Survey (SDSS, Colless et al. 2001; York et al. 2000). Its first data release was in 2000 and it is still ongoing. It includes both photometric and spectroscopic data and has been used to create the largest 3D sky map to date (Dawson 2020). These spectroscopic data can help with obtaining accurate redshifts, z, of galaxies, which in turn can be used to find their distance. The wavelength at which a spectral line is emitted

is λ_e and the wavelength at which is it observed is given by λ_o. Redshift is then defined as:

$$z = \frac{\lambda_o - \lambda_e}{\lambda_e}. \tag{1.1}$$

The redshift of an object can be used to derive its velocity (for a detailed discussion, see Davis et al. 2019). At large scales, cosmic expansion becomes important and an object's total velocity, v_{total}, consists of two components: the recession velocity, v_r, and peculiar velocity, v_p.

$$v_{total} = v_r + v_p \tag{1.2}$$

The recession velocity depends on the Hubble constant, H_0 and the proper distance of the object, D.

$$v_r = H_0 D \tag{1.3}$$

Subtracting the velocity due to cosmic expansion from the observed velocities results in the peculiar velocities, which are caused by gravitational interaction and thus can give insights in how structures are bound together.

1.4.1 Our local cosmological environment

Mapping peculiar velocities was the key to defining the Laniakea Supercluster of which the MW is a part (Tully et al. 2014). As can be seen in Fig. 1.5, the flow of peculiar velocities of the objects within this Supercluster converges to the centre of mass, which is called the "Great Attractor" (Dressler et al. 1987; Tully et al. 2014). It has been found that the Laniakea Supercluster is not gravitationally bound, meaning it will disperse in the future (Chon et al. 2015).

Within the Laniakea Supercluster, the Local Supercluster (also called the Virgo Supercluster) forms a smaller structure. This excess of galaxies in the northern hemisphere was argued to correspond to a real, overdense structure in the galaxy distribution by de Vaucouleurs (1953, 1956). The supercluster is constrained by, among other things, the Local Void. Roughly at the centre of this structure is the Virgo Cluster, which is the cluster closest to the MW at ~16.5 Mpc (Mei et al. 2007). Its proximity makes it one of the most studied clusters. It is a relatively young cluster, as studying the kinematics reveals that the core is still in the process of forming and not yet virialised (Binggeli et al. 1987, 1993).

1.4.2 The IGM and CGM in the local Universe

Since the focus of this thesis is on gas in the context of the large-scale structure of the local Universe, it is important to look at other studies with a similar focus. The gas in the nearby Virgo Cluster was studied by Yoon et al. (2012); Yoon & Putman (2013), who found few absorbers within the virial radius of the cluster, but an abundance of Lyα absorbers in the outskirts. This suggests that the intercluster medium (ICM) is too hot to be detected in Lyα absorption, which is in agreement with detections in X-ray of hot, diffuse gas from the centre of the cluster (Böhringer et al. 1994). Further proof for this hot ICM comes from galaxies with truncated H I discs near the cluster's centre (Chung et al. 2009). Ram pressure stripping causes these galaxies to loose their gas. While the

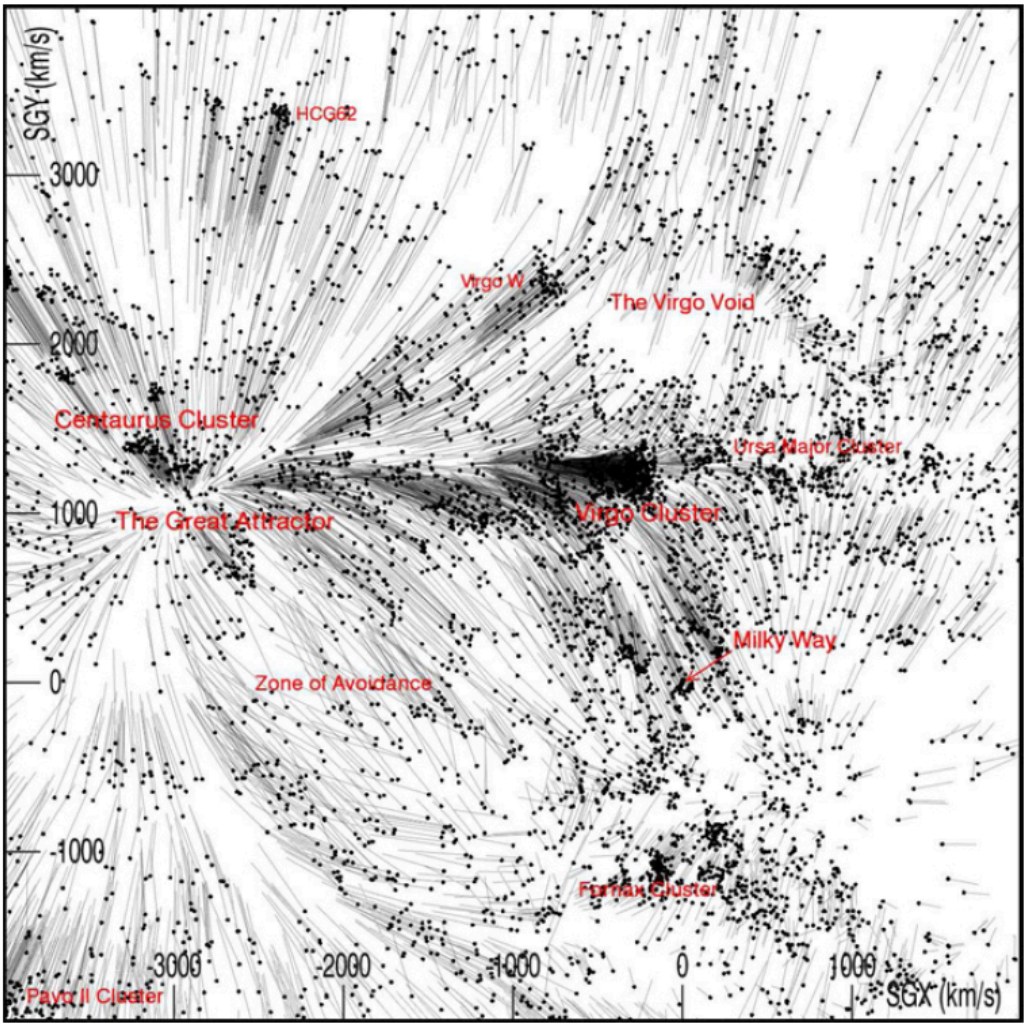

Figure 1.5 — Peculiar velocities for galaxies in the local Universe as found by Courtois et al. (2013, their Fig. 14). Galaxies are shown as dots, with their peculiar velocities given as vectors.

gas near the centre is likely too hot to show Lyα absorption, strong absorbers can be found in the filamentary substructures (Yoon et al. 2012). The same study also shows the covering fraction of absorbers is higher near the cluster than in the background. This is consistent with the idea of warm gas flowing via filaments into the dark matter potential well that is the centre of the cluster and getting shock heated as it draws nearer (Yoon et al. 2012). The detected gas might also be gas stripped from galaxies. While this seems likely for one particular sightline in Yoon & Putman (2017), which shows absorption within the virial radius of the Virgo Cluster and has a velocity within the cluster's velocity dispersion, most absorbers in Yoon et al. (2012) are found in regions without active stripping and thus seem to represent gas that might be used as fuel for star formation in nearby galaxies.

Another, more massive and regular cluster is the Coma Cluster. Because it is more massive, it is expected to have an even hotter ICM than Virgo. Similar to the Virgo Cluster, the Coma Cluster does not show Lyα absorption within the contours of X-ray emisssion (Yoon & Putman 2017). The velocity dispersion of the absorbers is higher than that of

the cluster itself, hinting at turbulent motions (Yoon & Putman 2017). Turbulent motions together with colder clumps are expected for the gas flowing along filaments (Emerick et al. 2015; Lau et al. 2009).

The Fornax Cluster, which is the cluster second-nearest to the MW is another well-studied environment. It has a mass of about $7 \cdot 10^{13}$ $M_\odot$ (Drinkwater et al. 2001), which is about 10% of the mass of the Virgo Cluster.

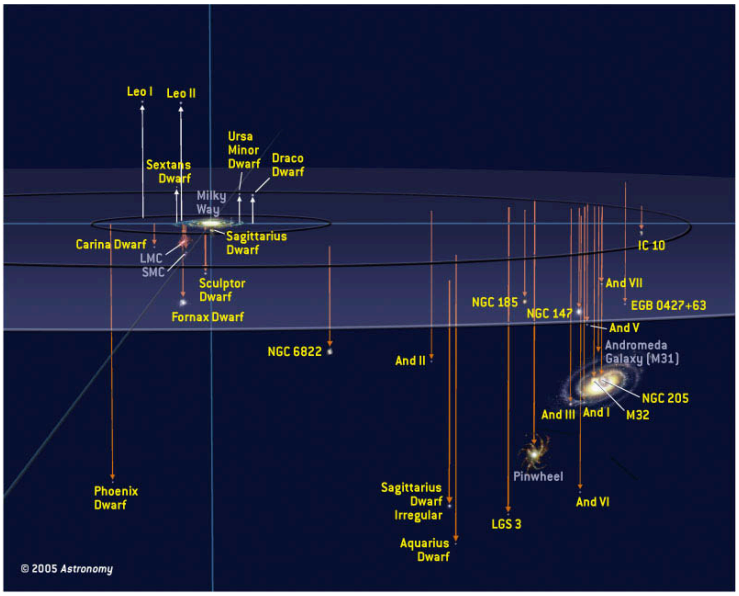

Figure 1.6 — Impression of the Local Group with its most prominent members (Kelly 2005).

On a smaller scale than galaxy clusters are galaxy groups. The MW and Andromeda (M31) are the most prominent members of the Local Group (LG), of which an impression is shown in Fig. 1.6. While this environment is the relatively nearby Universe, the different components of the IGM and the CGM are not easily disentangled, as it is difficult to obtain distance measurements, see also Sect. 1.3. The cosmological simulations of the LG done by Nuza et al. (2014) as part of the CLUES project show that the MW and M31 are embedded in a diffuse halo of hot gas ($T \geq 10^5$ K), with the cold gas ($T < 10^5$ K) showing a more filamentary structure (see Fig. 1.7). The third component that they studied, H I gas, is even more concentrated around the two galaxies, though some of it extends along the structures shown by the colder gas.

The HVCs that are part of the CGM of galaxies may form a bridge between the IGM and galaxies themselves. Some are infalling and can thus provide the MW with a reservoir of baryons for star formation. This continued accretion of matter from the surrounding medium fits the hierarchical structure formation model. Since the gas also traces the large-scale structure, this gas would be accreted from filaments. Blitz et al. (1999) argued that, for the LG, this would mean that mass would be sheared between the two most massive members, M31 and the MW. This gas would then fall into the galaxies as they are moving towards the LG barycentre. This fits with the model by Nuza et al. (2014) that suggested a bridge of gas between the MW and M31. While not all HVCs can be explained this way (see Wakker & van Woerden 1997), some might indeed be located outside of the virial radius of the MW and be part of the IGM between the MW and M31 (Sembach et al. 1999).

Further measurements of the velocities of HVCs around the MW show a velocity dipole indicating a stream of gas following the axis going through M31, the LG barycentre, the MW and onward, away from the MW (Richter et al. 2017). The HVCs towards the LG barycentre are shown to have negative velocities, suggesting they are at rest at

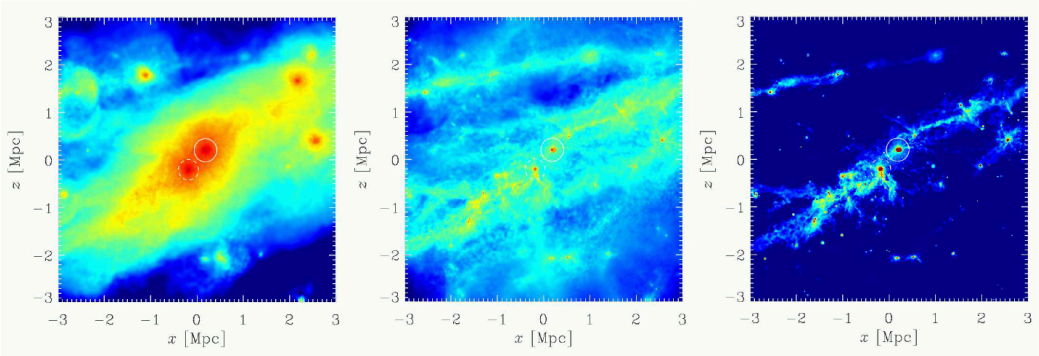

Figure 1.7 — Gas density for a simulation of the LG with the MW indicated by the dashed circle and M31 by the solid circle. Left panel shows hot gas (T $\geq 10^5$ K), middle panel shows cold gas (T $< 10^5$ K) and right panel shows H I (Fig. 1, Nuza et al. 2014).

the barycentre or inflowing from the direction of M31. The gas in the anti-barycentre direction on the other hand, is lagging behind: the MW is moving faster towards the barycentre than the more distant gas, thus resulting in positive velocities (in the local standard of rest frame) and an increasing distance.

While our perspective within the MW makes it hard to map the gas surrounding it, and other galaxies are too distant to have more than one QSO sightline passing through them, M31 provides an environment that is nearby enough to study the CGM. Using 18 sightlines, Lehner et al. (2015) probed the CGM of M31 at varying radii. For various ionised metals, they found absorption with velocities close to that of M31 and from this, they concluded that the CGM around M31 is multiphase and extends at least up to R_{vir}, becoming more ionised farther out.

More evidence for gas along a filament in the LG comes from Wolfe et al. (2013), who studied gas clouds between M31 and M33. These clouds were found to exist along a connecting axis and having velocities similar to those of M31 and M33. The latter means that they are unlikely to originate from tidal interactions between the two galaxies, as larger velocities would have been expected in that scenario. From the observed properties of these clouds, Wolfe et al. (2013) conclude the clouds are likely condensations of intergalactic gas that is part of a filament.

1.4.3 Intergalactic gas in filaments

Several studies have been initiated to detect gas in galaxy filaments on a larger scale than the LG (e.g. Morris et al. 1993; Penton et al. 2002; Prochaska et al. 2011; Wakker et al. 2015; Tejos et al. 2016). Filaments form the connection between clusters of galaxies and, in addition to galaxies, are thought to contain baryons in the form of diffuse plasma with temperatures of $T = 10^5 - 10^7$ K, which is hard to detect (Cen & Ostriker 1999; Davé et al. 2001). Wakker et al. (2015) defined a local filament and studied absorption on sightlines going through that filament. They found that strong absorbers are likely associated with galaxies, but this does not hold true for weaker absorbers ($\log N(\mathrm{H\,I}) \leq 10^{15}$ cm^{-2}), similar to findings from Tejos et al. (2012); Prochaska et al. (2011). Furthermore, equivalent widths (EWs) of the Lyα absorbers were found to correlate with filament impact parameter: stronger absorbers (not associated with a galaxy) were found closer to the filament axis. In addition to this, the absorbers closer to the filament axis

had a larger Doppler b-parameter (see Sect. 1.3) than those farther out, suggesting hotter gas near the central axis of the filament. All this shows that the gas traces the filaments defined by galaxies. To what extend this correlation holds, remains to be determined.

The above study only focused on overdense regions like clusters and filaments, but the underdense regions of the Universe are just as important in defining the large-scale structure. Lyα absorbers in voids have been found to follow a random distribution, with in general lower column densities than the absorbers at the edges of voids (Tejos et al. 2012). This shows that next to Lyα absorbers associated with galaxies, there is a population that is unrelated to galaxies. Tejos et al. (2012) argue that the 'random' population originates in structures still growing linearly from primordial density fluctuation.

1.5 Interplay between the CGM/IGM and galaxies

At present times, galaxies have formed and the collapse of matter onto galaxies has slowed down. This does not mean that the IGM and galaxies no longer influence each other. To the contrary, the interactions between the two fulfil an important role in the formation and evolution of galaxies. For example, gas residing in the IGM serves to replenish galaxies with new matter. This matter is needed to keep up the ongoing star formation observed in galaxies at the current day. The boundary layer that forms the connection between the IGM and galaxies is the CGM. Studying this layer can give insights into the interactions between the IGM and galaxies, thus leading to a better understanding of how both evolve with time.

Material accreting from the IGM (see Fig. 1.8a) is an obvious source of baryons. Models do indeed show gas from the IGM being accreted (White & Rees 1978; Kereš et al. 2005; Dekel & Birnboim 2006). This material from filaments is denser than the halo gas and thus shock heating will not have a large effect on the gas (Joung et al. 2012). The larger the overdensity of the cloud is, the longer it will survive without being shredded in the hot halo gas. The gas may form a co-rotating disc around the galaxy (Stewart et al. 2011) and thus will feed into the outskirts of the galactic disc rather than the galaxy's central region.

As mentioned in Sect. 1.1, the accretion paths for massive ($M > 10^{12}$ $M_\odot$) and less massive halos differ: hot-mode accretion is more important for the massive halos, whereas in lower mass galaxies, cold-mode accretion plays an important role (Birnboim & Dekel 2003; Kereš et al. 2005; Kereš & Hernquist 2009; Nelson et al. 2013). While both types of galaxies are surrounded by a halo that is heated to virial temperature, only in the more massive ones is incoming gas shock-heated. Infalling gas in lower mass halos does not create a stable shock, thus it does not heat until it reaches the plane of the galaxy (Birnboim & Dekel 2003). This means that IGM gas can be accreted directly, instead of having to cool first (White & Frenk 1991). In both scenarios, cool gas should be present in the CGM and indeed, observations have shown cold, dense matter with low metallicity to exist around galaxies (Fumagalli et al. 2011a; Lehner et al. 2013; Cooper et al. 2015; Glidden et al. 2016).

Direct evidence for galaxies accreting from the IGM is hard to find, although a recent study done with the Multi Unit Spectroscopic Explorer (MUSE) might have found a Lyman limit system (LLS) within a filament that is being accreted onto a galaxy (Lofthouse et al. 2020). Indirect evidence comes, for example, from the observation that the fraction of galaxies associated with a Lyα absorber continuously decreases as impact parameter increases (Wakker & Savage 2009). Contrary to the scenario where the gaseous

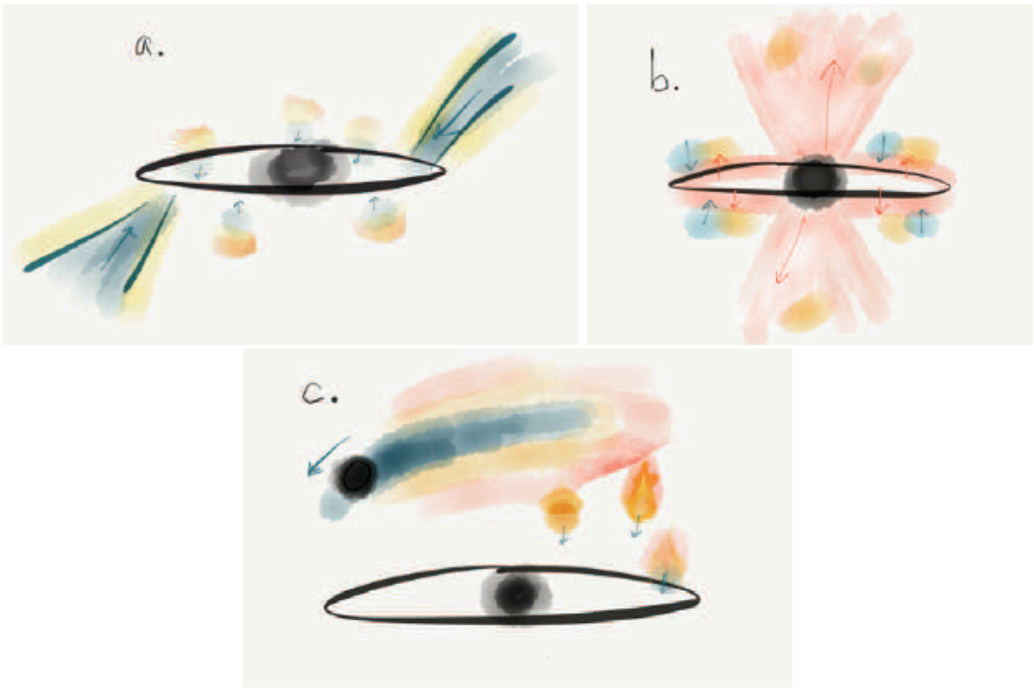

Figure 1.8 — Several modes of accretion, with hot gas shown in red and cooler gas in blue. a) Gas accreting onto the galaxy from the IGM. b) Stellar feedback causes gas to be ejected from the galaxy, into the halo, where it cools before falling back down. c) Gas gets stripped from satellite galaxies (Fig. 2, Putman 2017).

halos of galaxies are clearly separated from the large-scale structure – in which case there would be a break in the detection fraction – the steady decline shows the connection between the CGM and IGM. Similarly, Penton et al. (2002) found no correlation between Lyα equivalent width and galaxy impact parameter for low-density absorbers (N(H I) $< 10^{15}$ cm^{-2}). These weak absorbers are thus not the result of gas expelled from galaxies, but are part of the IGM. Another hint of IGM gas being accreted onto galaxies comes from observations of LLSs at $z \sim 0$ which suggest a dichotomy between absorbers with low and high metallicity ($\sim$ 2.5% and $\sim$ 50% solar metallicity) (Lehner et al. 2013). The low-metallicity absorbers likely represent IGM gas that is less metal-enriched.

Not all the gas clouds found in the CGM originate in the IGM, however. Feedback processes in galaxies contribute hot gas to the CGM that is more metal-enriched than the IGM gas (Fig. 1.8b). The origin of this gas ranges from supernova explosions to feedback from active galactic nuclei (AGN). In low-mass systems, (part of) the gas that is ejected into the CGM can escape the galaxy and enrich the IGM, but in high-mass systems, this gas is retained and remains hot (e.g. Binney 2004; Bower et al. 2006). This hot gas cannot directly collapse onto the galaxy to trigger new star formation.

One of the ways to cool hot coronal gas is through so-called "galactic fountains" (Shapiro & Field 1976). In this scenario, relatively cold gas (T < 10^3 K) near the galactic plane is swept up by stellar winds or supernovae. As clouds of this cold gas travel through the hot coronal gas, they interact with the hot gas, causing it to cool. This cooled down gas can then be accreted by the galaxy and form stars (Fraternali & Binney 2008, see Fig. 1.9).

The gas ejected from the galaxy in this way has higher metallicity than the coronal gas, therefore this is one way the outlying gas can be enriched (Richter 2017).

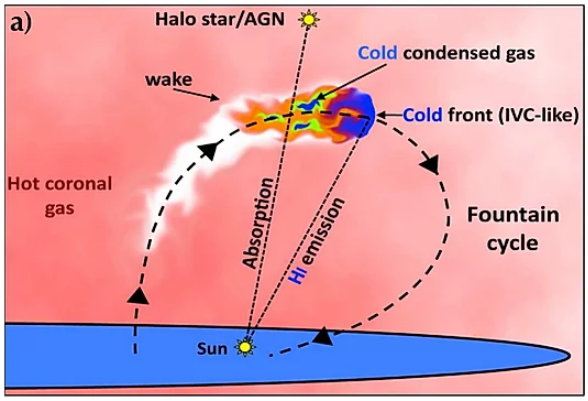

Figure 1.9 — Galactic fountain model (Fig. 11, Fraternali 2017)

Another origin for accreted gas are satellite galaxies (Fig. 1.8c). For the LG, it has been shown by Grcevich & Putman (2009) that the dwarf galaxies at smaller galactocentric radii have less H I than those at larger distances. The gas from these galaxies can be removed by various processes such as ram-pressure stripping and tidal interactions. Depending on the mass of the satellite galaxies, they can provide substantial amounts of fuel to their host galaxy.

Sancisi et al. (2008) showed that gas stripped from dwarf companions could account for at least $0.1-0.2$ $M_{\odot}yr^{-1}$ of accreted gas. The actual number might be higher, as ionised hydrogen and helium will also contribute. However, to keep star formation at the observed rate of $\sim 1 M_{\odot}yr^{-1}$, they argue that accretion directly from the IGM is needed. Using H I observations from galaxies in the local Universe, Di Teodoro & Fraternali (2014) came to a similar result for the amount of gas supplied by these minor mergers, namely a maximum of $0.28 M_{\odot}yr^{-1}$. The same study showed that about 22% of galaxies studied have detected dwarf companions and they could not find evidence for a significant population of H I clouds, leading to the conclusion that additional mass must be accreted from other sources.

To get a better view of how much each type of accretion contributes, characteristics of the gas surrounding galaxies should be studied. Satellite companions and gas previously ejected from the galaxy will have higher metallicities, whereas gas from the IGM is not as enriched. Low-metallicity LLS might be one of the most important tracers of accreting IGM gas (Lehner et al. 2013; Cooper et al. 2015).

1.6 Aims and outline of the thesis

The different phases of the IGM and CGM require a combination of methodological approaches in studying them. **The main aim of this thesis is to reach a better understanding of the connection between the IGM and the large-scale structure as traced by galaxies in the local Universe.** As mentioned before, the COS instrument and galaxy catalogues have greatly advanced the study of the local Cosmic Web. However, many questions remain unanswered and to obtain a more complete view of the interplay between galaxies, the CGM and the IGM, we look at different scales in the local cosmological neighbourhood.

Questions that will be addressed in this thesis are:

How does the wider gas environment connect to the cosmological structure in which galaxies reside?

- What is the origin of HVCs around the MW? Some are part of the MW's CGM, but a subset might also reside at larger distances and could be connected to the IGM of the LG.
- Do Lyα absorbers trace individual galaxies or the large-scale structure they reside in? A sample of *HST*/COS sightlines scattered over the entire sky is used to address to this question.
- Is there a population of Lyα absorbers following a random distribution, as found in previous studies?

Archival data from the COS instrument mounted on the *HST*, together with galaxy data from the publicly available V8k catalogue, are used to provide a tomographic view of the CGM/IGM around galaxies and find answers to these questions. Absorption lines of different species (e.g. Lyα, Si III and C II) are measured in the spectra of background QSOs. For a sub-set of these lines, models are used to obtain column densities as well as physical parameters.

Outline

The different analysis methods and underlying physics of them will be discussed in Chapter 2, together with more details about the COS instrument. HVCs and their relation to the gaseous bridge between the MW and M31 is the topic of Chapter 3. Going from the LG to nearby large-scale filamentary structures, Chapter 4 discusses the relation between Lyα absorbers and galaxy filaments. Finally, the results are discussed and summarised in Chapter 5.

2 Methods and Instrument

What is the origin of HVCs around the Milky Way? How are Lyα absorbers connected to the large-scale structure? The methods used to answer answer these and other questions about the relation between CGM, IGM and large-scale structure, will be discussed in this chapter. Sections 2.1.1 and 2.1.2 will go into more details about the physics of absorption spectra, while Sections 2.1.3 through 2.1.5 will discuss how absorption spectra can be analysed. Absorption line measurements have been used to model the physical conditions of the gas, as described in Section 2.2. Finally, two statistical methods that were used in this study are discussed in Section 2.3.

2.1 Spectroscopy

With hydrogen being the most abundant element in the Universe, it is most easily detected and it is one of the main elements used in this thesis to probe the gas residing around and in-between galaxies. Emission might seem the most straightforward method to study the IGM, as it originates directly from the gas, but due to its low-density and often low temperatures, this emission is too weak to be detected with current instruments. Spectra of bright background objects, however, allow us to detect and identify the IGM in absorption. Here, the signal-to-noise of the background objects limits the sensitivity for detection of even weak absorbers. Since Lyα absorption in QSO spectra is an important aspect of this thesis, the physics involved in this absorption will be discussed first in this section.

2.1.1 Absorption spectra

Lyα absorption occurs when a photon hits a hydrogen atom and causes the electron to go from the ground state, $n = 1$, to the first excited state, $n = 2$. The energy levels of the hydrogen atom can be derived with the following equation:

$$E_n = -13.6 \text{ eV}/n^2. \tag{2.1}$$

From this, it follows that the energy needed to excite an electron from $n = 1$ to $n = 2$ is 10.2 eV. This corresponds to a photon with a wavelength of 1215.67 Å. Neutral hydrogen, H I, will be easily ionised by UV photons below this wavelength.

The ionisation of species other than hydrogen is more complicated, as they have multiple electrons and can thus be ionised multiple times. For example, Si II is singly ionised silicon, missing one electron; Si III is doubly ionised and missing two electrons, etc. Because of the more complex structure of those species, the ionisation energies are not as easily calculated as that of hydrogen and instead have to be measured from experiments.

Since the photon ionising a species is absorbed, the intensity of light at that specific wavelength will be reduced. The optical depth (τ_ν) describes how much of the incident light is absorbed by the intervening medium at a given frequency. Assuming an intensity $I_{0,\nu}$ for the light coming from the source, the light reaching the absorber will have intensity I_ν:

$$I_\nu = I_{0,\nu} e^{-\tau_\nu}. \tag{2.2}$$

If $\tau_\nu >> 1$, the gas cloud is optically thick, while for $\tau_\nu << 1$, it is optically thin, or transparent. Different column densities of the regions containing H I result in different absorption spectra and Lyα absorption can be divided into three different categories: the Lyα forest, LLSs and damped Lyα systems (DLAs).

The regions with the highest column density are DLAs, which are defined to have $N(\mathrm{H\,I}) \geq 2{\cdot}10^{20}$ cm^{-2} (Wolfe et al. 1986) and are optically thick in H I absorption. These systems are thought to be the precursors of modern day galaxies when their H I will be converted for a larger part into stars.

LLSs have column densities of $1.6{\cdot}10^{17} < N(\mathrm{H\,I}) < 2{\cdot}10^{20}$ cm^{-2}. These regions absorb most of the radiation with rest-frame wavelengths shorter than 912 Å (Péroux et al. 2003). This wavelength corresponds to a photon with enough energy to ionise hydrogen. Like the DLAs, these systems are also optically thick.

With its low densities, the Lyα forest is most prevalent in the Universe. This series of absorption lines arises when light is scattered by neutral hydrogen with densities $N(\mathrm{H\,I}) \leq 10^{17}$ cm^{-2}. These low densities result in lines that are predominantly optically thin. As the light travels from the source to the observer, it passes many such diffuse gas clouds at different distances, resulting in a host of absorption lines, hence the name Lyα forest.

Ionisation can occur because of photons (photoionisation), but also through collisional ionisation of atoms with other particles. By studying these different ionisation states, it is possible to get a better understanding of the physical conditions of the gas.

2.1.2 Line broadening

An absorption line will always have a certain intrinsic width, which depends on the absorbing medium. Various physical processes cause line broadening and one of the possible line profiles is a Doppler profile. In such a profile, the absorption lines are Doppler broadened due to the motions of atoms and ions.

The speeds of these particles in an ideal gas follow a Maxwell-Boltzmann distribution with the most probably speed given by $v_{mp} = \sqrt{2kT/m}$, where the mass of each particle is m, temperature, T, and the Boltzmann constant, k. This gives a root mean square speed, v_{rms}, of:

$$v_{\mathrm{rms}} = \left(\frac{3kT}{m}\right)^{1/2}. \tag{2.3}$$

This can be combined with the equation for the Doppler shift of a line:

$$\Delta\lambda/\lambda_0 = v_r/c. \tag{2.4}$$

Here, $\Delta\lambda$ gives the wavelength interval over which the line is spread out, λ_0 the central wavelength, and c the speed of light. The radial velocity, v_r, only takes into account velocities along the line of sight. The Doppler width of a spectral line is thus given by,

$$\Delta\lambda \approx \frac{2\lambda}{c}\sqrt{\frac{2kT}{m}}. \tag{2.5}$$

The broadening of the absorption line is described by the Doppler parameter, b, which consists of a turbulent and a thermal component:

$$b_{\text{tur}} = \sqrt{2}\sigma_v, \tag{2.6}$$

$$b_{\text{th}} = \sqrt{\frac{2kT}{m}}. \tag{2.7}$$

In these equations, σ_v is the one dimensional velocity dispersion , k the Boltzmann constant, T temperature and m the mass of the absorbing particle (Draine 2011; Fontana & Ballester 1995). Unresolved substructure is another factor that could add to the line broadening, but is not taken into account in these equations.

Doppler broadening is not the only process to influence linewidths. Collision broadening causes dampening wings in the line profile and the width of these wings depends, among other things, on the average time between collisions, Δt_0. If the number density is n and the collision cross-section of the particles σ, the average time between collisions (Δt_0) can be found:

$$\Delta t_0 = \frac{1}{n\sigma\sqrt{2kT/m}}. \tag{2.8}$$

From this, the width due to collision broadening can be approximated by (see e.g. Carroll & Ostlie 2007):

$$\Delta\lambda = \frac{\lambda^2}{c}\frac{1}{\pi\Delta t_0} \approx \frac{\lambda^2}{c}\frac{n\sigma}{\pi}\sqrt{\frac{2kT}{m}}. \tag{2.9}$$

Another contributor to line broadening is the uncertainty principle. This type of broadening is also called "natural broadening" and is a result of the finite lifetime of a state. The uncertainty in energy (ΔE) and the lifetime of the excited state (Δt) follow the relation:

$$\Delta E\Delta t \gtrsim \hbar. \tag{2.10}$$

An increased number density leads to more collisions, decreasing the lifetime of a state, thus resulting a larger uncertainty in the energy. These two processes both give rise to a Lorentzian line profile, which is described by:

$$L(\Delta\nu) = \frac{\Gamma}{(2\pi\Delta\nu)^2 + (\Gamma/2)^2}. \tag{2.11}$$

The full width at half maximum is defined by 2Γ. For natural broadening, Γ is inversely proportional to the natural life time, $\gamma = 1/(2\pi\Delta t)$, whereas for collision broadening, $\Gamma = \gamma + 2\nu_{\mathrm{col}}$. The frequency of collisions is ν_{col}.

The relevance of these different broadening mechanisms depends on the conditions of the gas, with Doppler broadening being more important at high temperatures and low pressures, whereas collisional broadening plays a significant role at high pressure. A high column density will also result in the damping wings seen in a Lorentzian profile. A Voigt-profile takes both line profiles into account and can thus be used for gas in a variety of environments. It is a convolution of a Lorentz profile (collision broadening) and a Gaussian profile (Doppler broadening) and is often used in modelling absorption lines.

2.1.3 Analysing spectra

QSOs or other bright background objects can be used to obtain absorption spectra, like mentioned in Sect. 1.3. In order to obtain information on chemical abundances and the physical conditions of the intervening gas, absorption lines have to be analysed. This analysis can be done by either measuring equivalent widths (EWs) or by using models. Both will be discussed here.

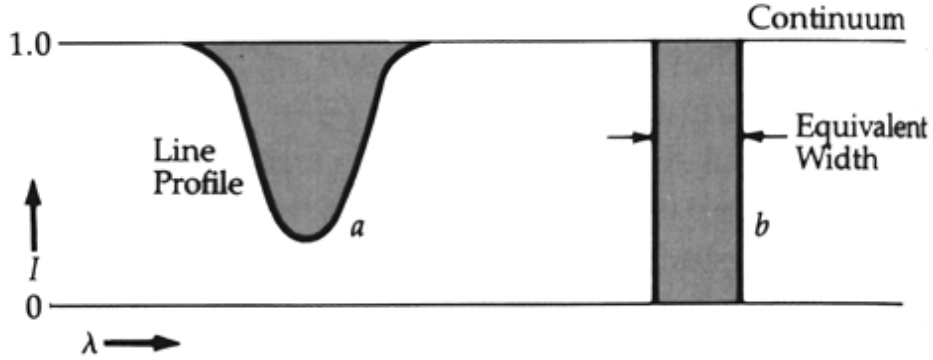

Figure 2.1 — Absorption line together with its equivalent width[2].

EW measurements are the most straightforward way to measure absorption as they measure the relative amount of light lost. Fig. 2.1 shows an example absorption line on the left with the corresponding EW on the right. Assuming the absorption line covers an area A and the intensity of the continuum is I_C, the EW is defined as the width (b) of a rectangle reaching up to the continuum that covers the same area as the absorption line, so that $A = I_C \times b$. Equation 2.12 shows the integral used to calculate the EW (W_λ).

$$W_\lambda = \int_{\lambda_1}^{\lambda_2} \frac{I_C - I_\lambda}{I_C} d\lambda \tag{2.12}$$

Since the CCD of a telescope is limited by its pixel size ($\Delta\lambda$) and therefore divides the spectrum in discrete wavelength steps, the EW is (see e.g. Stetson & Pancino 2008):

$$W_\lambda = \Delta\lambda \sum_i \frac{I_{C_i} - I_i}{I_{C_i}}. \tag{2.13}$$

[2] http://ircamera.as.arizona.edu/astr_250/Lectures/Lecture_15.htm, accessed: 06-05-2020

The continuum level flux at the ith pixel is I_{C_i} and I_i is the flux received at that pixel. An advantage of using EWs is that this method is independent of the resolution of the instrument and of the instrumental profile. Furthermore, there are no underlying assumptions made on the physics involved. All this means that EWs from different works, measured with different instruments can easily be compared. However, EW does depend on redshift, but this effect is negligible for the results of this study, as it studies only the very nearby Universe.

The EW of a line is only an indication of the area an absorption line takes up, it does not distinguish between narrow, deep lines and broad, shallow lines. It also does not take into account that lines can be blended and physical properties, like the temperature of the gas, cannot be derived from EW measurements.

To get more information on physical conditions of the gas or for disentangling blended lines, model spectra can be used. These synthetic spectra are produced by modelling the physical processes taking place when light passes through a medium.

2.1.4 Curve of growth

The curve of growth describes how the equivalent width of a line increases with increasing column density. Since, as described above, various processes play a role in this broadening, the curve of growth is not a linear relation. First of all, the oscillator strength of a line plays a role. This quantity describes the probability that a photon will be absorbed or emitted for a given transition of a species, so that a transition with a higher oscillator strength will produce a stronger line than one with a low oscillator strength. For weak lines, the curve of growth increases linearly with column density. In this regime, the broadening because of collisions is not significant compared to the Doppler broadening, so that:

$$W \propto N. \tag{2.14}$$

As the density increases and the line saturates, the Doppler wings do not grow very strongly, leading to a slower increase of EW with column density (N),

$$W \propto \sqrt{\ln N}. \tag{2.15}$$

As shown in Fig. 2.2, at this point, no background light can be detected anymore and the absorption line becomes saturated. The curve of growth flattens, until collision broadening becomes important at an optical depth, $\tau_\nu \gg 1$ and the relation becomes:

$$W \propto \sqrt{N}. \tag{2.16}$$

By using both the EW and the curve of growth, the column density of the measured chemical species can be calculated. Together with assumptions on diameter and the gas cloud's symmetry, a volume density and total mass can be derived from the column density.

In conclusion, there are several factors that come into play when deciding whether to measure EWs or to model absorption lines. In this work, both approaches will be used. For the relatively small sample of sightlines in Chapter 3, all absorption components were modelled, while the larger sample in Chapter 4 has EW measurements for all Lyα components and only a subsample was selected to be modelled.

2.1.5 Synthetic spectra

The spectra used in this study are analysed with the span code written by Richter et al. (2011), which is based on the FITLYMAN date-reduction package that is part of the ESO-MIDAS analysis software (Fontana & Ballester 1995). Both codes model absorption lines by using a Voigt profile. For a line with central wavelength λ_c, column density N in a spectrum I_0, this kind of profile is described by:

$$I_\lambda = I_{0,\lambda} e^{-r_\lambda}, \qquad (2.17)$$

where r_λ is the optical depth, $r_\lambda = \frac{N r_0 f \sqrt{\pi} c \lambda_c 10^{-8}}{b\sqrt{2ln2}} H(a,u)$. The Voigt function is:

$$H(a,u) = \int_{-\infty}^{\infty} \frac{e^{-y^2} dy}{a^2 + (u-y)^2}, \qquad (2.18)$$

where a and u are parameters given by,

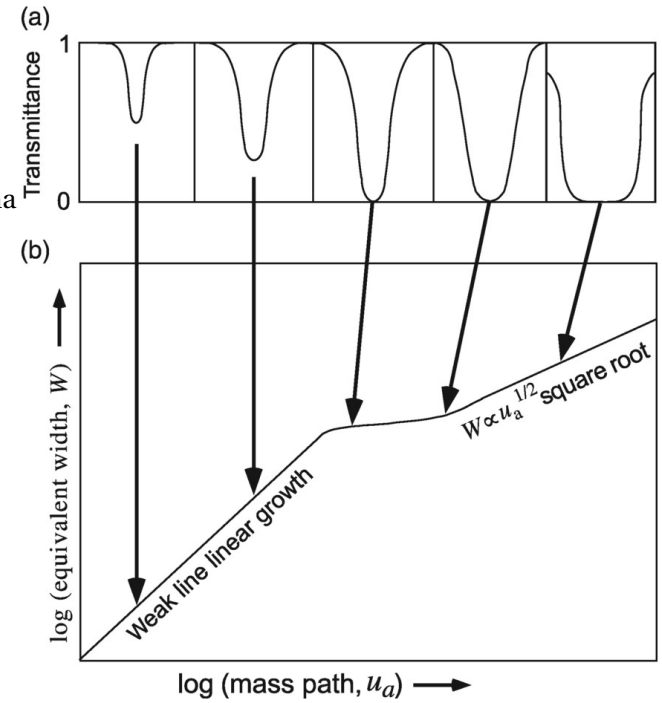

Figure 2.2 — Absorption lines with increasing equivalent width (panel a) together with their curve of growth (panel b). The curve of growth increases as a function column density (u_a in this plot) (figure from Catling & Kasting 2017)

.

$$a = \frac{\Gamma \lambda_c}{4\pi b 10^{13}}; \quad u = \frac{(\lambda_c - \lambda)c}{b\lambda_c \sqrt{2\ln 2}}. \qquad (2.19)$$

The parameters Γ and f are the damping coefficient and the oscillator strength, respectively. Furthermore, r_0 is the classical electron radius, c the speed of light and b the Doppler parameter. The Doppler parameter is calculated with (see also Equations 2.6 and 2.7):

$$b = \sqrt{b_{\rm tur}^2 + b_{\rm th}^2}. \qquad (2.20)$$

In the FITLYMAN program, the Voigt profile of each absorption line is thus defined by four parameters: $\lambda_c, N, b_{\rm tur}$ and $b_{\rm th}$. In addition to this, the oscillator strength, damping coefficient and rest frame central wavelength for each transition are used in the modelling.

To obtain an accurate model spectrum, the line-spread function (LSF) of the instrument should also be taken into account. The LSF causes additional line broadening in the detected spectrum and the model spectrum has to be convolved with the LSF of the instrument. In the case of COS, the LSF is non-Gaussian and has broad wings, which limit the detection of faint, narrow features (Dashtamirova et al. 2020).

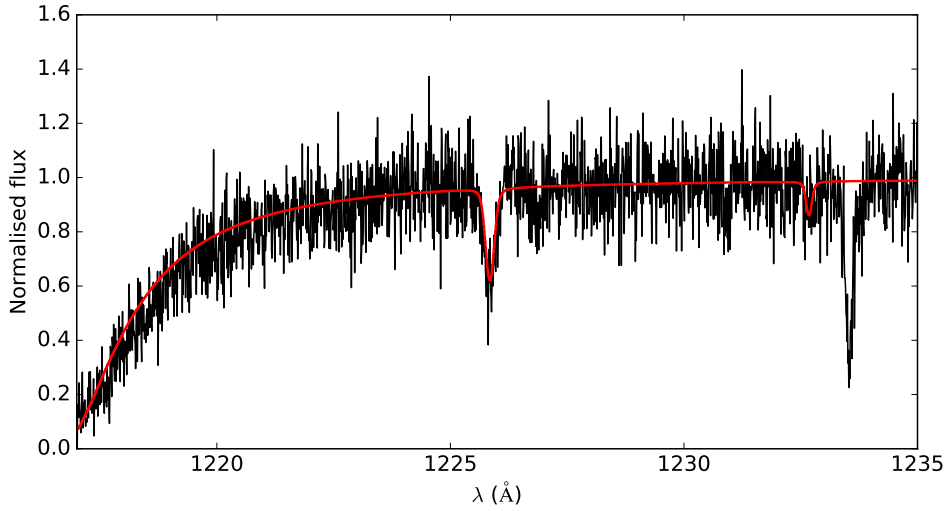

Figure 2.3 — Example spectrum of QSO TON580 (black) together with the synthetic spectrum used to measure Lyα absorption at 1225.9 and 1232.7 Å (red). Galactic Lyα absorption can be seen on the left side of the spectrum.

While the original `FITLYMAN` package fits a model to the absorption based on minimisation of χ^2, the custom-written `span` code produces synthetic spectra based on individual components like in Richter et al. (2013). This method allows a single absorber to have multiple lines with different physical conditions, as well as blended lines in general. The first condition is necessary to model the multi-phase structure of HVCs. The column densities of different species can be varied, as well as the Doppler parameter, to obtain a synthetic spectrum that matches the one observed. Figure 2.3 gives an example of a QSO spectrum and the matching synthetic spectrum.

2.2 Ionisation modelling

Once absorption lines have been measured, these data can be used to derive volume density and a more accurate temperature of the absorption system. We use the Cloudy code version 17.00 (Ferland et al. 2017) for this[1]. The physical background is described in Osterbrock & Ferland (2006).

With an incident radiation field that has a mean intensity of radiation, J_ν (energy units per unit area, per unit time, per unit solid angle, per unit frequency interval), the photoionisation rate of hydrogen per unit area (Γ) is described by:

$$\Gamma = n(\mathrm{H\,I}) \int_{\nu_0}^{\infty} \frac{4\pi J_\nu}{h\nu} a_\nu(\mathrm{H}^0) d\nu. \tag{2.21}$$

Here, $n(\mathrm{H\,I})$ is the number density per unit volume of neutral hydrogen, and $h\nu$ is the energy each incident photon has. Only photons with energy $h\nu > h\nu_0$ are capable of ionising hydrogen. The number of photons reaching the slab of gas per unit area, per unit time, per unit frequency interval is $\phi_\nu = \frac{4\pi J_\nu}{h\nu}$.

[1] `https://www.nublado.org/`

Part of the ions created by photoionisation will recombine, with a rate that depends on the electron and proton densities (n_e and n_p), as well as recombination coefficient $\alpha_A(\mathrm{H\,I}, T)$. The recombination rate is thus:

$$R = n_e n_p \alpha_A(\mathrm{H\,I}, T)\ [\mathrm{cm^{-3}s^{-1}}]. \tag{2.22}$$

Osterbrock & Ferland (2006) derive in their Chapter 2 that the typical recombination time is of the order of $10^5/n_e$ yr, which is usually long enough to establish an ionisation equilibrium in which the photoionisation rate (Equation 2.21) equals the recombination rate (Equation 2.22). If the system is also in thermal equilibrium, the energy gained by absorption of ionising photons equals the energy lost by radiation. An ionising photon with energy $h\nu$ produces a photoelectron with energy $\frac{1}{2}mv^2 = h(\nu - \nu_0)$, where m is the mass and v the velocity of the emitted electron. If this electron recombines, its energy $\frac{1}{2}mv^2$ is "lost". The main recombination process is collisional excitation of ions, which is followed by emission of a photon when the ion reverts back to its ground state. The photon may escape from the gas cloud.

The energy per unit volume per unit time gained because of photoionisation is:

$$G(\mathrm{H}) = n(\mathrm{H^0}) \int_{\nu_0}^{\infty} \frac{4\pi J_\nu}{h\nu} h(\nu - \nu_0) a_\nu(\mathrm{H^0}) d\nu\ [\mathrm{erg\,cm^{-3}s^{-1}}]. \tag{2.23}$$

Combining this with Equations 2.21 and 2.22 to eliminate $n(\mathrm{H^0})$ gives:

$$G(\mathrm{H}) = n_e n_p \alpha_A(\mathrm{H^0}, T) \frac{3}{2} k T_i. \tag{2.24}$$

In this equation, $\frac{3}{2}kT_i$ is for the initial temperature of the created photoelectrons. The energy gained thus depends on the recombination rate, because of the cloud being in ionisation equilibrium. The energy lost by recombination is:

$$L_R(\mathrm{H}) = n_e n_p kT \beta_A(\mathrm{H^0}, T)\ [\mathrm{erg\,cm^{-3}s^{-1}}], \tag{2.25}$$

where $\beta_A(\mathrm{H^0}, T)$ is the effective recombination coefficient for hydrogen at temperature T. The recombination cross sections have an anti-correlation with the energy of the electrons, so it roughly scales with v^{-2}. More energetic electrons are less likely to be captured than the ones with lower kinetic energy, causing the cloud to heat up. If a gas cloud is in thermal equilibrium, $G(\mathrm{H}) = L_R(\mathrm{H})$.

Other processes, like free-free emission or radiative cooling, which follow the collisional excitation of species such as O and N, play a role in cooling. The latter process is important in an astrophysical context, despite the low number density of elements other than H and He, because their excitation potentials are of the order kT, while those for H and He are much higher.

For thermal equilibrium to hold, the heating rate, G, should equal the cooling rates due to recombination (L_R), free-free emission (L_{FF}) and collisional excitation (L_C). Typical heating and cooling rates for a photoionised gas with low-density are shown in Fig. 2.4. These rates are calculated for various the kinetic temperatures and at the point where the two lines intersect, the gas is in thermal equilibrium. The peak of the cooling function near $T = 10^3$ K is where fine-structure lines are important coolants. Cooling decreases when increasing temperature after this point, until optical forbidden lines become important at $T \sim 4000$ K.

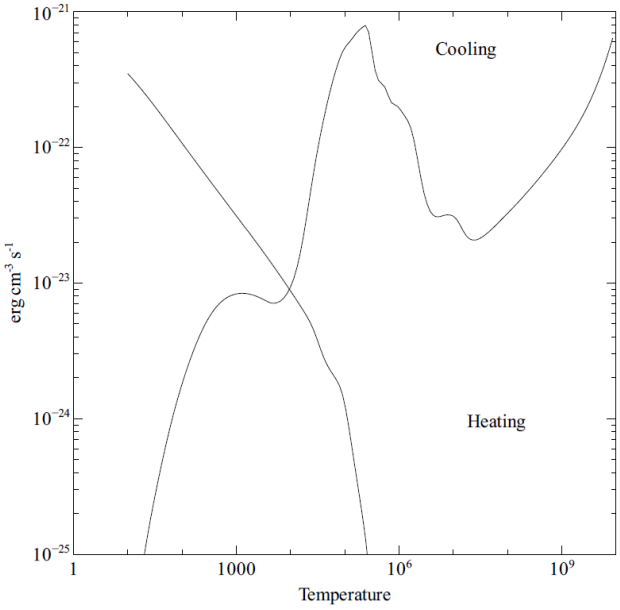

Figure 2.4 — Heating and cooling function for a low-density photionised gas (Fig. 10.1 from the Hazy 2 documentation for Cloudy version 13.05, Ferland et al. 2013).

By simulating an astrophysical environment, the Cloudy code determines the ionisation, gas temperature and chemical state of the gas. From these parameters, it predicts the resulting spectrum. It takes an optically thick slab of gas that can be illuminated by an external radiation field, assuming non-equilibrium, steady-state conditions. This slab is divided into concentric zones (shells), which are small enough to assume the physical conditions remain constant. In this work, we use the ionising background described in Haardt & Madau (2012) in addition to the CMB. This ionising background is caused by, for example, quasars and star-forming galaxies. The Haardt & Madau (2012) background includes, among other things, X-ray emission of quasars and UV-emission from star-forming galaxies, and is an updated and extended version of the ionising background from Haardt & Madau (1996). Energetic photons from these sources will ionise the gas as outlined in the equations given in this section and the various physical processes in the gas are calculated to obtain resulting chemical abundances of different ions, as seen in Fig. 2.5. These abundances may then be compared to those that are measured in spectra to find, for example, n_H of the gas.

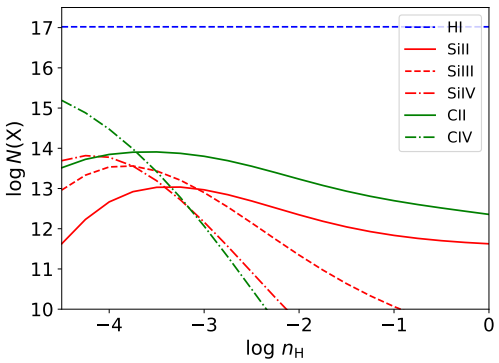

Figure 2.5 — Example of Cloudy output for the abundances of several ionised species for log$N$(H I) = 17.0 and different logn_H. A metallicity of $Z_X = 0.1$ is assumed.

2.3 Statistical methods

Several statistical methods have been used in this thesis, first of all the Lee statistic. This statistic can be found in Chapter 3, where it was applied to a sample of HVCs in order to find whether there were two separate populations of absorbers. In Chapter 4, the Kolmogorov-Smirnov (KS) test was used to compare the distribution of galaxies, Lyα absorbers and random points around filaments with each other.

2.3.1 Lee statistic

The Lee statistic can be used to find bimodality in data, as well as the most likely partition point (Lee 1979). This test thus shows whether there are two distinct populations or whether all data are drawn from the same parent population. Fitchett & Merritt (1988) applied the one-dimensional version in an astronomical context of dynamics in the Hydra I Cluster. Their Equation 4 gives the one-dimensional form of the Lee statistic for a sample of size N as:

$$L = \max_{\text{partitions}} \left\{ \frac{N m_2^{(\text{tot})}}{N_l m_2^{(l)} + N_r m_2^{(r)}} - 1 \right\}. \tag{2.26}$$

The second moment, m_2, is calculated by, $m_2 = N^{-1}\Sigma(v_i - \bar{v})^k$. In Fitchett & Merritt (1988), a sample of velocities, v_i, was analysed, but this can be replaced by any desired parameter. N_l and N_r are the number of data points to the left and right of the partition value, respectively, and $m_2^{(l)}$ and $m_2^{(r)}$ the second moments of these subsets. The second moment of the entire subset is $m_2^{(tot)}$. The most likely partition value will give the highest outcome of the part between brackets in Equation 2.26. If the data belong to two distributions that are separated by more than their respective variances, L will become large. The general form and derivation of the Lee statistic is outlined in Lee (1979).

2.3.2 Kolmogorov-Smirnov test

Another statistical test that can be used to compare two data samples is the Kolmogorov-Smirnov test. The null hypothesis is that both samples are drawn from the same parent distribution. The empirical distribution function, $F(x)$, is derived by calculating the fraction of data points (total number of points is N) with a value lower than a specified value.

$$F(x) = \frac{1}{N} \sum_{i=1}^{N} I_{X_i < x}. \tag{2.27}$$

Here, $I_{X_i<x}$ is the indicator function which is 1 when $X_i < x$ and 0 otherwise. $F(x)$ is thus a step function beginning at 0 and increasing with $1/N$ for each X_i, until it becomes 1.

For the KS test, the empirical distribution functions for both samples are compared and the KS statistic (D_N) is the largest difference between both, as shown in Fig. 2.6,

$$D_N = \max_x |F(x) - G(x)|. \tag{2.28}$$

If the KS statistic is small, the null hypothesis cannot be rejected. On the other hand, a high KS value does not automatically warrant a rejection of the null hypothesis, as it also depends on the p-value, which gives the probability that the hypothesis can be rejected (or not). A high KS statistic in combination with a p-value ≤ 0.05 means the null hypothesis can be rejected with a probability of $\geq 95\%$.

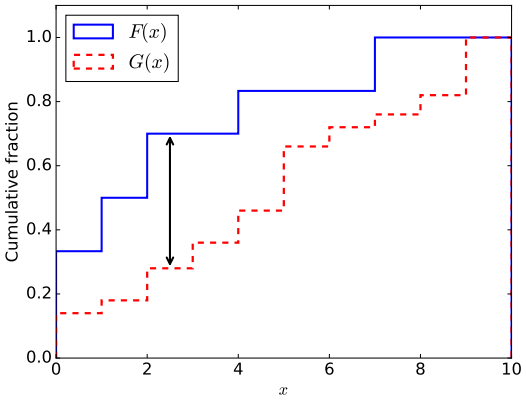

Figure 2.6 — Cumulative distribution functions $F(x)$ and $G(x)$ for two samples and with the KS-statistic indicated by the black arrow.

2.4 The COS instrument

The Cosmic Origins Spectrograph is one of the instruments mounted on the *Hubble Space Telescope* (Dashtamirova et al. 2020). *HST* was launched in 1990 with the space shuttle Discovery. As a space-based telescope, it is not affected by Earth's atmosphere blocking certain wavelengths, meaning it can observe from the UV to the infrared.

Since its launch, five service operations have been made to replace parts and add new instruments to the *HST*. The first was done in 1993, to correct an aberration of its primary mirror. The most recent service operation took place in 2009 and one of its goals was to repair the Space Telescope Imaging Spectrograph (STIS). A complementing instrument is the COS instrument, which was installed during this mission.

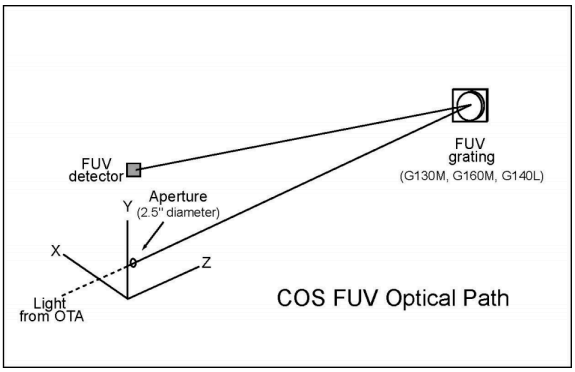

Figure 2.7 — Optical path for the far-UV mode of the COS spectrograph (Fig. 3.3, Dashtamirova et al. 2020).

Among the intended fields of study of COS are the large-scale structure of the Universe and galaxy formation and evolution. COS operates at UV wavelengths, where it has two detectors: one in the far-UV (900−2150 Å) and one in the near-UV (1650−3200 Å). The configuration of the far-UV mode can be seen in Fig. 2.7. Light enters at the *HST*'s optical system (optical telescope assembly; OTA), which has an aperture of 2.5″, and encounters a diffraction grating before reaching the detector. The FUV detector is made out of two separate components, resulting in a small gap in the measured spectrum.

Different gratings provide medium and low-resolution spectra. The spectral resolution (R) of a spectrograph is given by $R = \lambda/\Delta\lambda$, with λ being the wavelength observed and $\Delta\lambda$ the smallest wavelength difference that can be resolved at that wavelength. The gratings used for measurements in this thesis are the G130M and the G160M gratings, which have resolving powers of $R = 12,000$-$16,000$ and $13,000 - 20,000$, respectively. The

spectra for the G130M grating cover the wavelength range 1150−1450 Å and the spectra obtained with the G160M grating cover 1405−1775 Å. An example of a COS fUV spectrum can be seen in Fig. 2.8. Unlike most spectrographs, light does not pass a slit before encountering the detector, but instead COS has a very small field of view. In addition to the spectroscopy mode, the near-UV setting also has an imaging mode.

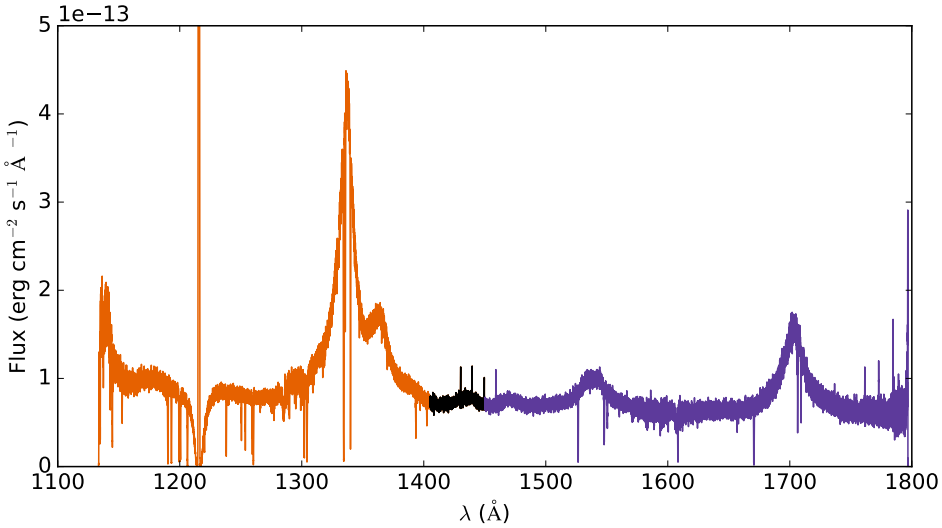

Figure 2.8 — Spectrum of the QSO PG0804+761 with the wavelength range covered by the G130M grating in orange, that of the G160M grating in purple and the overlapping region in black. Galactic Lyα absorption and emission can be seen at 1216 Å as well as various other emission and absorption features.

The COS instrument is still operational at this time and started Cycle 28 on the 1st of October 2020.

2.5 Galaxy catalogues

In this study, spectrographic data on gas is combined with galaxy data from the V8k catalogue (Tully et al. 2009). At a first impression, making a catalogue of galaxies might appear straight-forward, but this section will go deeper into their limitations.

In general, catalogues can be divided in two types: pencil-beam and wide-field. Pencil-beam catalogues focus on a small area of the sky, but go to larger distances/depth, while wide-field catalogues cover a large area, but are not as deep. An important factor in both types is up to which luminosity (at a certain distance) they are complete. Some catalogues, like the V8k catalogue, focus on more luminous galaxies and will miss most dwarf galaxies. These fainter galaxies will also escape detection when they are located at larger distances.

In addition to information on the luminosities of galaxies, their velocities also give valuable information. These velocities are a combination of the Hubble flow velocity and the galaxy's peculiar velocity. For relatively nearby regions, the peculiar velocity can be a significant part of the total velocity, making it more complicated to derive accurate cosmological distance estimates. For example in the Virgo Cluster, the gravitational attraction between the members combined with their relative proximity means peculiar

velocities dominate over the velocities caused by the Hubble flow (e.g. Karachentsev & Nasonova 2010).

The catalogue used in this study is the V8k catalogue, which is combined of several other catalogues and can be found online as part of the Extragalactic Distance Database (Tully et al. 2009). While it does not include dwarf galaxies, it provides a relatively uniform sky coverage for galaxies up to 8000 km s^{-1} (Courtois et al. 2013) and as such gives a good overview of the large-scale structure of the nearby Universe.

3 High-velocity clouds in the Local Group

Published as: **A population of high-velocity absorption-line systems residing in the Local Group**, S. J. D. Bouma, P. Richter, and C. Fechner 2019, A&A, Volume 627, A20

3.1 Introduction

Since the first discovery of high-velocity clouds (HVCs) by Muller et al. (1963) in the Milky Way (MW) halo, their origin has been a matter of debate. These HVCs are seen in 21cm emission or in ultraviolet or optical absorption at radial velocities $|v_{LSR}| > 90-100$ km s^{-1}. Already more than 50 years ago, Oort (1966) made a list of their possible origins; he suggested that they might be parts of supernova shells, intergalactic gas that is being accreted by the MW, small satellite galaxies of the MW, or independent galaxies of the Local Group (LG). As we know today, most HVCs have low metallicities (< 0.3 solar, typically; e.g. Gibson et al. (2000); Wakker (2001); Richter et al. (2001); Collins et al. (2007); Fox et al. (2010); Shull et al. (2011)), indicating that they originate from accreted gas, either from satellite galaxies or the intergalactic medium (IGM). The Magellanic Stream (MS), for example, is the result of the gravitational and hydrodynamical interaction between the MW and the Magellanic Clouds (e.g. Putman et al. 1998).

Halo clouds with somewhat lower velocities, namely the intermediate-velocity clouds (IVCs; $40-50 < |v_{LSR}| < 90-100$ km s^{-1}), often appear to be associated with a so-called Galactic fountain. In the Galactic fountain model (Shapiro & Field 1976; Fraternali & Binney 2008), gas is blown out by superbubbles (created by supernova explosions), mixes with the ambient coronal gas, cools, and falls back onto the disc. The relatively high metallicity found in many IVCs (Wakker 2001, and references therein) further supports a Galactic origin of the IVCs as part of the Galactic fountain model. This model, however, does not explain HVCs, thus making it likely that their origin is not within the disc or bulge of the MW (Marasco et al. 2012). Some HVCs may be explained by Galactic rotation, but only when systematic peculiar velocities are assumed. An example is the Outer Arm HVC being an extension of the Outer Arm (Haud 1992).

One of the keys to our understanding of the origin and nature of HVCs is knowing their distances from us. Most HVCs are located within 20 kpc and relatively close to the MW disc (Wakker 2001; Thom et al. 2006, 2008; Wakker et al. 2007, 2008), but some clouds possibly lie outside of the virial radius of the MW (Sembach et al. 2003; Richter et al. 2017). These distant clouds could be evidence that some HVCs have a LG origin.

Blitz et al. (1999) proposed that some of the compact HVCs (CHVCs) represent distant (extragalactic) clouds confined by dark matter mini-halos that are moving towards the LG barycentre. This theory has been disputed, however, as stellar components have not been found in these HVCs (Simon & Blitz 2002; Hopp et al. 2003) and the nearby M31 does not show any significant CHVC population at large galactocentric radii (Westmeier et al. 2008).

In addition to distance, the kinematics of HVCs can also help in understanding their origin. As pointed out by Nicastro et al. (2003), high-velocity O VI absorption in the MW halo has negative velocities for absorbers located between $0° \leq l \leq 180°$, while the systems on the other half of the hemisphere have mostly positive velocities. This trend disappears when velocities are transformed to the Local Group Standard of Rest (LGSR) frame. Furthermore, using the LGSR or Galactic Standard of Rest (GSR) decreases the amplitude of the average velocity vector of the halo O VI absorption when compared to the LSR. Another, much more detailed study of O VI absorption in the halo (Sembach et al. 2003) confirms that the dispersion around the mean velocity of their absorption systematically decreases if the LSGR or GSR is taken as reference frame. These results indicate that at least one subset of the high-velocity O VI absorbers may not be located in the MW, but rather these absorbers are spatially and kinematically associated with gas filling the LG.

Following up on this, Richter et al. (2017, hereafter R17), in their all-sky HVC absorption survey, compared the absorption velocities of HVCs in the direction of the LG barycentre ($l < 180°$, $b < -30°$) to those of HVCs at $l > 240°$, $b > 60°$ in low and intermediate ions such as Si II and Si III. A velocity dipole is clearly visible: the gas in the direction of the barycentre has negative velocities up to $v_{LSR} = -400$ km s^{-1}, while in the opposite direction the velocities are positive up to $v_{LSR} = +300$ km s^{-1}. Since such high radial velocities cannot be explained by Galactic rotation, the observed kinematics of the HVC absorber population could be the result of the MW moving towards the LG barycentre and away from the anti-barycentre direction. In this scenario, gas at rest in the LG barycentre or coming from M31 would have negative velocities as it is coming towards the MW, while LG gas in the anti-barycentre direction would be left behind, leading to positive velocities.

Nearby HVCs are expected to have, on average, lower velocities than those far away; they are also expected to have substantially higher thermal gas pressures as they are located deep within the MW potential well where they are pressure-confined by the ambient hot coronal gas in the outer disc-halo interface. In turn, the very low thermal gas pressures measured in earlier HVC studies in the high-velocity barycentre absorbers towards PKS 2155−304 and Mrk 509 ($P/k < 5$ K cm^{-3}; Sembach et al. 1999; Collins et al. 2004) indicate that these clouds cannot reside in the inner halo (as they would collapse rapidly), but are located in the outer Galactic halo or even beyond the MW virial radius in the LG, where the thermal pressures are at least two orders of magnitude lower than in the inner halo (Miller & Bregman 2015; Wolfire et al. 1995).

Finally, an LG origin of barycentre/anti-barycentre high-velocity absorbers is also supported by the ionisation structure of the absorbing gas (as indicated by the column density ratios of low and high ions; see R17) and, in the case of the barycentre clouds, the lack of a two-phase structure of the high-velocity clumps seen in H I 21cm emission (Winkel et al. 2011).

Table 3.1 — Atomic data for absorption lines

Ion	λ_0 [Å]	f
C II	1334.53	0.1284
C IV	1548.20	0.1897
C IV	1550.77	0.0947
Si II	1190.42	0.2919
Si II	1193.29	0.5824
Si II	1260.42	1.1762
Si II	1526.71	0.1328
Si III	1206.50	1.6273
Si IV	1393.76	0.5126
Si IV	1402.77	0.2541

Notes. Data compiled from Morton (2003)

In this study, we investigate in more detail the physical conditions of the barycentre/anti-barycentre high-velocity absorbers identified in R17 to further explore a possible LG origin of these clouds. To this end, we re-analyse high-velocity absorption along 29 sightlines and model the absorber structure and the ionisation conditions in the gas. Our paper is organised as follows. In Sect. 2 we describe the absorber sample and the analysis methods. In Sect. 3 we present the results of our absorber-modelling analysis. We present the ionisation modelling of the absorbers in Sect. 4. In Sect. 5, we discuss the implications of our results with regard to distance and origin of the absorbers. A summary of our study is given in Sect. 7.

3.2 Data acquisition and spectral analysis

The 29 active galactic nucleus (AGN) sightlines that are considered in this paper represent a subsample of the 262 sightlines used in the HST/COS Legacy Survey of HVCs presented in R17. For the LG barycentre direction ($l < 180°$, $b < -30°$) our sample includes 19 sightlines; for the LG anti-barycentre direction ($l > 240°$, $b > 60°$) we have 10 sightlines available. Names and Galactic coordinates of the 29 AGNs are given in Table A1 in the Appendix. Their sky distribution, with offsets when one sightline has several absorption components, is shown in Fig. 3.1.

The original HST/COS data were retrieved from the HST Science Archive at the Canadian Astronomy Data Centre (CADC) and reduced following the strategy described in R17. Most of the COS spectra used here have data from the G130M and G160M gratings, but for ten sightlines only G130M data are available. The COS G130M grating covers a wavelength range of 1150 − 1450 Å. This range includes the absorption lines of Si II, Si III, Si IV, and C II. Absorption in the important C IV doublet falls into the range of the COS G160M grating, which covers λ = 1405 − 1775 Å. The resolving power for both gratings is $R = 16,000 - 21,000$ (Green et al. 2012; Fischer et al. 2018). Table 3.1 lists wavelengths and oscillator strengths of the transitions used in this study to measure the above-mentioned ions of Si and C. We include Si IV in our analysis here; it is not covered in our progenitor study (R17).

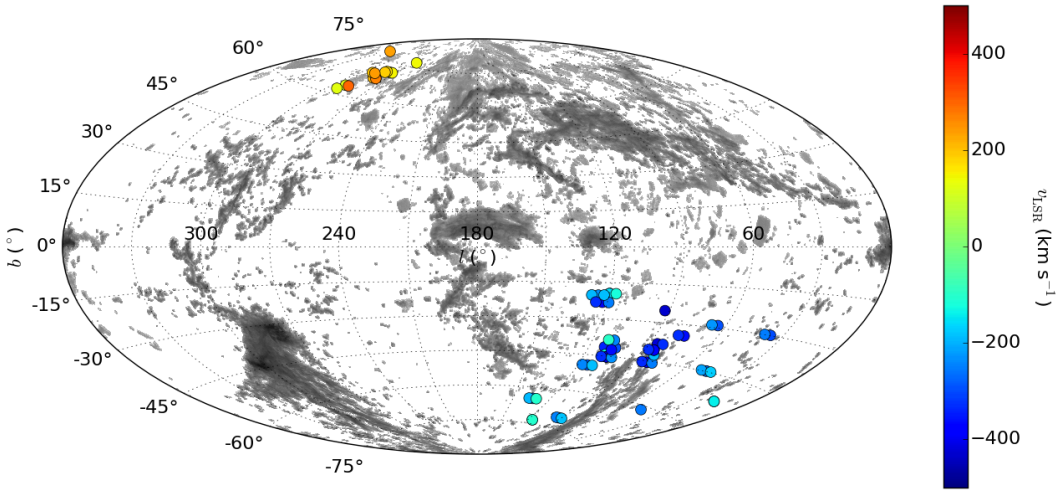

Figure 3.1 — Sky distribution of the AGN sightlines considered in this study in Galactic coordinates. The colour indicates the observed LSR velocity of the high-velocity components seen in these directions. As can be clearly seen, the high-velocity absorbers form a velocity dipole on the sky along the LG major axis (see R17). H I 21 cm data from Westmeier (2018) is added in greyscale.

All COS spectra were normalised using the custom-written `span` code (Richter et al. 2011). While in R17 we used the apparent optical depth (AOD) method to measure velocity-integrated column densities for the various metal ions in the high-velocity absorbers, here we model in detail the velocity-component structure of the absorbers using the component-modelling method (Richter et al. 2013). For this, a synthetic spectrum is constructed from a component model for each absorber, so that it matches the observations. For each velocity sub-component of an HVC absorber the component model defines the velocity centroid, the Doppler parameter/b-value, and the column density of the various ions as input parameters. This method is necessary for our purpose as the physical conditions are expected to vary along the individual sub-components. It should be noted that our aim is to treat each individual absorption sub-component as an individual cloud for which we model the local ionisation conditions. Another advantage of using the modelling approach is that blended lines can be reproduced with a synthetic spectrum, providing additional constraints on the derived column densities and b values.

In this study, we concentrate on HVC absorbers that form the velocity dipole in the LG barycentre and anti-barycentre direction (R17). For the LG barycentre direction region at $l < 180°$, $b < -30°$ we therefore consider only high-velocity absorbers with negative velocities. In the direction of the anti-barycentre at $l > 240°$, $b > 60°$, we consequently only consider HVCs with positive LSR velocities.

In Fig. 3.2 we show a typical example for our modelling approach for the high-velocity absorbers at -294 km s^{-1} and -223 km s^{-1} in the direction of the quasar Mrk 1513. All modelling results (component velocities and column densities for each ion) are listed in Table A1 in the Appendix. Further details regarding the modelling method can be found in Richter et al. (2013).

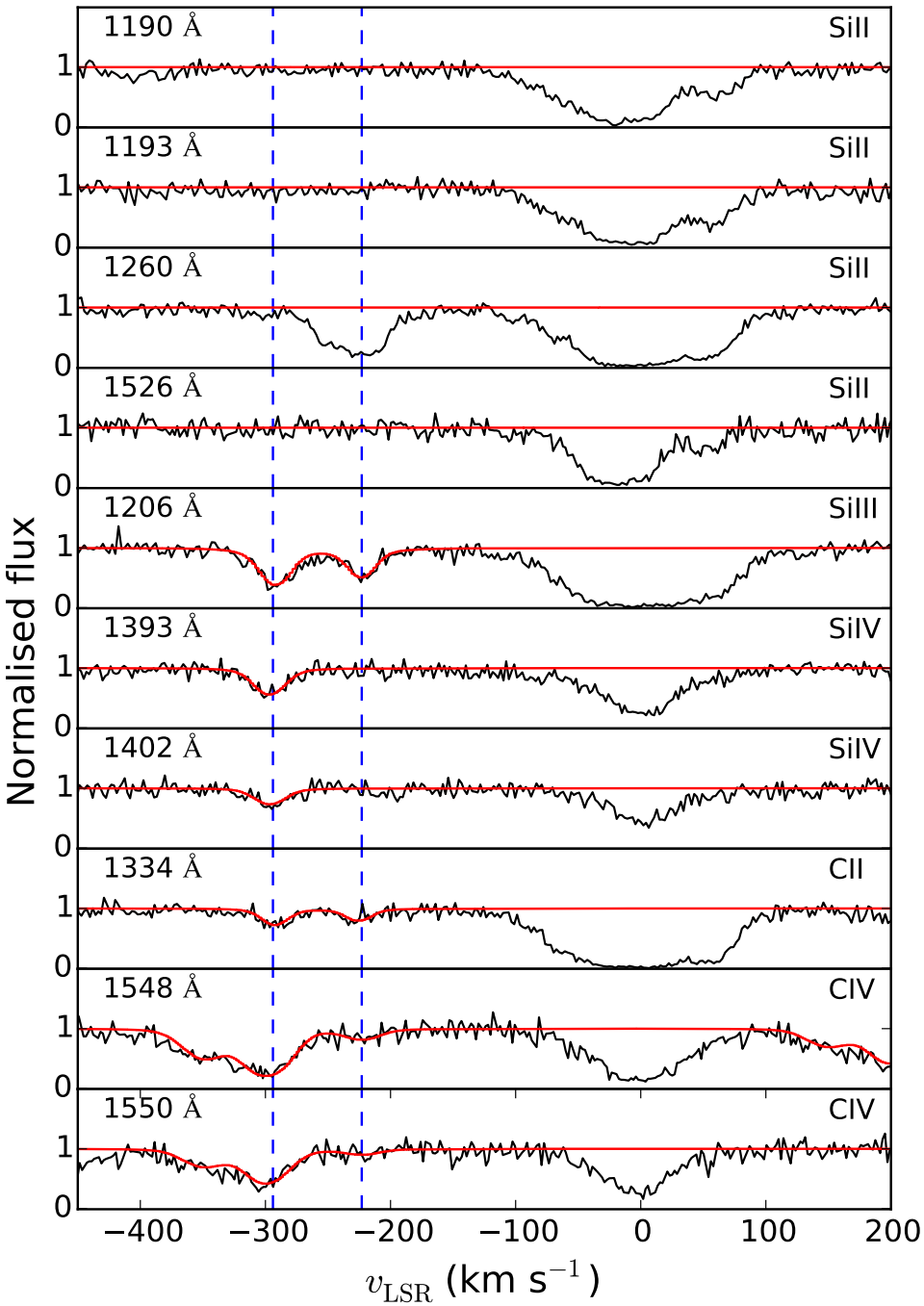

Figure 3.2 — Example for the simultaneous modelling of high-velocity absorption components in COS spectral data. Shown is spectrum of Mrk 1513 for the various ions considered in our study, plotted in LSR velocity space (black solid line). The synthetic model spectrum (red solid line) accurately reproduces the high-velocity absorption in the 2 high-velocity components at −294 and −223 km s^{-1} seen in this direction, which are indicated with blue dashed lines.

3.3 Results from the absorption-line analysis

Along the 19 sightlines towards the LG barycentre, 55 high-velocity absorption components with $v_{\rm LSR} \gtrsim -100$ km s^{-1} are identified. One of these components has large uncertainties due to blending and low S/N and therefore is not considered hereafter. All the sightlines in the LG barycentre direction show at least one high-velocity absorption component, with 17 sightlines having at least two absorption components. Therefore, the observed HVC sky covering fraction in this direction is 100 % in our COS sample.

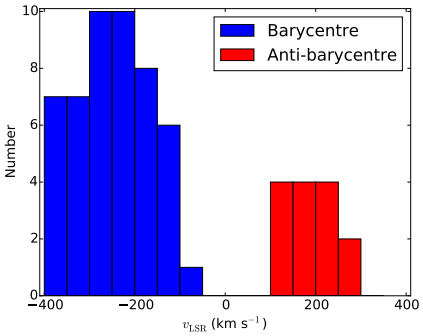

Figure 3.3 — Velocity distribution of the detected 68 high-velocity absorption components in the LG barycentre/anti-barycentre direction. Absorbers in the barycentre direction are shown in blue and those in the anti-barycentre direction in red.

In the anti-barycentre direction, our sample of ten sightlines exhibits 14 individual high-velocity components at $v_{\rm LSR} \geq +100$ km s^{-1}. Positive high-velocity absorption is present in all of these sightlines, implying an HVC sky covering fraction of 100 % in our data set, with four of the ten sightlines having at least two high-velocity absorption components. The barycentre sightlines show more absorption components (with negative velocities) per sightline than the anti-barycentre sample does for positive velocities.

In Fig. 3.3, we show the velocity distribution of the 68 high-velocity absorption components in our sample as a histogram. Absorption in the barycentre sample has velocities spanning the entire velocity range used, from ~ -100 km s^{-1} down to -400 km s^{-1}, while the anti-barycentre sample does not have velocities higher than about $+300$ km s^{-1}. For both samples, the absorption systems are quite evenly distributed over the velocities, although the barycentre sample has most systems in the bins between $|v_{\rm LSR}| = 200-300$ km s^{-1}, which is where the anti-barycentre sample drops off slightly.

In Fig. 3.4, we compare the column density distribution of the barycentre-absorption components (blue) with the that of the anti-barycentre components (red) for the five different ions considered in our study. The two carbon ions that have been measured, C II and C IV, span a range of slightly higher column densities ($\log N \sim 13-15$) than the three silicon ions Si II, Si III, and Si IV ($\log N \sim 12-14$), owing to the higher cosmic abundance of C. Only 34 of the 51 high-velocity components for which G160M data are available show C IV absorption. Likewise, only 30 of the 67 C II/Si II/Si III HVC components are detected in Si IV. One HVC component is only observed in Si IV and C IV. One explanation for the relatively low detection rate of high ions in this sample and in the all-sky survey (R17) might be that they preferentially arise in low-density environments, for example the diffuse outer layers of 21cm HVCs, and in diffuse halo structures far away from the Galactic plane (Sembach et al. 1999; Collins et al. 2005).

The ratio of Si II to Si III is shown in Fig. 3.5. The barycentre sample shows a lower ratio than the anti-barycentre sample, indicating that the gas detected in the barycentre sample is more highly ionised.

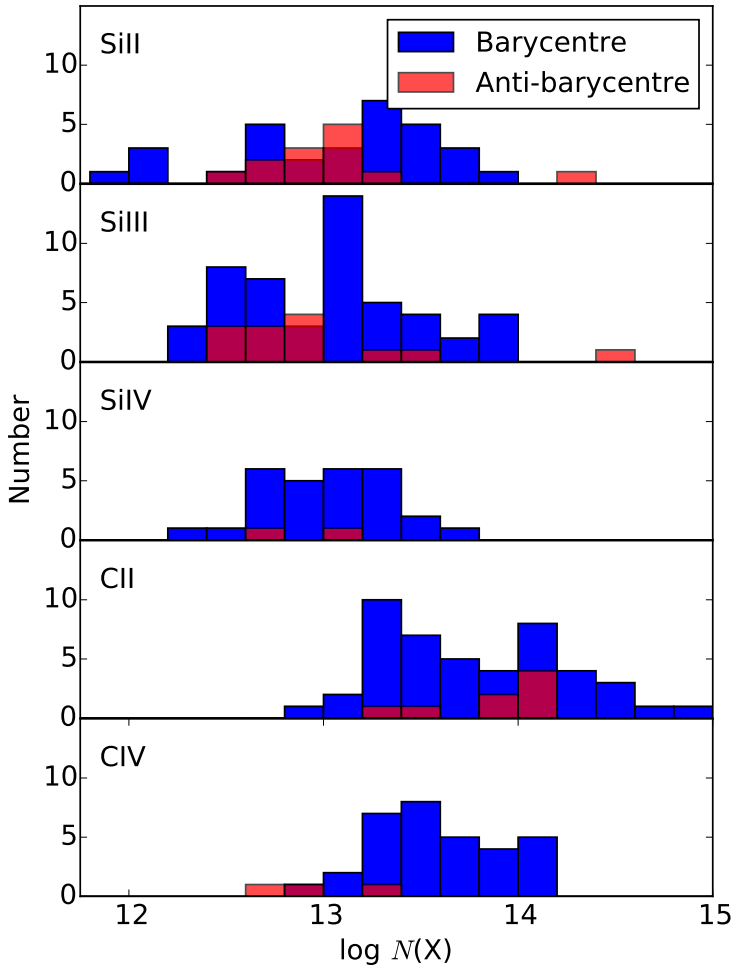

Figure 3.4 — Column density distribution for measured ions for the LG barycentre and anti-barycentre directions. The barycentre sample is in blue and the anti-barycentre sample in red.

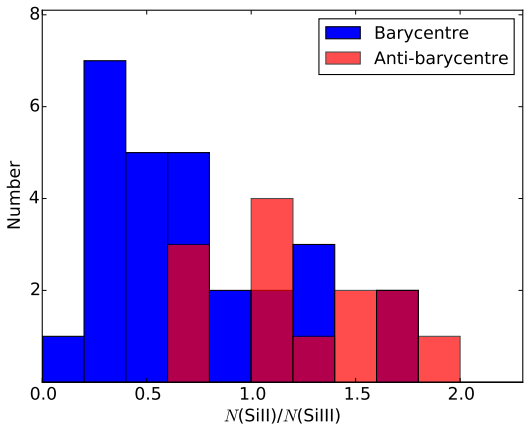

Figure 3.5 — Ratio of column densities of Si II to Si III for sightlines in the barycentre and anti-barycentre directions.

3.4 Ionisation modelling

To obtain more precise information about the physical conditions in the identified high-velocity absorption components we constructed photoionisation models using the Cloudy code version 17.00 (Ferland et al. 2013). For a given ionisation model usually defined by the background ionising radiation field, the absorber geometry, the neutral gas column density, the gas temperature, and the metallicity, Cloudy delivers predictions for the column densities of metal ions as a function of the gas density and ionisation parameter, $U = n_\gamma / n_{\rm H}$. In turn, an observed set of ion column densities in an absorber can be used together with Cloudy to constrain the local gas density. In our case the observed ion column densities (or limits) for Si II, Si III, Si IV, C II, and C IV are used to constrain the gas density in the high-velocity absorption components in our sample. A similar strategy was also used in many of our previous HVC absorption studies (e.g. Richter et al. 2009, 2013; Fox et al. 2010, 2013, 2014).

In our grid of Cloudy models, the absorbing clouds are assumed to be plane-parallel slabs illuminated on both sides by the local ($z = 0$) UV background radiation from Haardt & Madau (2012). For the modelling we do not consider ionising radiation coming from stars in the MW and in M31, due to the unknown location of the absorbers with respect to their stellar discs. As shown in the MW radiation models by Fox et al. (2005, 2014), the contribution of the local (stellar) radiation field in MW-type galaxies is relevant for CGM absorbers within ~ 100 kpc of the plane, and depends on the position of the cloud with respect to the disc. The assumed flux of ionising photons in our Cloudy models therefore represents a lower limit. This needs to be kept in mind when it comes to the interpretation of the derived gas densities and thermal pressures from our models. We will discuss these issues further in Sect. 5.1.3.

The column densities for the above-listed ionisation states are modelled for different ionisation parameters and volume densities of hydrogen assuming a constant gas temperature of 10,000 K and relative solar abundances as given in Grevesse et al. (2010). A temperature of $\sim 1-2\times10^4$ K is typical for photoionised circumgalactic gas (e.g. Richter et al. 2016), and similar temperatures have been derived in previous studies of individual HVCs in the LG barycentre and anti-barycentre directions (Collins et al. 2005; Sembach et al. 1999). Since we do not have information on the H I column density for most of the absorbers in our sample, we fix the overall metallicity of the gas to a value of $Z_X = 0.1$ to indirectly constrain $\log N$(H I) from the observed ion column densities. A metallicity of $Z_X = 0.1$ is characteristic of many of the most distant HVCs, such as the Magellanic Stream, Complex C, and Complex A (Fox et al. 2013; Richter et al. 2001; Sembach et al. 2004; Wakker et al. 1999).

For some HVCs in our sample, not all elemental abundances fit to the same Cloudy model, suggesting a multiphase-nature of these absorbers. A similar behaviour has also been found in CGM absorbers around other galaxies (see detailed discussion in Richter et al. 2016). More highly ionised species are likely to be found in the outer parts at lower hydrogen volume densities ($\log n_{\rm H}$), while the less ionised species are found in the cloud cores at higher $\log n_{\rm H}$. However, because not all multiphase clouds necessarily have this (rather oversimplified) internal structure and because Si is also affected by dust depletion effects, our strategy is to fit the Si and C ions independently and then evaluate possible discrepancies with respect to dust depletion and column density errors for each absorber individually. Si IV and C IV are matched together only when Si II, Si III, and C II match the same model at the same $\log n_{\rm H}$. For all models, Si III is used as an

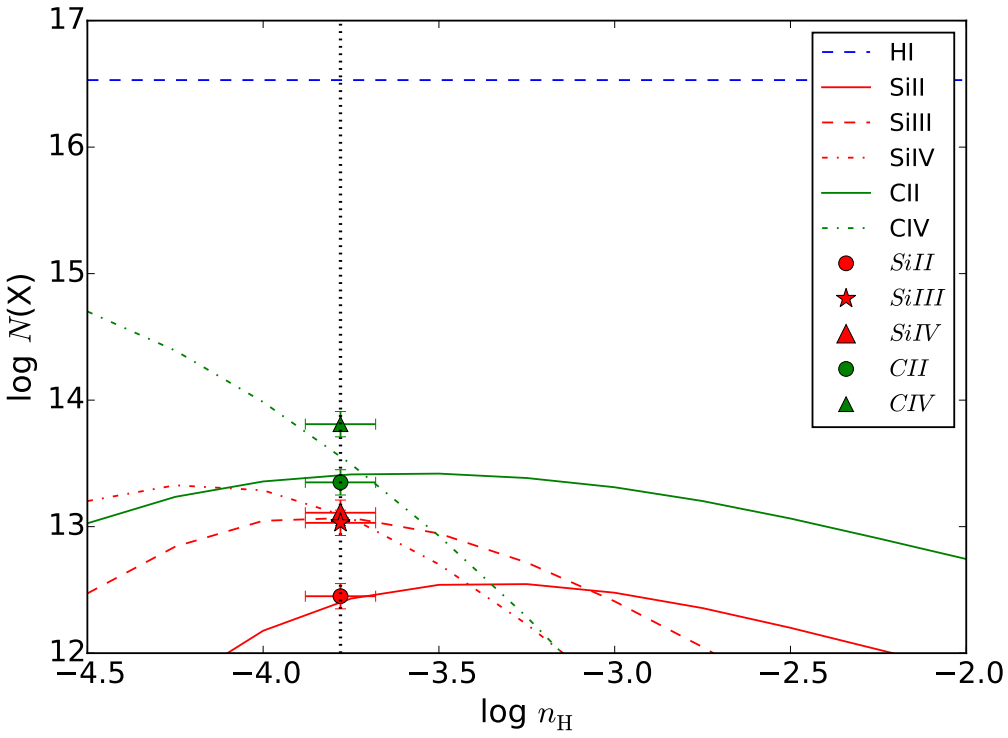

Figure 3.6 — Cloudy model for the HVC at $v_{LSR} = -257$ km s^{-1} in the direction of MR 2251-178. Solid, dashed, and dash-dotted lines represent column densities predicted by the Cloudy model for different ions, while the symbols (dots, star, and triangles) show the measured values. This model, with log N(H I) = 16.53, fits Si II, Si III, Si IV, and C II at log $n_H = -3.78$, which is indicated by the black dotted line.

anchor-ion as it is detected in all but one of the 54 HVCs (and for all HVCs in the anti-barycentre direction). The log n_H derived for the one HVC component without Si III is not considered as the more highly ionised Si IV and C IV trace a different gas-phase. For two barycentre HVCs and one anti-barycentre HVC, Si III was the only securely detected ion, making it impossible to obtain log n_H. For 15 additional HVCs (10 HVCs in the barycentre sample and 5 HVCs in the anti-barycentre direction) we did not find satisfying solutions in our Cloudy models (possibly related to blending and saturation problems), so these absorbers are not considered further in our discussion. In Fig. 3.6 we show a typical example for our Cloudy modelling approach. A characteristic error of 0.1 dex is assigned to the column densities of the different ions and for log n_H; this is in agreement with errors found in R17.

For this project, the ionising radiation field of Haardt & Madau (2012) is used. The intensity of this background field is lower than that of the Haardt & Madau (2001) background model and also lower than the value expected from recent measurements of the local HI photoionisation rate (Kollmeier et al. 2014; Wakker et al. 2015; Shull et al. 2015). Generally, a lower intensity of the background field results in higher gas densities. Additionally, the Haardt & Madau (2012) spectrum is harder than the older version, leading to higher metallicities (e.g. Wotta et al. 2019; Chen et al. 2017). To explore the uncertainties related to the scaling and shape of the UV background, as an

example we model the absorber towards MR 2251-178 adopting the Haardt & Madau (2001) background, as implemented in Cloudy as Table HM05. The change in the spectral energy distribution of the ionising radiation leads to changes in the column density curves (see Fig. 3.6). For the HM05 spectrum, the peak of log N(Si II) is closer to the curve of log N(C II). For the MR 2251-178 example system, this results in a density of $\log n_{\rm H} = -3.55$ instead of -3.78, thus a 0.23 dex difference. This difference is rather small, although it should be noted that the choice of the ionising radiation field does affect our results to a certain degree.

3.5 Discussion

3.5.1 Distribution of gas density

In Fig. 3.7, we show the distribution of the derived logarithmic gas densities, $\log n_{\rm H}$, as a histogram. In the barycentre direction (in blue), the densities are spread over a wide range ($\log n_{\rm H} = -2.5$ to -4.0), with more than 35 % of the absorbers having very low densities $\log n_{\rm H} \leq -3.5$. In the anti-barycentre direction the densities are confined to a much narrower range, $\log n_{\rm H} = -2.7$ to -3.3.

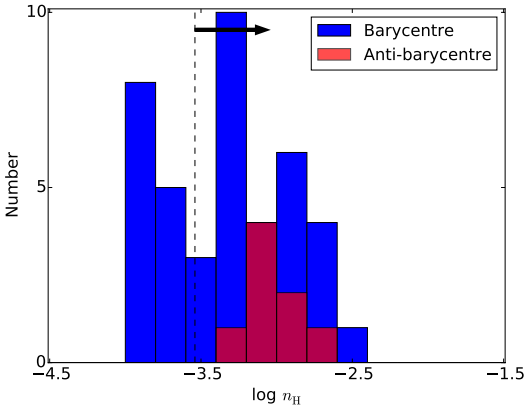

Figure 3.7 — Histogram of logarithmic hydrogen volume densities for 41 HVCs in the barycentre direction (blue) and 8 HVCs in the anti-barycentre direction (red), based on our Cloudy modelling of these absorbers presented in Sect. 4. The black dashed line and the arrow indicate the region for which the MW radiation field plays a role (see Sect. 5.1.3).

HVCs in the barycentre direction

Figure 3.8 shows the hydrogen volume densities for HVCs in the barycentre direction plotted on top of the H I 21cm distribution of high-velocity gas in this region of the sky (grey-shaded areas). There are more HVCs with higher $\log n_{\rm H}$ near the MS and near M31 than in the direction of the Galactic centre negative (GCN) Complex. Distance estimates for Complex GCN range from 15 to 35 kpc, based on computations of a hypothetical orbit that the clouds composing Complex GCN might follow (Jin 2010). If Complex GCN were connected to the Leading Arm of the Magellanic System, as suggested by simulations from Diaz & Bekki (2011), the distances would be between 14 to 22 kpc. However, Complex GCN might instead be a conglomerate of scattered gas clouds with different origins and distances, as pointed out by Winkel et al. (2011). The absorption properties of the GCN absorbers towards Mrk 509 and PKS 2155−304 (Sembach et al. 1999) indicate extremely low gas pressures of $P/k = 1-5$ cm^{-3} K, inconsistent with gas located in the inner ($d < 50$ kpc) MW halo, but instead pointing towards a LG origin for these gas clouds.

Some of the highest densities are found in the absorbers in the general direction of M31 (see Fig. 3.8). These absorbers have relatively low velocities, suggesting that they are close to the MW disc and are not associated with M31 itself. Absorbers near the tip of the MS show the highest velocities. In this region, the MS has velocities in 21cm emission between ~ -250 and -350 km s^{-1} (Kalberla et al. 2005), demonstrating that, from the kinematics, these clouds could well be associated with the MS. However, the absorber at $(l,b) \sim (110,-40)$ has $v_{\rm LSR} \sim -400$ km s^{-1}, indicating that it is not part of the MS. The low densities ($\log n_{\rm H} \sim -3.9$) of some absorbers in this region are also indicative of an extragalactic origin. We will discuss these aspects further in Sect. 5.3, where we include the pressure estimates as additional constraints on the origin of the high-velocity absorbers in the barycentre direction.

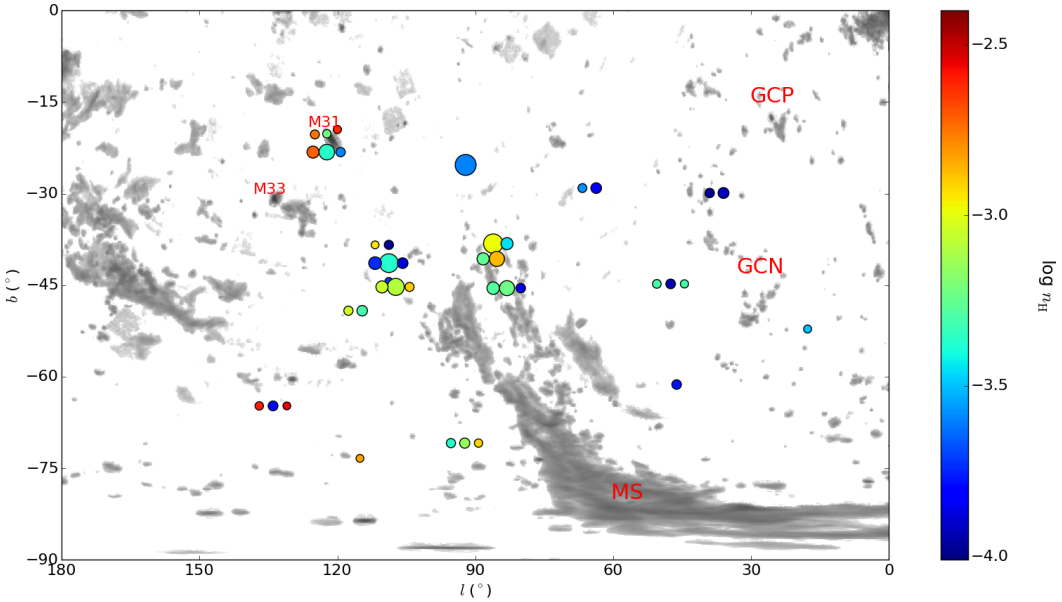

Figure 3.8 — Sky-distribution of gas densities (see vertical bar at right for colour-coding) for 41 HVCs in the barycentre direction with $\log n_{\rm H}$ measured from Si III, overlaid on the H I map with data from Westmeier (2018), which is based on the LAB survey (Kalberla et al. 2005, 2007). For purposes of display, HVCs along the same sightlines have been given an angular offset. The size of the dots scales with the HVC velocity. Important H I complexes are indicated.

HVCs in the anti-barycentre direction

Since in this region there are no prominent clouds seen in the H I 21cm HVC surveys, we do not provide a density map as for the barycentre direction. The sightlines are all relatively close together on the sky and in velocity (Fig. 3.1) and the spread in $\log n_{\rm H}$ is much smaller than for the anti-barycentre sample (Fig. 3.7). This coherency points to a common origin of these high-velocity absorbers as part of a coherent, ionised, high-velocity gas structure located in the inner or outer MW halo.

Role of the Milky Way radiation field

As mentioned above, our ionisation modelling is based on the assumption that the HVC absorbers are only exposed to the extragalactic radiation field at $z = 0$, i.e. any contribution from the MW radiation field has been ignored so far. Since for a given set of input column densities of various metal ions Cloudy delivers the ionisation parameter U as the primary result, there is a degeneracy between the gas density and the intensity of the ionising field in the interpretation of U if Galactic ionising photons are important in addition to the UV background field. This means that the same value for U could be achieved for different combinations of n_γ and $n_{\rm H}$ at different locations inside and outside the MW halo.

Fox et al. (2005, 2014) have modelled in detail the flux of Galactic ionising radiation, demonstrating that the MW radiation field becomes important for galactocentric distances $r \leq 100$ kpc. However, the exact strength of the local radiation field in the MW halo depends strongly on location relative to the Galactic disc. Since we do not know the location (and distance) of the HVC absorbers in our sample with respect to the disc,

the influence of the MW radiation field on the derived HVC gas densities represents a critical aspect in the interpretation of our Cloudy models. To overcome the degeneracy between gas density and photon density we make use of the fact that the gas density in photoionised gas clouds at $T = 10,000 - 20,000$ K situated in a galaxy potential well is constrained by the local gas pressure, which is expected to decline rapidly with increasing galactocentric distance. For a fully ionised gas containing 10 % helium, the thermal gas pressure P is given by the relation $P/k = 2.3\, n_{\rm H}\, T$, where k is the Boltzmann constant, $n_{\rm H}$ the hydrogen volume density, and T the temperature of the gas. From the coronal gas model by Miller & Bregman (2015), it follows that $P/k = Cr^{-1.58}$ or $n_{\rm H} = Dr^{-1.58}$, where C and D are constants with values of $C = 3.31\,10^4$ K cm$^{-1.42}$, $D = 0.435\, C\, T^{-1}$, and r is the galactocentric distance. By combining the density constraints from the Fox et al. (2006, 2014) radiation field model and the Miller & Bregman (2015) pressure relation, we are able to define a threshold value for U that separates absorbers that are potentially influenced by the Galactic radiation field (thus being located at $r \leq 100$ kpc) from absorbers that must be located at $r > 100$ kpc (i.e. absorbers for which no radiation-field or pressure model solution exists at $r \leq 100$ kpc). Taking the extragalactic radiation field as reference, this threshold for U corresponds to a density threshold of $\log n_{\rm H} = -3.54$.

We conclude that all absorbers, for which our initial Cloudy model delivers gas densities $\log n_{\rm H} \leq -3.54$, must be located beyond $r = 100$ kpc, and thus cannot be significantly influenced by radiation from the MW disc. For all other absorbers with $\log n_{\rm H} > -3.54$, we do not know where they are located in the MW halo. They could be either inside or outside $r = 100$ kpc and therefore the gas densities derived for them from our initial UV background Cloudy model must be regarded as lower limits.

3.5.2 Density-velocity plane

A correlation is expected between $v_{\rm LSR}$ and $\log n_{\rm H}$ if high velocity and low density are both signs of clouds being at greater distance. In fact, halo clouds are expected to slow down as they get closer to the Galactic disc because the pressure and density of their surrounding medium increases and so does the effect of ram pressure, which scales with $\rho\, v^2_{\rm infall}$. As a consequence, clouds in the lower halo are expected to have relatively low velocities, while clouds in the outer halo or even beyond can have much higher velocities. Since only the radial component of the space velocity is observed, however, there might be a population of distant clouds that move with high tangential velocities through the outer halo, while we see them as low-velocity HVCs (or even IVCs) because of their small radial velocity component. Clearly, a large sample of MW halo absorbers is required in order to identify possible trends between $v_{\rm LSR}$ and $\log n_{\rm H}$.

It should be noted that the velocities from the HVCs in the direction of M31 are mostly in the range $-250 \lesssim v_{\rm LSR} \lesssim -120$ km s^{-1}, with two HVCs having absolute velocities > 300 km s^{-1}. The systemic velocity of M31 is about -300 km s^{-1} and HVCs with $-300 \lesssim v_{\rm LSR} \lesssim -150$ km s^{-1} might belong to either M31 or its dwarf companions (Lehner et al. 2015). Thus, some of the HVCs in this direction could be part of the CGM of M31 instead of that of the MW.

In the upper panel of Fig. 3.9, we plot $\log n_{\rm H}$ against $v_{\rm LSR}$ for all 49 absorption components. In the lower panel of Fig. 3.9, we bin the data points in 50 km s^{-1}-wide velocity bins, where we regard the individual densities as fixed values (i.e. in this plot we ignore that densities may represent lower limits).

HVCs in the barycentre direction

For the HVCs in the direction of the LG barycentre, the upper panel of Fig. 3.9 indicates a large scatter in the $v_{\rm LSR}$ /log $n_{\rm H}$ parameter plane. This trend is expected from the wide range that the barycentre absorbers cover in velocity (Fig. 3.3) and density (Fig. 3.7). The sample appears to split into two populations: low-density absorbers with log $n_{\rm H} \leq -3.54$ that appear to cluster near $v_{\rm LSR} = -300$ km s^{-1}, and absorbers with high densities (or density limits) that uniformly scatter in the region log $n_{\rm H} > -3.54$ and $v_{\rm LSR} = -100$ to -400 km s^{-1}. The large scatter in log $n_{\rm H}$ is also reflected in the large error bars seen in the binned version (Fig. 3.9, lower panel), which indicate the standard deviation for log $n_{\rm H}$ in each bin. For the barycentre sample, the bin with $v_{\rm LSR} \geq -100$ km s^{-1} has only one HVC, so an error of 0.1 dex is assumed. The same is true for the last bin ($+250 < v_{\rm LSR} < +300$ km s^{-1}) in the anti-barycentre sample. Standard deviations in the other two bins in the anti-barycentre sample are smaller than the size of the symbols. Despite the large scatter, the binned version shows a mild trend where the average density increases with decreasing absolute radial velocity. As mentioned above, this behaviour is expected in the scenario where distant clouds move through the MW halo at higher velocities than the nearby clouds, which are slowed down by ram-pressure forces that act predominantly in the inner halo. While this trend is plausible, here we refrain from a deeper discussion to avoid an overinterpretation of the data. The large scatter in log $n_{\rm H}$ in the overall sample and the fact that for log $n_{\rm H} \leq -3.54$ our Cloudy modelling provides only lower limits if the Galactic radiation field is taken into account (see Sect. 4) may also be responsible for this trend (at least partly), but the influence of these effects on the observed $v_{\rm LSR}$/log $n_{\rm H}$ distribution remains unknown.

The Lee statistics (Lee 1979) can be used to determine whether there are indeed two distinct populations in the density distribution of our absorber sample and to provide an estimate for the characteristic density that separates these two populations from each other (separation value). The first step is to split the sample into two subsamples for different values of log $n_{\rm H}$. Next, the second moment of the total population is multiplied by the total number of data points which is then divided by the sum of values derived on either side of the separation value, resulting in the Lee parameter (L). The value of L will be at its maximum for the most likely separation value (see Fitchett & Merritt (1988) for more details). To evaluate L for our absorber sample, all limits on the gas density are regarded as absolute values. The maximum L comes out to 2.45 and is found at a density of log $n_{\rm H} = -3.44$, while the minimum L is 0.09 at log $n_{\rm H} = -2.44$. The split at log $n_{\rm H} = -3.44$ is marginally higher than the value derived above (-3.54), resulting in two more absorbers being assigned to the low-density subsample. Overall, however, the results from the Lee statistics agree very well with the results based on the estimated influence of the Galactic radiation field (Sect. 5.1.3).

Despite the uncertainties in modelled densities, the existence of a distinct population of barycentre absorbers with log $n_{\rm H} \leq -3.54$ and $v_{\rm LSR} \leq -120$ km s^{-1} is securely constrained by the distribution shown in Fig. 3.9 and further strengthened by the Lee statistics. These results point toward photoionised halo absorbers with very low gas pressures (see discussion in Sect. 5.3).

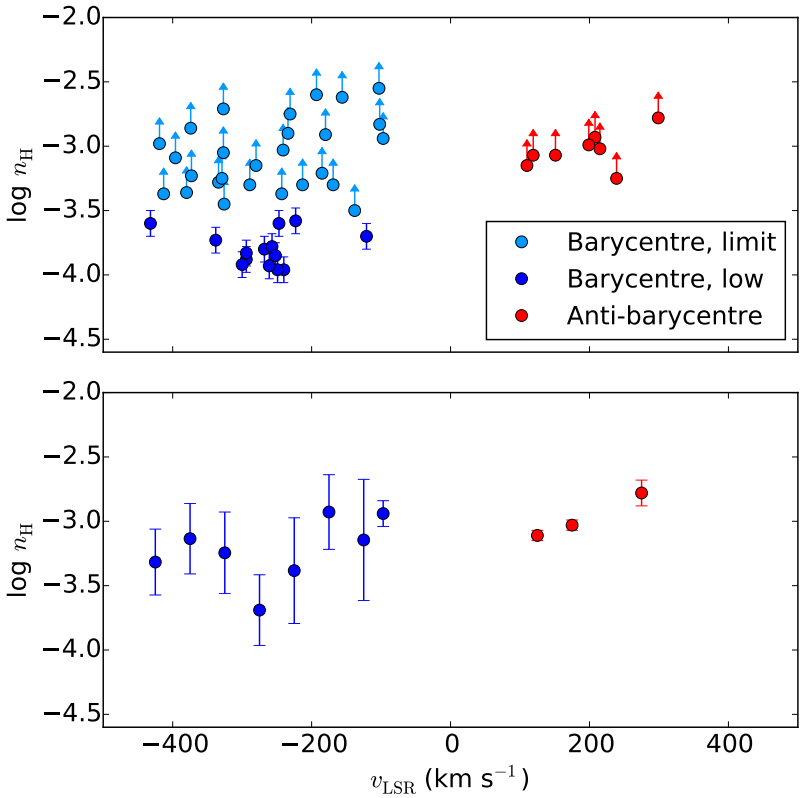

Figure 3.9 — Volume density of hydrogen plotted against $v_{\rm LSR}$ for our HVC absorber sample. The blue data points show the barycentre absorbers, the red data points indicate the anti-barycentre absorbers. The densities are taken from our Cloudy modelling. *Upper panel:* Data points for the 49 HVCs with reliable $n_{\rm H}$ measurements are shown. Lower limits are indicated by light blue symbols and indicated by the arrow. HVCs with $\log n_{\rm H} \leq -3.54$ are shown in dark blue. *Lower panel:* Same as above, but data are binned in 50 km s^{-1}-wide velocity bins. For this plot, we regard the individual densities as fixed values (i.e. in this plot we ignore that densities may represent lower limits)

HVCs in the anti-barycentre direction

For the HVCs in the anti-barycentre direction, all absorbers cluster in the density-velocity plane in the region $v_{\rm LSR} \sim +300$ km s^{-1} and $\log n_{\rm H} \sim -3.0$ with very little scatter (Fig. 3.9, upper and lower panel). Thus, the anti-barycentre absorbers have on average significantly higher densities and lower absolute radial velocities than the barycentre absorbers. This striking asymmetry between barycentre and anti-barycentre HVCs has also been discussed in R17.

It should be noted that the anti-barycentre sample contains only eight absorbers with well-constrained gas densities, compared to the 41 absorbers in the barycentre sample. Only ~ 35% of the barycentre absorbers have low $\log n_{\rm H} < -3.54$.

If the anti-barycentre sample had the same fraction of low-density clouds as the barycentre sample (~ 35% having $\log n_{\rm H} < -3.54$), we would expect to find only three of these systems in the anti-barycentre direction at this sample size. Because of the low

number statistics, we could have missed low-density absorbers in the anti-barycentre direction that are not covered by our sample.

3.5.3 Gas pressures and galactocentric distances

High-velocity clouds are expected to be in pressure equilibrium with their environment, or else they would not exist very long. Since the coronal gas pressure in the inner Galactic halo ($r < 50$ kpc) is expected to be $P/k \gtrsim 100$ K cm^{-3} (Wolfire et al. 1995; Miller & Bregman 2015), HVCs in the inner Galactic halo should have similar pressures. Here we assumed a constant temperature of 10,000 K for the photoionised HVCs. For the errors in the pressure estimates we allowed the temperature to vary in the range $T = 5,000 - 20,000$ K and also considered the individual errors derived for the densities from the Cloudy modelling.

Looking at the range of hydrogen densities (or limits) derived for the barycentre and anti-barycentre sample, all HVCs have pressure values (or lower limits) in the range $P/k \sim 2.5 - 50$ K cm^{-3}, as indicated in Fig. 3.10. For the 41 absorbers in the barycentre direction, for which absolute values of $\log n_{\rm H}$ could be determined (see Sect. 5.1.1), we derived gas pressures in the range $P/k \sim 2.5 - 10$ K cm^{-3}, which is far lower than expected for the inner halo. The lowest pressures were found for the HVCs in the direction of Complex GCN and the HVCs that are (in projection) close to the tip of the MS.

Figure 3.10 shows $v_{\rm LSR}$ plotted against P/k together with a distance scale (dashed green lines), based on the pressure-distance relation described in Miller & Bregman (2015, see their Sect. 5.4). Applying their model to our data, we calculated for each absorber the galactocentric distance (or limit) that corresponds to the derived pressure (or limit). As can be seen, the distances derived for the low-density barycentre HVCs with $\log n_{\rm H} \leq -3.54$ are very large, $r > 200$ kpc, thus beyond the assumed virial radius of the MW.

It should be noted that the Miller & Bregman (2015) pressure model considers only the MW gravitational potential, but not the LG potential, which defines the pressure floor for any gas absorber located inside the LG. The pressure was estimated to decrease from $P/k \sim 10$ K cm^{-3}, at a distance of 200 kpc from the MW centre, to $P/k \sim 0.1$ K cm^{-3} in the LG intra-group medium in the direction of M31 (Nuza et al. 2014; Richter et al. 2017). Therefore, the lowest pressure values derived from our sample correspond to gas outside of the MW's virial radius possibly residing in the LG's intra-group medium.

The low pressures derived here can be compared to CGM clouds within the virial radius of other more distant galaxies. Gas pressures of clouds in the CGM of low-redshift galaxies have been estimated by Werk et al. (2014) and Stocke et al. (2013), indicating $P/k \sim 3 - 100$ K cm^{-3} within the virial radius. Thus, the lowest pressures in our HVC sample fall just below the range suggested for CGM gas in the local Universe.

Two separate HVC populations

From our pressure modelling we conclude that all barycentre HVC absorbers with gas densities lower than $\log n_{\rm H} = -3.54$ (14 absorbers) and that are predominantly associated with Complex GCN and the outer boundary of the MS, are most likely located beyond the MW's virial radius in the LG. For the other remaining barycentre and anti-barycentre absorbers with $\log n_{\rm H} > -3.54$ (35 absorbers) the derived density and pressure limits do not provide constraints on the location of these absorbers inside or outside the MW halo.

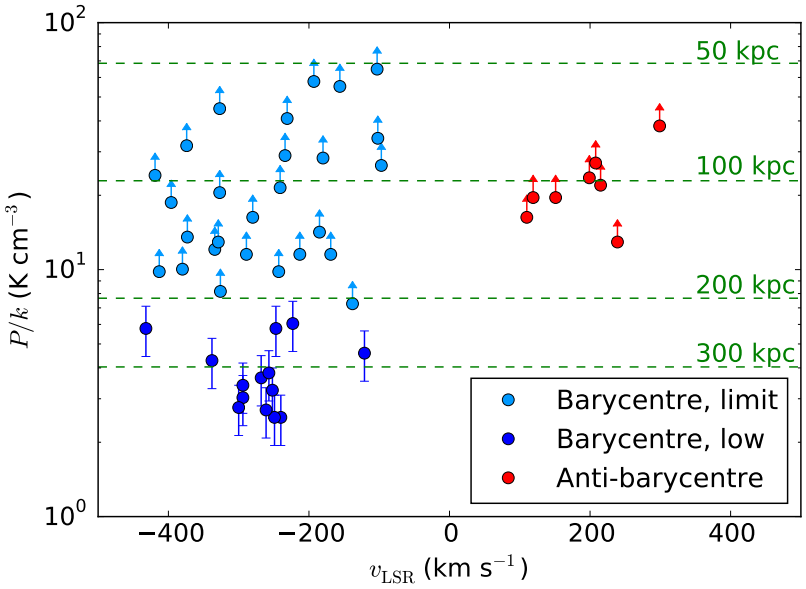

Figure 3.10 — Same as Fig. 3.9, but now with the pressure values, log P/k, on the y-axis. Lower pressure limits are indicated by the arrows (see also Sect. 5.2.1). The dashed green lines show distance-scale based on the halo pressure model from Miller & Bregman (2015).

The barycentre HVCs near Complex GCN and the tip of the MS represent a distinct population of high-velocity absorbers that are peculiar in other properties as well. As discussed in R17, the region near Complex GCN and the tip of the MS contains very little H I 21cm emission, but is very pronounced in O VI absorption (Sembach et al. 2003; Wakker et al. 2003). In addition, the many scattered 21cm clumps do not show the typical two-phase characteristics of nearby HVCs with cold cloud cores and extended diffuse gas layers, indicating that they reside in a very low-density environment.

With only the 14 barycentre absorbers having distinct properties that point to a LG origin, our study does not provide further evidence for the scenario where the observed velocity dipole of HVC absorbers in the barycentre and anti-barycentre absorbers is a result of the overall motion of the MW with respect to the LG's intra-group medium (R17). Since the distances found in our study are derived from the gas densities and pressures, they depend on the background radiation field and the assumed MW halo model, among other assumptions. The low number statistics for the anti-barycentre sample adds to these uncertainties. However, our study also does not exclude such a model and the observed large negative velocities of the LG absorbers in the barycentre direction may well be related to the MW's overall motion towards M31 and its companions (see also Nuza et al. 2014).

3.5.4 Masses and sizes of the HVCs

The sizes and masses of the absorbers can be estimated from log N(H) and log $n_{\rm H}$, based on the values derived from the Cloudy models. We note that a direct measurement of log N(H I) from Lyα absorption is not possible as Galactic disc emission and absorption dominates the Lyα spectrum up to about 400 km s^{-1}. Here we computed sizes and

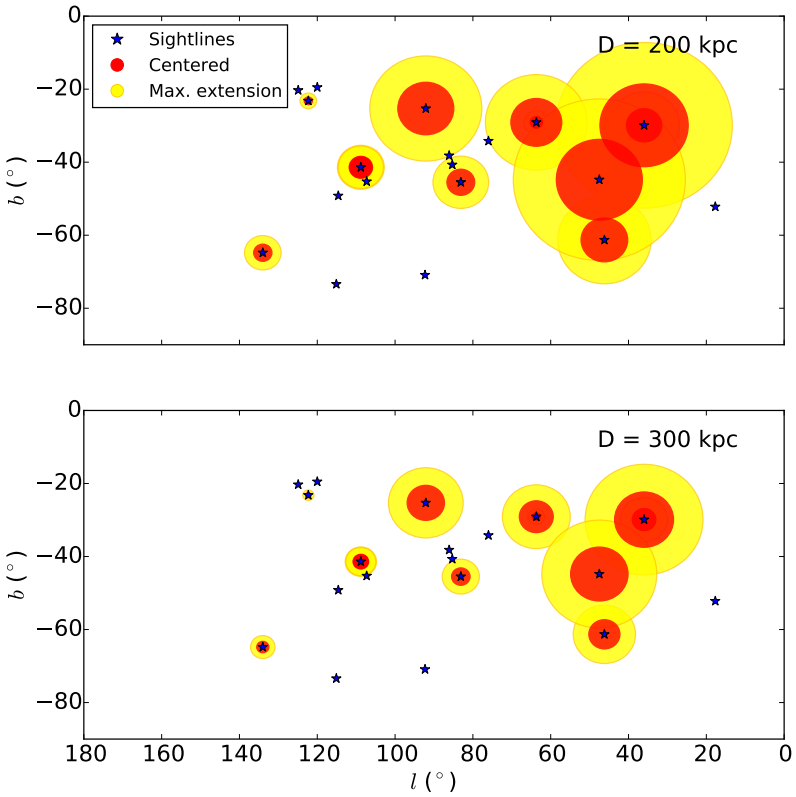

Figure 3.11 — Positions and angular sizes on the sky of the absorbers with $\log n_{\rm H} \leq -3.54$ in the direction of the LG barycentre. For sightlines with multiple low-density absorbers, the one with the largest angular size has been plotted. Red filled circles indicate the size if the cloud were centred on the sightline along which it is detected. Yellow circles instead indicate the maximum extent of the cloud assuming that the AGN sightline passes the edge of the cloud.

masses for the subsample of barycentre clouds with $\log n_{\rm H} \leq -3.54$ by using the Cloudy results in combination with equations (6)-(8) presented in Richter et al. (2009). From this we derived linear diameters between 5 and 39 kpc; the masses range from $\sim 10^5$ to 10^8 $M_\odot$ for the most massive cloud, with the median mass being $4.0 \cdot 10^6$ $M_\odot$. The angular sizes of the absorbers on the sky depend on their distances. Assuming a distance of 200 kpc, the estimated angular sizes are up to 11 degrees. Assuming instead that the absorbers are located at 300 kpc reduces their angular sizes by a factor of 2/3. Figure 3.11 displays the location of the barycentre absorbers on the sky together with their angular sizes.

If we further assume that the absorbers are centred on the AGN sightline along which they are observed, none of the absorbers are expected to cover multiple AGN sightlines. This is true for both 200 kpc and 300 kpc distances, although there are two systems near the tip of the MS where the estimated extent of the clouds almost overlaps with other AGN sightlines. Since these other sightlines do not show low-density absorption, we conclude that these clouds cannot be at distances closer than 200 kpc as they would be picked up by multiple AGN sightlines. This conclusion depends, however, on various assumptions, for instance the assumed spherical geometry of the clouds.

If the absorbers are not centred on the sightline along which which they are detected, there are several cases where clouds may cover multiple sightlines. However, only in the case of the four absorbers in the direction of Complex GCN (see also Fig. 3.8) do the different sightlines all show coherent low-density absorption that could be associated with overlapping absorbers. As seen in Fig. 3.8, these possibly overlapping absorbers in the direction of the Complex GCN all have similar velocities and similar densities. If this is indeed one and the same low-density cloud stretching over multiple AGN sightlines, a distance of about 200 kpc is needed since there is no more overlap at 300 kpc. However, a conglomerate of small clouds with similar properties could also mimic such an absorption pattern. This would fit the picture of the H I gas in this region, as seen in Fig. 3.8.

In conclusion, the estimated masses and sizes do not provide any additional firm constraints on the distance and origin of the barycentre absorbers, but they are fully in line with a LG origin of these clouds, as concluded from the low gas pressures.

3.6 Summary & Conclusions

In this paper, 68 high-velocity absorption systems in a sample of 29 HST/COS spectra were studied to learn more about the origin of these HVCs and their relation to the intra-group medium of the LG. Of these spectra, 19 are in the direction of the LG barycentre and 10 are in the LG anti-barycentre direction. The velocity range studied for the barycentre sample is $-100 < v_{\rm LSR} < -400$ km s^{-1}, while that for the anti-barycentre sample is $+100 < v_{\rm LSR} < +400$ km s^{-1}. We measured column densities for the ions Si II, Si III, Si IV, C II, and C IV in these absorbers by modelling in detail the absorption patterns with synthetic spectra. These column densities were then used together with Cloudy to model the ionisation conditions in the absorbers and to determine the local gas densities, $\log n_{\rm H}$.

The density constraints that we derived from this modelling indicate that the absorbers span a wide range in gas densities from $\log n_{\rm H} = -2.5$ to -4.0. The positive-velocity absorbers all have $\log n_{\rm H} > -3.3$, corresponding to thermal pressures of $P/k > 11.5$ K cm^{-3} for $T = 10,000$ K. These absorbers must be located within $R_{\rm vir} = 200$ kpc of the MW in the inner and outer halo. The negative-velocity absorbers are split into two different populations. One population (27 systems) has $\log n_{\rm H} > -3.54$ and $P/k > 7.3$ K cm^{-3}, thus similar to the positive-velocity absorbers, indicating a location within $R_{\rm vir}$. The other population (14 systems) consists of absorbers with very low gas densities ($\log n_{\rm H} \leq -3.54$) and very low thermal pressures ($P/k < 7.3$ K cm^{-3}), suggesting that these absorbers trace gas situated outside the MW halo in the LG intra-group medium. The derived gas densities and pressures depend on several assumptions, such as the ionising radiation field. Therefore, the derived distances of the absorbers conservatively should be regarded as approximate values. The low-density, low-pressure absorbers appear to be spatially and kinematically connected to HVC Complex GCN and the tip of the Magellanic Stream, but also could lie behind these complexes. A LG origin for these absorbers is further supported by other observed peculiarities, such as the lack of a pronounced core-envelope structure (Winkel et al. 2011) and the excess of O VI absorption (Sembach et al. 2003).

To more precisely pinpoint the exact location of the (predominantly ionised) low-density LG absorbers beyond the virial radius of the MW using the bracketing method (e.g. Wakker et al. 2007, 2008; Richter et al. 2015), combined spectroscopic observations

of the most distant globular clusters and adjacent AGN sightlines are necessary. While the bracketing method can be used for nearby clouds using bright halo stars and AGNs (e.g. Peek 2018), this is not possible for distances near or outside the virial radius. The strategy of using distant globular clusters has to wait for future UV instrumentation, however, as the eligible background sources are too faint to be observed with HST/COS at realistic integration times.

4 Lyα in filaments

Published as: **The relation between Lyα absorbers and local galaxy filaments**, S. J. D. Bouma, P. Richter, and M. Wendt 2021, A&A, in press

4.1 Introduction

It is generally accepted that the intergalactic medium (IGM) contains the majority of the baryons in the universe (e.g. Shull 2003; Lehner et al. 2007; Danforth & Shull 2008; Richter et al. 2008; Shull et al. 2012; Danforth et al. 2016), making it a key component in understanding cosmological structure formation. It is estimated that about 30 % of the baryons at low-z are in the form of photoionised hydrogen at a temperature of $\lesssim 10^4$ K (Penton et al. 2000; Lehner et al. 2007; Danforth & Shull 2008; Shull et al. 2012; Tilton et al. 2012; Danforth et al. 2016), while the collapsed, shock-heated warm-hot intergalactic medium (WHIM) at T $\sim 10^5 - 10^6$ K contains at least 20 % (Richter et al. 2006a,b; Lehner et al. 2007). Cosmological simulations indicate that the WHIM may contribute up to 50 % of the baryons in the low-z universe (Cen & Ostriker 1999; Davé et al. 1999; Shull et al. 2012; Martizzi et al. 2019). This makes the IGM an important reservoir of baryons used by galaxies to fuel star formation. Indeed, to explain current rates of star formation, such a baryon reservoir is needed (e.g. Erb 2008; Prochaska & Wolfe 2009; Genzel et al. 2010). In this way, the evolution of galaxies is tied to the properties and the spatial distribution of the IGM.

The relation between the IGM and galaxies is not one-way, however, as galaxies influence their surroundings by ejecting hot gas into their circumgalactic medium (CGM) via active galactic nucleus (AGN) feedback (e.g. Bower et al. 2006; Davies et al. 2019) and, particularly in the early universe, via supernova explosions (Madau et al. 2001; Pallottini et al. 2014). Thus, there is a large-scale exchange of matter and energy between the galaxies and the surrounding IGM, and each environment influences the evolution of the other. One observational method for studying the gas circulation processes between galaxies and the IGM is the analysis of intervening Lyman α (Lyα) absorption in the spectra of distant AGN, which are believed to trace the large-scale gaseous environment of galaxies. Generally, an anti-correlation between Lyα absorber strength and the galaxy impact parameter is found for absorbers that are relatively close to galaxies (e.g. Chen et al. 2001; Bowen et al. 2002; Wakker & Savage 2009; French & Wakker 2017).

The IGM is not only tied to the galaxies; it is also expected to trace the dark matter distribution and can, therefore, provide insights into the large-scale structure of the universe. This large-scale structure has been mapped by galaxy surveys such as the Two-degree Field Galaxy Redshift Survey and the Sloan Digital Sky Survey (SDSS; Colless et al. 2001; York et al. 2000). Studying the IGM absorber distribution at low redshift allows for a comparison with data from these galaxy surveys. Already more than 25 years ago, Morris et al. (1993) studied the spectrum of the bright quasar 3C 273 and mapped Lyα absorbers along this line of sight together with galaxies in its vicinity. They found that Lyα absorbers cluster less strongly around galaxies than the galaxies do among themselves. This can be interpreted as most of the Lyα absorbers being truly intergalactic in nature, following the filamentary large-scale structure rather than the position of individual galaxies.

More recently, Tejos et al. (2016) studied Lyα and O VI absorption in a single sightline in regions between galaxy clusters. The detected over-density of narrow and broad Lyα absorbers hints at the presence of filamentary gas connecting the clusters. A different approach was taken by Wakker et al. (2015). Instead of mapping gas along an isolated sightline, they used several sightlines passing through a known galaxy filament. By comparing the relation of Lyα equivalent width with both galaxy and filament impact parameters, Wakker et al. (2015) conclude that Lyα absorbers are best described in the context of large-scale structure rather than as tracers of individual galaxy halos. While there is a relation between strong (N(H I) $> 10^{15}$ cm^{-2}) absorbers and the CGM of galaxies, weak Lyα absorbers are more likely to be associated with filaments. This view is also supported by Penton et al. (2002), who find that weak absorbers do not show a correlation between equivalent width and impact parameter to the nearest galaxy, while stronger absorbers do. By comparing the position of their sample of Lyα absorbers relative to galaxies in filaments, they conclude that the absorbers align with the filamentary structure. Evidence for absorbers tracing an extensive, intra-group medium comes from the other recent surveys of Stocke et al. (2013) and Keeney et al. (2018).

While the correlation between the Lyα equivalent width and the galaxy impact parameter seems to indicate that these absorbers are somehow associated with galaxies (e.g. by the gravitational potential), studies such as Wakker et al. (2015) and Tejos et al. (2016) show that at least some of the absorbers are associated with the cosmological large-scale structure. Others studies (Bowen et al. 2002; Wakker & Savage 2009) conclude that their data simply do not yield any definite conclusions on this aspect (see also Penton et al. 2002; Prochaska et al. 2011; Tejos et al. 2014). Therefore, the question of how Lyα absorbers at $z = 0$ are linked to galaxies and the large-scale cosmological structure remains unresolved. Clearly, additional absorption line studies that improve the currently limited statistics on the absorber-to-galaxy-connection are desired.

In this paper, we systematically investigate the properties of $z = 0$ Lyα absorbers and their connection to the local galaxy environments and the surrounding large-scale structure. For this, we follow an approach similar to that of Wakker et al. (2015). We combine the information on local galaxy filaments mapped by Courtois et al. (2013) with archival UV absorption line data from the Cosmic Origins Spectrograph (COS) installed on the *Hubble Space Telescope* (*HST*).

Information on the galaxy sample used in this study is provided in Sect. 2. In Sect. 3, the HST/COS data are described and information on the absorption line measurements is given. Details on the galaxy filaments are presented in Sect. 4. In Sect. 5, we investigate the relation between absorbers and galaxies, whereas in Sect. 6 we focus on the relation

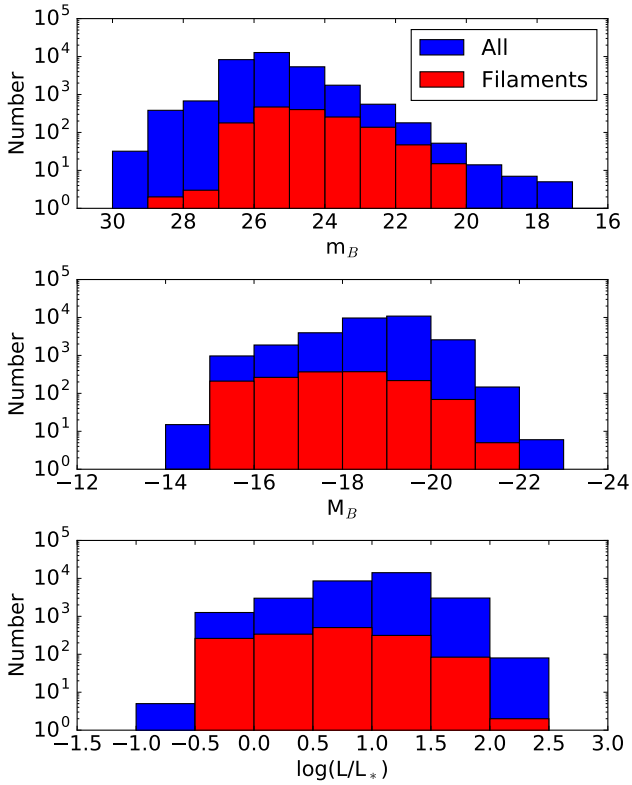

Figure 4.1 — Histogram of apparent and absolute B-band magnitudes and luminosities for all galaxies of the V8k catalogue.

between absorbers and filaments. In Sect. 7, we discuss our findings and compare them with previous studies. Finally, we summarise and conclude our study in Sect. 8.

4.2 Galaxy data

Courtois et al. (2013) used the V8k catalogue of galaxies to map galaxy filaments in the nearby universe. This catalogue is available from the Extragalactic Distance Database[1] (EDD; Tully et al. 2009). It is a compilation of different surveys, including John Huchra's 'ZCAT' and the IRAS Point Source Catalog redshift survey with its extensions to the Galactic plane (Saunders et al. 2000a,b). In total, the catalogue consists of ∼ 30 000 galaxies, all with velocities less than 8000 km s^{-1}. It is complete up to $M_B = -16$ for galaxies at 1000 km s^{-1}, while at 8000 km s^{-1}, it contains one in 13 of the $M_B = -16$ galaxies. A radial velocity of 8000 km s^{-1} corresponds to a cosmological distance of $d \sim (114\ \mathrm{km\,s^{-1}})h_{70}^{-1}$. The distance to the Centaurus Cluster ($v \sim 3000$ km s^{-1}) is ∼ 40 Mpc. As described in Sect. 3, the velocity range studied in this work extends up to $v \sim 6700$ km s^{-1}, which corresponds to $\lambda \sim 1243$ Å. We note that distance estimates to galaxies within 3000 km s^{-1} in the V8k catalogue are adjusted to match the Virgo-flow model by Shaya et al. (1995). The relatively uniform sky coverage – with the exception of the zone of avoidance (ZOA) – of the V8k survey combined with the broad range of galaxy types make it suitable for qualitative work (Courtois et al. 2013).

[1] `http://edd.ifa.hawaii.edu/`

The distribution of apparent and absolute B-band magnitudes as well as $\log(L/L^*)$ for all galaxies of the V8k catalogue is presented in Fig. 4.1. As can be seen from this distribution, the V8k catalogue is largely insensitive to dwarf galaxies with luminosities $\log(L/L^*) \leq -0.5$. This needs to be kept in mind for our later discussion of the absorber-galaxy relation in Sects. 5 and 6. We decided to not add supplementary galaxy data from other surveys because the sky coverage of such a mixed galaxy sample would be quite inhomogeneous, which would introduce an additional bias to the absorber-galaxy statistics.

In the upper panel of Fig. 4.2, we show the sky distribution of the galaxies in the various filaments, as defined in Courtois et al. (2013). The galaxies in these filaments have radial velocities in the range $v = 750 - 5900$ km s^{-1}. All filaments feed into the Centaurus Cluster located at $l \sim 300°$ and $b \sim 20°$. The large concentration of galaxies in the green filament, between $l \sim 260 - 300°$ and $b \sim 60 - 70°$, is due to the Virgo Cluster.

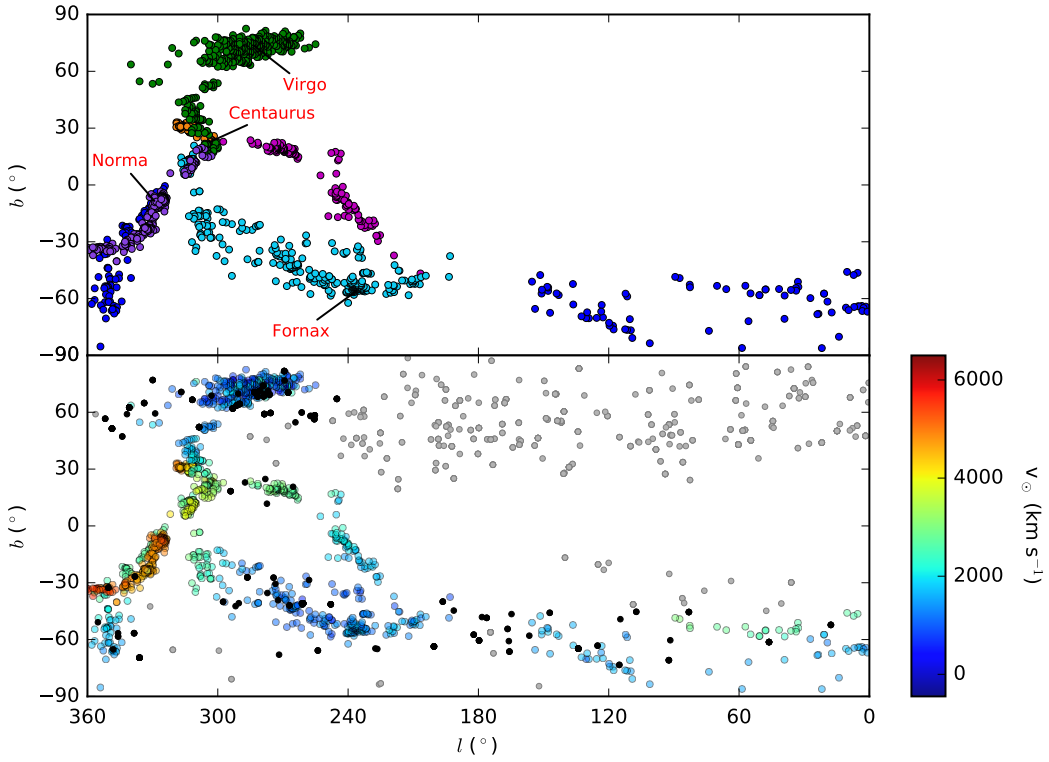

Figure 4.2 — All-sky map of filaments in the local Universe. *Upper panel:* Sky distribution of galaxies from V8k belonging to filaments as defined in Courtois et al. (2013). The different colours indicate different galaxy filaments. Several important clusters are noted. *Lower panel:* Sky distribution of HST/COS sightlines passing close to a filament (black circles) and HST/COS sightlines not belonging to a filament (grey circles) plotted together with the galaxies from the V8k catalogue belonging to filaments (colour-coded according to velocity).

4.3 Absorption line data

4.3.1 HST/COS observations

In this study, we made use of ancillary HST/COS data, as retrieved from the HST Science Archive at the Canadian Astronomy Data Centre (CADC). The total sample consists of 302 quasar (QSO[2]) sightlines, all of which were reduced following the procedures described in Richter et al. (2017).

Since the Lyα absorption (λ_0 = 1215.67 Å) in the spectra studied here falls within the wavelength range between 1215 and 1243 Å, we made use of the data from the COS G130M grating. This grating covers a wavelength range from 1150 − 1450 Å and has a resolving power of $R = 16,000 - 21,000$ (Green et al. 2012; Dashtamirova et al. 2018). The data quality in our COS sample is quite diverse, with signal-to-noise ratios (S/N) per resolution element varying substantially (between 3 and 130; see Fig. B.1 in the appendix.)

We also checked for metal absorption in the Lyα absorbers, considering the transitions of Si III λ1206.50, the Si II doublet λ1190.42; 1193.29, Si II λ1260.42, Si II λ1526.71, the Si IV doublet λ1393.76; 1402.77, C II λ1334.53, and the C IV doublet λ1548.20; 1550.77. For the lines at $\lambda > 1450$ Å, data from the COS G160M grating were used, which covers $\lambda = 1405 - 1775$ Å.

The QSO sightlines are plotted on top of the V8k galaxy filaments in the lower panel of Fig. 4.2. The sky coverage of the sightlines is noticeably better in the upper hemisphere. As can be seen, the majority of the sightlines do not pass through the centres of the filaments, but rather are located at the filament edges.

A reason for sightlines not going directly through filaments could be extinction. This especially holds true for dense regions such as the Virgo Cluster, where the extinction is high. On the other hand, the Virgo Cluster is a nearby cluster and might be better studied than random regions on the sky. From the COS sightlines shown in the lower panel of Fig. 4.2, no clear bias can be seen, except for the northern versus southern hemisphere.

4.3.2 Absorber sample and spectral analysis

For all 302 COS spectra, the wavelength range between 1220 − 1243 Å was inspected for intervening absorption. This range corresponds to Lyα in the velocity range $v \approx 1070 - 6700$ km s^{-1}. At velocities < 1070 km s^{-1}, Lyα absorption typically is strongly blended with the damped Lyα absorption trough from the foreground Galactic interstellar medium (ISM). To ensure consistency, we did not further consider any absorption feature below 1220 Å.

We verified that each detected absorption feature at 1220−1243 Å was Lyα absorption by ruling out Galactic foreground ISM absorption and other, red-shifted lines from intervening absorbers at higher redshift. As for the Galactic ISM absorption, this wavelength range contains only the N V doublet (1238, 1242 Å) and the weak Mg II doublet (1239, 1240 Å) as potential contaminants, and the regions were flagged accordingly. Potential red-shifted contaminating lines that were ruled out include: the H I Lyman-series up to Lyδ, Si III (1206.50 Å), and the two O VI lines at 1037.62 and 1031.93 Å. Whenever possible, we also used the line list of intergalactic absorbers from Danforth

[2]Throughout the following, we use the expression "QSO" as synonym for all types of AGN

et al. (2016), which covers a sub-sample of 82 COS spectra. All in all, we identified 587 intervening Lyα absorbers along the 302 COS sightlines in the range $\lambda = 1220 - 1243$ Å.

For the continuum normalisation and the equivalent width measurements of the detected features (via a direct pixel integration), we used the `span` code (Richter et al. 2011) in the ESO-MIDAS software package, which also provides velocities for the absorbers. To derive the column densities of H I (and the metal ions) for a sub-sample of the identified Lyα absorbers, we used the component-modelling method as described in Richter et al. (2013). In this method, the various velocity sub-components in an absorber are consistently modelled in all available ions (H I and metals) to obtain column densities (N) and Doppler parameters (b-values) for each ion in each component. Throughout the paper, we give column densities in units of [cm^{-2}] and b-values in units of [km s^{-1}]. The modelling code, which is also implemented in ESO-MIDAS, takes into account the wavelength-dependent line-spread function of the COS instrument. Wavelengths and oscillator strengths of the analysed ion transitions were taken from the list in Morton (2003).

The total sample of 302 COS sightlines was separated into two sub-samples, one with sightlines that pass close to a filament and the other with sightlines that do not. To account for the large projected filament widths that are occasionally seen (see e.g. part of the dark blue filament in Fig. 4.2) and to be able to also map the outer parts of the filaments, a separation of 5 Mpc from the nearest galaxy belonging to a filament was chosen as the dividing distance in this selection process. One sightline (towards 4C–01.61) was categorised as belonging to a filament – despite its nearest galaxy distance being as large as 7.9 Mpc – because it passes a filament that is very poorly populated. In total, our selection processes led to 91 sightlines being categorised as filament-related, while the remaining 211 sightlines were categorised as sightlines that are unrelated to the filaments studied here. The total redshift path length in our COS dataset can be estimated as $\Delta z = 0.0189\,N$, with N being the number of sightlines. This gives $\Delta z = 1.72$ and 3.99 for the sightline sample belonging to filaments and the one unrelated to filaments, respectively. This will be further discussed in Sect. 4.7.

Within the sub-sample of the filament-related sightlines relevant for us, 12 spectra were unsuited for absorption line measurements due to various data issues, such as an indeterminable continuum or heavy blending from various lines. Of the remaining 79 spectra, nine had no Lyα absorption features detected in the studied wavelength range. This implies a Lyα detection rate of ~90 % (we will later further discuss the number density and cross-section of Lyα absorbers in this sample). The S/N for these 79 spectra vary between five and 92 per resolution element. In this sub-sample of 79 filament-related sightlines, we identify 215 Lyα absorption systems that are composed of 227 individual components. For these 215 (227) absorbers (components), we derived H I column densities and b-values via the component-modelling method, as described above.

In the other sightline sample, which we categorise as unrelated to the galaxy filaments, 25 spectra were unsuited for measurements for the reasons described above. Of the remaining 186 spectra, only 24 show no Lyα absorption in the range considered above, resulting in an 87 % detection rate for Lyα in this sample.

Metal ions (Si II, Si III, Si IV, C II, or C IV) were detected for 26 of the 215 Lyα filament absorbers, giving a metal detection fraction of ~12 %. Two example HST/COS spectra are shown in Fig. 4.3 (black) together with the synthetic model spectrum (red). These

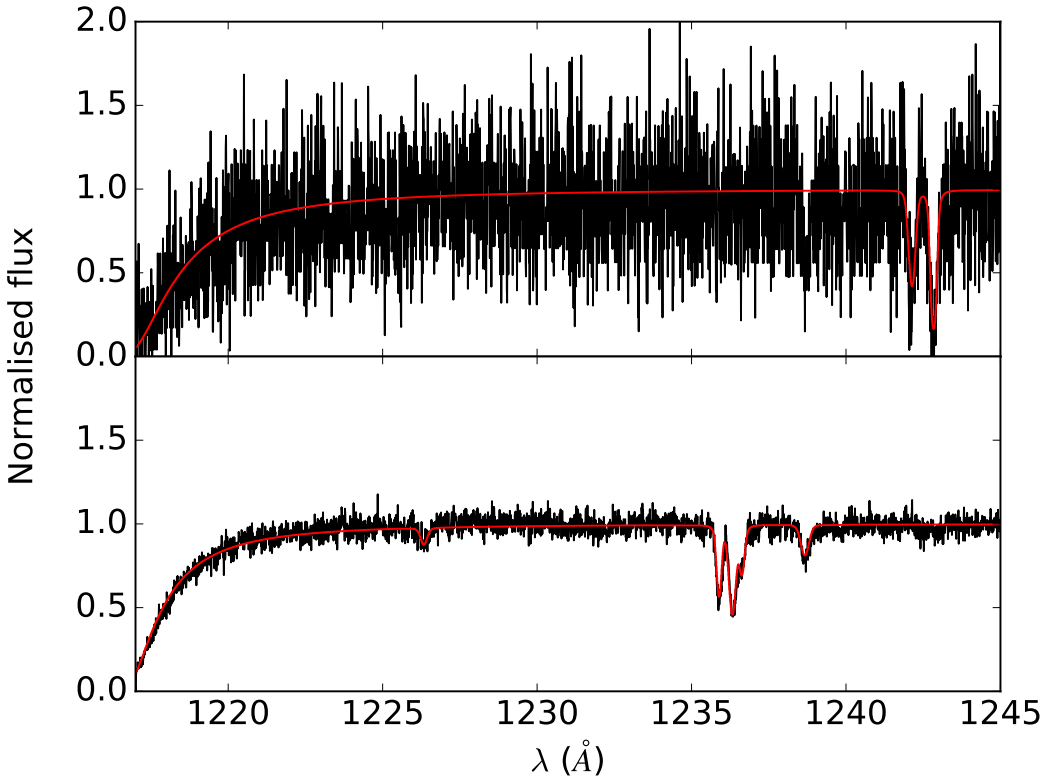

Figure 4.3 — HST/COS G130M spectra of the QSOs VV2006-J131545.2+152556 (upper panel) and PKS2155-304 (lower panel). The COS data are given in black, and the absorber model is plotted in red. Several Lyα absorbers are seen in these spectra. For a better visualisation, both spectra are binned over two pixels.

example spectra give an indication of the characteristic differences in S/N in the COS data used in this study.

The upper panel of Fig. 4.4 shows the distribution of H I Lyα equivalent widths for the detected absorbers in the two sub-samples and in the combined, total sample. The lower panel shows the distribution of H I column densities in the filament-related absorbers, as derived from the component modelling. Both distributions mimic those seen in previous Lyα studies at $z = 0$ (Lehner et al. 2007). The sample of Danforth et al. (2016) with 2577 Lyα absorbers obtained with HST/COS shows a similar distribution with a peak in equivalent width just below 100 mÅ. The H I column density distribution falls off below log N(H I) = 13.5 due to the incompleteness in the data regarding the detection of weaker H I Lyα absorbers. We note that, because of the limited spectral resolution and S/N, many of the broader Lyα lines are most likely composed of individual, unresolved sub-components. The H I column density distribution function (CDDF) will be discussed in Sect. 7.

Errors of the measured equivalent widths have been derived with the `span` code (Richter et al. 2011), which takes into account the S/N around each line, the uncertainty for the local continuum placement, and possible blending effects with other features. Typical 1σ errors for the equivalent widths lie around 20 mÅ. The errors in the column

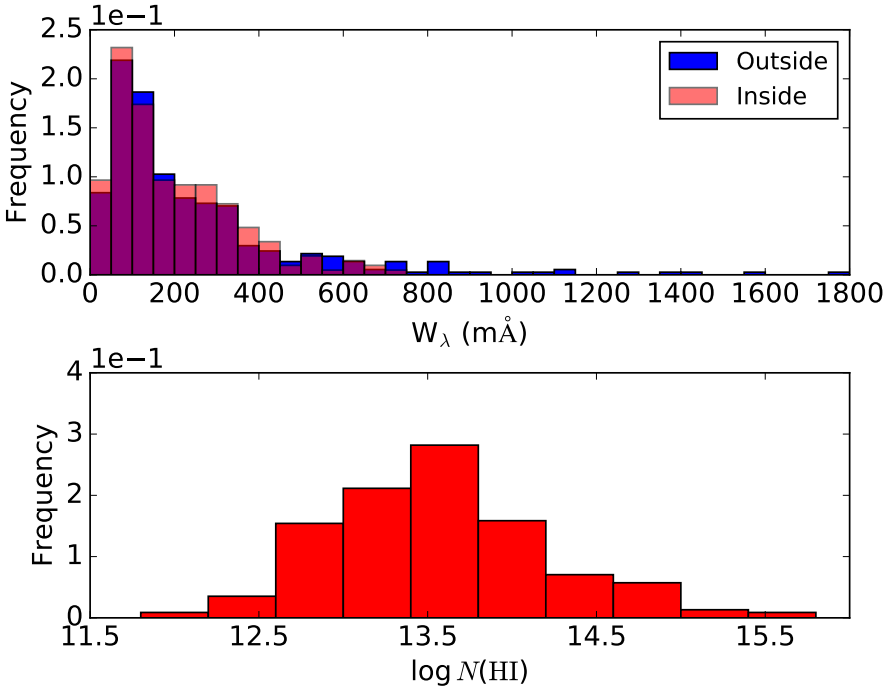

Figure 4.4 — Histogram of equivalent widths of Lyα absorbers (upper panel) and log$N$(HI) in the filament-related absorbers as derived from the component modelling (lower panel).

densities were derived based on the component-modelling method in Richter et al. (2011). Here, the typical errors are of the order of ~ 0.1 dex.

This value is similar to the errors found by Richter et al. (2017) for the same method and a comparable COS dataset. The Doppler parameters have a relatively high uncertainty, especially for higher values of b. With the majority of b-values falling between 10 and 30 km s^{-1}, the errors are typically ~ 5 km s^{-1}, with lower errors for the low end of the range of b and slightly higher errors for larger b-values. Tabulated results from our absorption line measurements can be made available upon request.

4.4 Characterisation of galaxy filaments

To study how the IGM is connected to its cosmological environment, it is important to characterise the geometry of the filaments, their galaxy content, and their connection to the overall large-scale structure. In Fig. 4.5, we show the position of the galaxies in the filaments together with their radial extent shown as 1.5 virial radii (1.5 R$_{\rm vir}$). Gas within this characteristic 'sphere of influence' can be considered as gravitationally bound to that galaxy. This plot therefore gives a first indication of how much uncovered sky there is between the galaxies and their spheres of influence, indicative of the projected intergalactic space in the filaments (compared to the projected circumgalactic space within 1.5 R$_{\rm vir}$). The Virgo Cluster clearly stands out as many galaxies overlap in their projected spheres at 1.5 R$_{\rm vir}$, while in most other filaments, there are both regions with strong overlap and regions without overlapping halos. In Sect. 6 and in the appendix, we will discuss other virial radii as selection criteria.

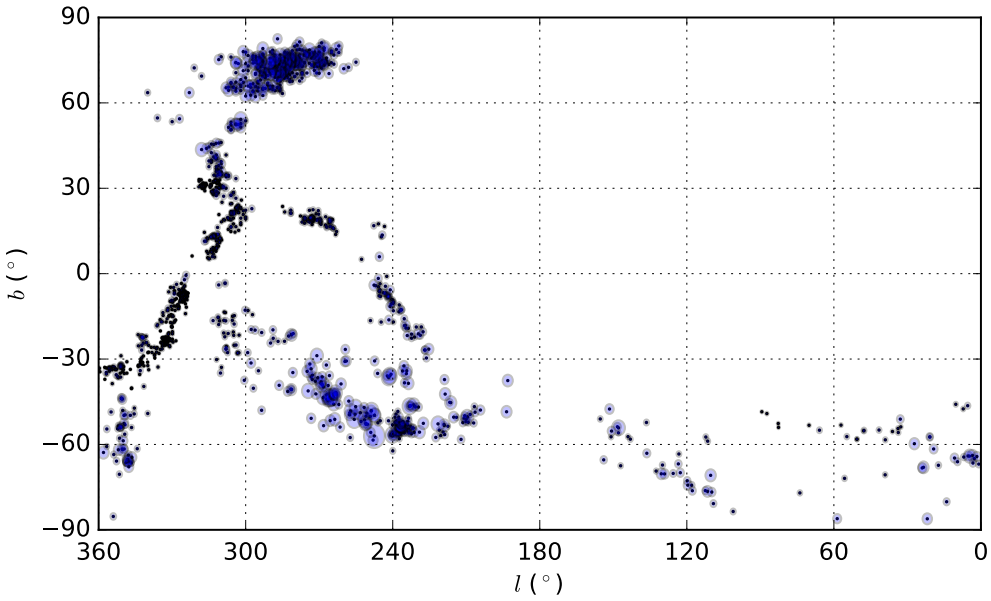

Figure 4.5 — Galaxies belonging to all filaments considered in this study plotted together with their projected 1.5 virial radii.

4.4.1 Parametrisation of filament geometry

To define an axis for each filament, a rectangular box was generated per filament containing the galaxies therein. The dark blue filament (see Fig. 4.2) was split into two individual boxes for geometrical reasons. Widths and lengths of the boxes vary for the different filaments as they scale with the filament's projected dimensions.

After defining the boxes that sample the individual filaments, they were each subdivided into segments with the full width of the box and a length corresponding to 20° on the sky. Each segment overlaps with the previous one with half the area (10° length). The average longitude and latitude of the galaxies within each segment was then determined and used as an anchor point to define the filament axis. All these anchor points were connected in each filament to form its axis.

In this way, the definition of the filament axis on the sky allowed us to calculate impact parameters of the COS sightlines to the filaments. In addition, we calculated velocity gradients in the filaments by taking the average velocity of all galaxies in each segment as the velocity anchor point.

The method of using overlapping segments to determine the filament axis is similar to the approach used by Wakker et al. (2015). A difference with their approach is that they first determined which galaxies were part of the filament by looking at the velocities. We did not do this as the filaments were already defined by Courtois et al. (2013). The uncertainty on the placement of the filament axes is no more than 1.5° on the sky, and less for most filaments.

The characteristics of each filament will be discussed separately in the following subsections. The orange or 'four-cluster' filament from Courtois et al. (2013) is not discussed here as there are no available COS sightlines nearby.

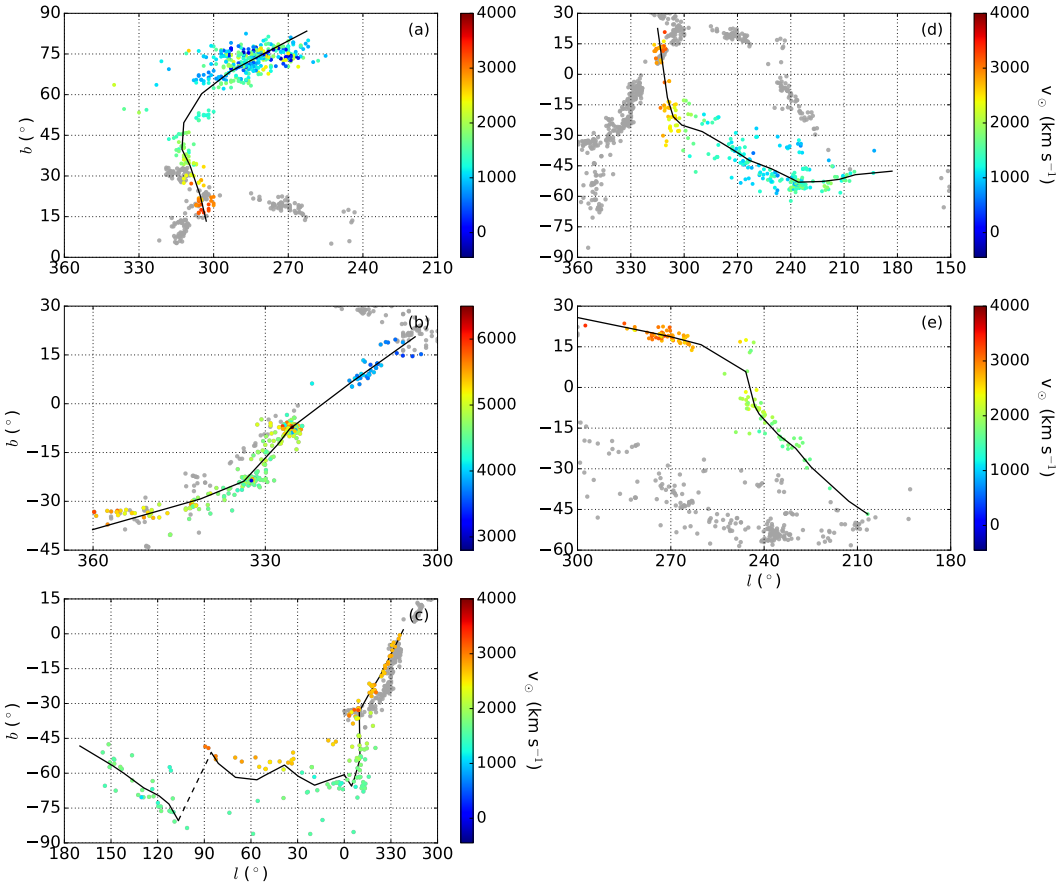

Figure 4.6 — Galaxies belonging to different filaments – (a): green; (b): purple; (c): dark blue; (d): cyan; (e): magenta – with their velocities colour-coded. Grey dots show galaxies belonging to one of the other filaments. The filament axes are indicated with the black solid lines.

4.4.2 Green filament

Perhaps the most notable of the filaments discussed here is the one containing the Virgo Cluster, located at a distance of ~16.5 Mpc (Mei et al. 2007) and home to as many as 2000 member galaxies. This filament is labelled in green in Fig. 4.2 and extends from the Centaurus Cluster to the Virgo Cluster in the range $l \sim 260 - 300°$ and $b \sim 60 - 70°$. The Virgo area has the highest galaxy density of the regions studied here.

The axis of the green filament as well as the galaxy velocities are indicated in Fig. 4.6a. The velocities range from $\sim 3400\ \mathrm{km\,s^{-1}}$ at the Centaurus Cluster to $\sim -400\ \mathrm{km\,s^{-1}}$. The velocities of the galaxies in the Virgo Cluster reach up to $\sim 2500\ \mathrm{km\,s^{-1}}$, indicating a large spread in velocities, just as would be expected for a massive galaxy cluster.

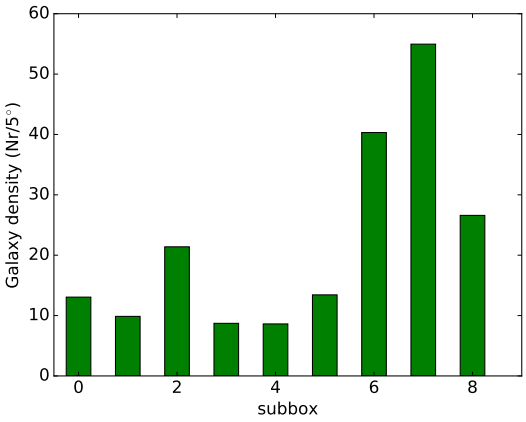

Figure 4.7 — Galaxy density along the green filament. The galaxy density indicates the number of galaxies within 5° on the sky for each galaxy.

Figure 4.7 shows that the density along the filament varies greatly, with the Virgo Cluster being the densest region (sub-boxes 6 to 8). In total, this filament has 427 galaxies and 36 COS sightlines passing through it.

4.4.3 Purple filament

As mentioned in Courtois et al. (2013), the purple filament is the longest cosmological structure in space among those studied here. In projection, however, it is one of the shorter filaments on the sky. This filament was discussed in detail by Fairall et al. (1998), who named it the 'Centaurus Wall'. The striking lack of galaxies in the regions around $b \sim 0°$ evident in Fig. 4.6b is due to the ZOA caused by the Milky Way disk in the foreground. Just below this scarcely populated region is the Norma Cluster ($l \sim 325°$), followed by the Pavus II Cluster ($l \sim 335°$).

The purple filament contains the galaxies with the highest velocities in our sample, with v reaching up to $6500\ \mathrm{km\,s^{-1}}$ (see Fig. 4.6b). These high velocities indicate distances of ≤ 85 Mpc. It is the only filament in which the galaxy velocities strongly increase when moving away from Centaurus. As such, it extends beyond the velocity range considered in Courtois et al. (2013). Here, we consider only the part of the filament indicated by their work.

The purple filament is the densest of our defined filaments, which is not surprising as it hosts two galaxy clusters and the projection effect makes it visually compact on the sky. A total of 351 galaxies from the V8k catalogue belong to this filament, though only two COS sightlines, which are both shared with the dark blue filament.

4.4.4 Dark blue filament

The dark blue filament represents one branch of the Southern Supercluster filament, defined in Courtois et al. (2013). Since it is clearly separated on the sky from the other branch (the cyan filament), these two branches are treated as individual filaments in this study. Starting from the Centaurus Cluster, the dark blue filament is entangled with the purple filament, but it continues to stretch out as a rather diffuse cosmological structure over the range $l \sim 0-180°$ in the southern hemisphere. Because of the low galaxy density, the filament axis of the dark blue filament is not well defined and is unsteady compared to other filaments, as can be seen in Fig. 4.6c. The dashed portion of the axis indicated in the figure is a result of the small number of galaxies found in this region; as such, the exact filament geometry in this part of the filament remains uncertain.

Figure 4.6 further indicates that average velocities in the dark blue filament are much lower than in the purple filament, making the two filaments easy to distinguish. The dark blue filament also exhibits two distinct velocity branches – one with velocities ~ 2500 km s^{-1} and one with v ~ 1300 km s^{-1} (see Fig. 4.6) – further underlining the inhomogeneous morphology of this filament. This filament has only 180 galaxies and 21 COS sightlines.

4.4.5 Cyan filament

The second branch of the Southern Supercluster filament is indicated by the cyan colour in Fig. 4.2. Compared to the dark blue filament, this branch is rather densely populated and the corresponding filament axis is well defined (Fig. 4.6d).

As with the green and dark blue filaments, the highest velocities in the cyan filament are found near the Centaurus Cluster, with velocities decreasing as one gets closer to the Fornax Cluster. However, Fig. 4.6 suggests that there is a slight increase in velocity near the end of the filament at $l < 240°$. The cyan filament is made up of 289 V8k galaxies, and there are 20 COS sightlines passing though it.

4.4.6 Magenta filament

This filament (magenta coloured in Fig. 4.2) contains the Antlia Cluster and also crosses the ZOA. While it is densely populated for $b > 0°$ (near Centaurus), it is under-dense near the ZOA and only moderately populated at negative Galactic latitudes. This makes the transition of the filament axis from positive to negative latitudes hard to define.

As can be seen in Fig. 4.6e, the velocities in this filament range from 3000 km s^{-1} near the Centaurus Cluster to 1400 km s^{-1} near its end at $l = 210°$ and $b = -45°$. It has 143 galaxies and two usable COS sightlines.

4.5 Lyα absorption and its connection to galaxies

To learn about the relation between intervening Lyα absorption, nearby galaxies, and the local large-scale structure in which the absorbers and galaxies are embedded, we first looked at the connection between Lyα absorption in the COS data and individual galaxies. In the upper panel of Fig. 4.8, we plot the equivalent widths of all Lyα absorbers against the line-of-sight impact parameter to the nearest galaxy, $\rho_{\rm gal}$, that has a radial velocity within 400 km s^{-1} of the absorber. For this plot, all V8k galaxies have been taken

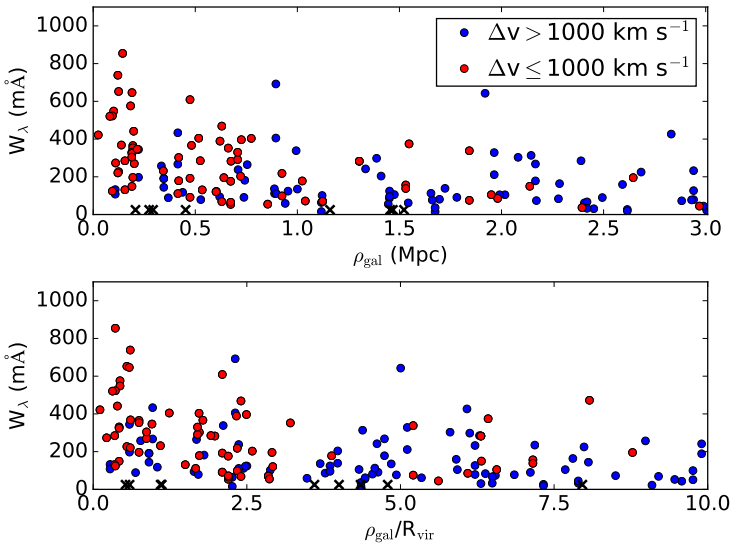

Figure 4.8 — Equivalent width of Lyα absorbers (blue dots) plotted against the impact parameter to the nearest galaxy (upper panel) or against the impact parameter in units of the galaxy's virial radius (lower panel). The sample has been split into components that lie within 1000 km s^{-1} of the nearest filament segment (red) and components that have a larger velocity difference (blue). Black crosses indicate sightlines that exhibit no significant Lyα absorption in the analysed spectral region. For these, we give the distance to the nearest galaxy in the velocity range $v = 1070-6700$ km s^{-1}.

into account (not just those in filaments) as some of the absorbers might be related to galaxies outside of the main cosmological structures. We indicate absorbers that are within 1000 km s^{-1} of the nearest filament in red and those that have larger deviation velocities in blue. Non-detections are indicated by the black crosses. The corresponding sightlines do not show any Lyα absorption in the wavelength range 1220−1243 Å.

There is an over-density of absorbers within 1 Mpc of the nearest galaxy, many of which have equivalent widths less than $W_\lambda < 200$ mÅ. This over-abundance of weak absorbers close to galaxies might be a selection effect. Prominent regions, such as the dense Virgo Cluster, receive more attention by researchers and are sampled by more sightlines (and by spectral data with better S/N) compared to under-dense cosmological regions, which typically are not as well mapped. The highest equivalent widths of the absorbers ($W_\lambda > 500$ mÅ) are typically found closer to the galaxies, in line with the often observed anti-correlation between the Lyα equivalent width and the impact parameter (e.g. Chen et al. 2001; French & Wakker 2017). There is, however, a large scatter in this distribution, which has also been seen in other studies (e.g. French & Wakker 2017). This scatter is most likely related to filament regions that have a large galaxy density and overlapping (projected) galaxy halos, as indicated in Fig. 4.5. Lyα absorption that is detected along a line of sight passing through such a crowded region cannot unambiguously be related to a particular galaxy (such as the nearest galaxy, which is assumed here) but could be associated, with the same likelihood, with any other (e.g. more distant) galaxy and its extended gaseous halo that is sampled by the sightline.

The lower panel of Fig. 4.8 shows the Lyα equivalent width plotted against ρ_{gal}/R_{vir}. Again, we see the same trend of stronger absorbers being closer to a galaxy. Out of the 208 Lyα absorption components, 29 are within 1.5 virial radii from the nearest

galaxy. Following Shull (2014) and Wakker et al. (2015), this is the characteristic radius up to which the gas surrounding a galaxy is immediately associated with that galaxy and its circumgalactic gas-circulation processes (infall, outflows, and mergers). It corresponds to $\sim 2-3$ times the gravitational radius as defined in Shull (2014). Outside of this characteristic radius, the gas is more likely associated with the superordinate cosmological environment (i.e. the group or cluster environment and the large-scale filament; but see also Sect. 6 and Fig. B.1). Wakker et al. (2015) use both this distance criterion and the criterion of absorption occurring within 400 km s^{-1} of the galaxy's velocity to associate each absorber with either the galaxy or the filament. This velocity range (which we also adopt here; see above) is justified in view of other dynamic processes that would cause a Doppler shift of the gas in relation to the galaxy's mean radial velocity, such as galaxy rotation, the velocity dispersion of gas structures within the virialised dark-matter of the host galaxy, and in- and outflows.

In Fig. 4.9, we show how the H I column density (log$N$(H I)) and the Doppler parameter (b-value) vary with $\rho_{\rm gal}$. Similarly to W_λ, the largest values for log$N$(H I) and b are found at smaller impact parameters, but (again) the scatter is large.

Wakker et al. (2015) also plotted the equivalent width versus impact parameter to the nearest galaxy for their sample. Although there are some high equivalent width absorbers at large $\rho_{\rm gal}$ (out to 2000 kpc), the average equivalent width decreases with increasing $\rho_{\rm gal}$. Similar to our sample, Wakker et al. (2015) find the majority of the absorbers within 1 Mpc of a galaxy. Our sample, however, has a larger scatter and a larger number of strong absorbers at larger distances. Prochaska et al. (2011) also conclude there is an anti-correlation between equivalent width and the galaxy impact parameter for their sample that has a maximum $\rho_{\rm gal}$ of 1 Mpc. In addition to stronger absorbers having lower impact parameters, their sample shows an increase in the number of weak absorbers ($W_\lambda < 100$ mÅ) with increasing impact parameter.

4.6 Lyα and its connection to filaments

In Fig. 4.10, the filaments are plotted together with the position of the COS sightlines (filled squares) and the velocities of the detected Lyα components, which are colour-coded (in the same way as the galaxies). Only those absorption components that have velocities within 1000 km s^{-1} of the nearest filament segment are considered. These plots are useful for visualising the large-scale kinematic trends of the absorption features along each filament while also allowing one to explore the spatial and kinematic connection between Lyα components and individual galaxies.

In the green filament (a), Lyα absorption is predominantly found near 1500 km s^{-1}. This holds true for both the sightlines at the outskirts of the filament and those going through the Virgo Cluster. For the latter, this indicates that the gas has a higher velocity than the typical velocity of galaxies in the Virgo Cluster (as mentioned earlier, the V8k catalogue takes into account the Virgo-flow model by Shaya et al. (1995)). Due to the extended Lyα trough in the Galactic foreground ISM absorption, intervening Lyα absorption below $\sim$ 1100 km s^{-1} cannot be measured in our COS dataset, meaning our absorption statistics are incomplete at the low end of the velocity distribution. Still, the trend of decreasing galaxy velocities with increasing distance to the Centaurus Cluster (see above) is not reflected in the kinematics of the detected Lyα absorbers in this filament, which appears to be independent of the large-scale galaxy kinematics.

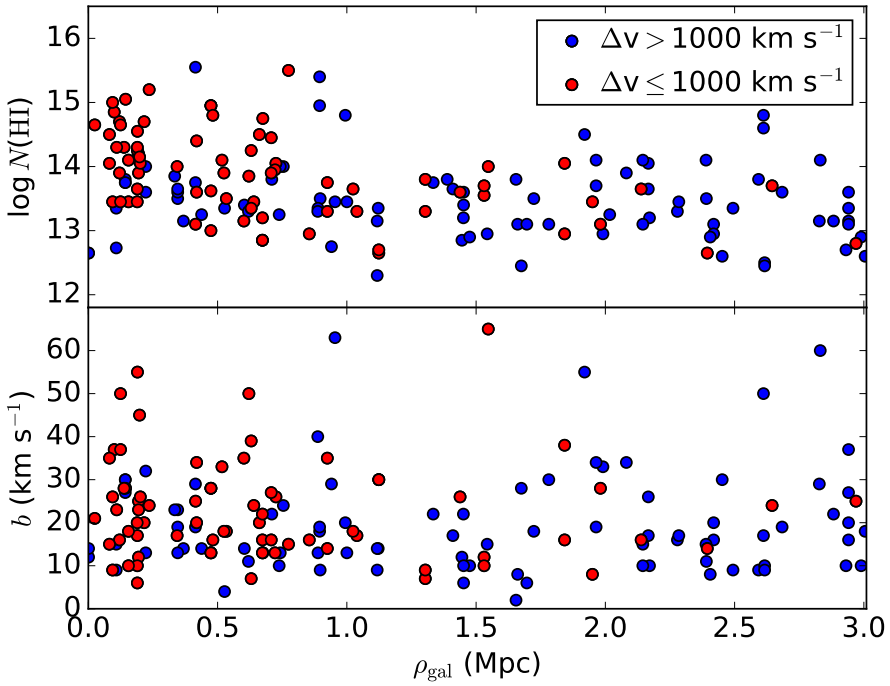

Figure 4.9 — Logarithmic H I column density and the Doppler parameter of Lyα absorbers plotted against $\rho_{\rm gal}$ for the same two samples that are shown in Fig. 4.8.

The purple filament (b) and the first section of the dark blue filament (c) overlap on the sky and have two COS sightlines in common. The different filament velocities allow us to assign the detected Lyα absorption in one of the sightlines to the purple filament, while the other sightline has one absorption component that we associate with the dark blue filament. With only two sightlines available for the purple filament, no clear trends can be identified.

As the dark blue filament continues, the different 'branches' noted earlier in Sect. 4.4 are also reflected in the velocities of the Lyα absorption components. This trend might be partly a result of our original selecting criterion for filament-related absorbers (absorption within 1000 km s^{-1} of the closest filament-segment velocity; see above). However, because of the large velocity range used, the selection criterion cannot account for the entire branching effect. Obviously, in this filament, the gas traces the velocities of the galaxies. Since this is the most diffuse filament, the chance of finding a Lyα absorber that is not directly associated with a galaxy but rather traces the large-scale flow of matter in that filament is higher.

The cyan filament (d) is well populated with galaxies while also being relatively long and broad. It thus has a high cross-section, and there are several sightlines that pass through this structure. Also in this case, the Lyα absorption appears to follow the velocity trend of the galaxies in the filament. Starting from Centaurus, the absorbers first exhibit velocities around 1800 km s^{-1}; the velocities then decrease by several hundred km s^{-1} to rise again slightly at the end of the filament, in line with the galaxies' velocity pattern.

Most of the sightlines that pass through the magenta filament (e) are not suited for spectral analysis. The one sightline we analysed shows no significant absorption in the

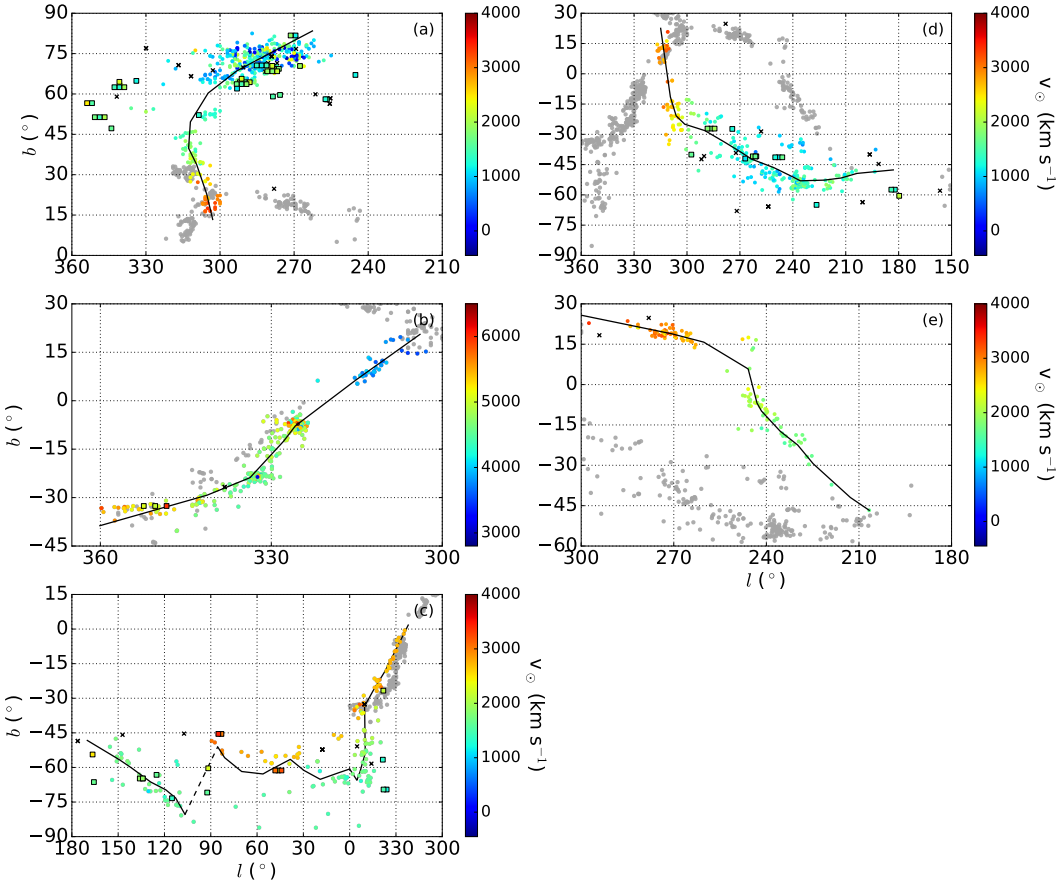

Figure 4.10 — Same as Fig. 4.6, but here with Lyα absorbers (coloured squares) that fall within 1000 km s^{-1} of the filament's velocity overlaid. Multiple absorbers along the same sightline have been given spatial offset. COS sightlines that do not exhibit Lyα absorption in this range are indicated by black crosses.

relevant velocity range, implying that no useful information is available for the magenta filament.

Analogous to Fig. 4.8, Fig. 4.11 shows the equivalent width of the Lyα absorbers, but now plotted against the filament impact parameter, $\rho_{\rm fil}$. To evaluate whether the absorbers are related to a nearby galaxy, those absorbers that pass within 1.5 $R_{\rm vir}$ and $\Delta v < 400$ km s^{-1} of a galaxy are shown as open circles, whereas absorbers not associated with a (known) galaxy are indicated with solid circles. In Fig. B.2 of the appendix, we show the effect of varying the impact-parameter criterion on absorbers being associated with a galaxy between 1.0 and 2.5 $R_{\rm vir}$ (which, however, led to no further insights).

While some of the absorbers with the highest equivalent widths are associated with a galaxy, this is not true for all strong absorbers. Neither sub-sample shows a clear, systematic trend for the equivalent width scaling with $\rho_{\rm fil}$, except that the maximum Lyα equivalent width in a given $\rho_{\rm fil}$ bin decreases with increasing distance. However, both sub-samples show a higher absorber density within $\rho_{\rm fil} < 3$ Mpc compared to more distant regions. Some of the absorbers indicated in green extend up to $\rho_{\rm fil} = 13$ Mpc, but these absorbers are unlikely to be part of the green filament as the typical width of a cosmological filament is a few megaparsecs (Bond et al. 2010). But even if we limit our

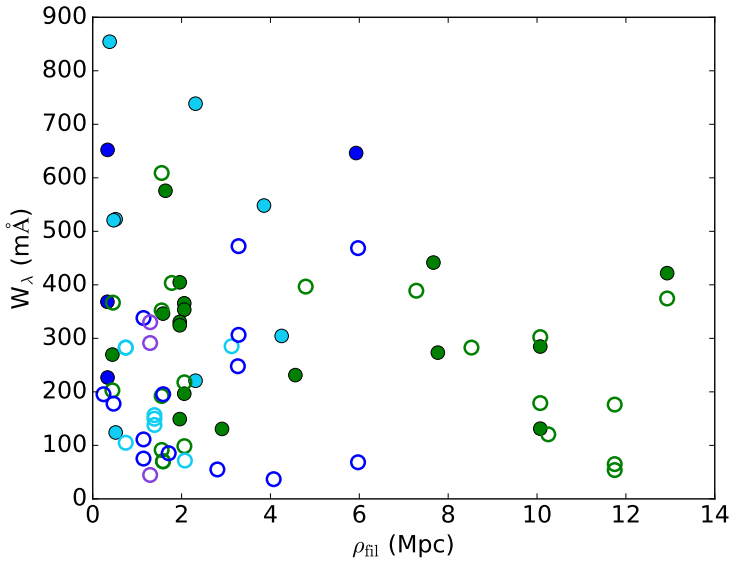

Figure 4.11 — Lyα equivalent width versus filament impact parameter for absorbers with velocities within 1000 km s^{-1} of the nearest filament segment. Open circles indicate absorbers that are associated with a galaxy (passing it within 1.5 $R_{\rm vir}$ and $\Delta v < 400$ km s^{-1}), and closed circles indicate absorbers that are not associated with a (known) galaxy. The different colours indicate the individual filaments.

analysis to absorbers with $\rho_{\rm fil} < 5$ Mpc (as in Wakker et al. 2015), the large scatter in the distribution of Lyα equivalent widths versus the filament impact parameter remains.

The velocity trends for galaxies and absorbers along four filaments (green, purple, dark blue, and cyan) are shown in Fig. 4.12. The starting point for each filament is the Centaurus Cluster region. Here, each sub-box (segment) is defined to have a length of 10° on the sky. This is half the length of the sub-boxes (segments) used to define the filament axes (see Sect. 4.1) because here, sub-boxes (segments) do not overlap. A length of 20° was only chosen for the second part of the dark blue filament (sub-boxes 12 to 18) in order to have a sufficient number of galaxies available for the determination of a meaningful average velocity.

Both the green and cyan filaments (Figs.4.12a and d) show a clear decrease in velocity as they extend farther away from the Centaurus Cluster. For these two filaments, the velocities of the detected Lyα absorbers all lie above the lower limit of the galaxy velocity dispersion in each sub-box, with only one exception (see sub-box 3 in the green filament, where one absorber falls just below the shaded area). This could possibly mean that there is a void of absorbers in the region between the filament and the Milky Way. However, it is important to recall that, because of the Galactic foreground absorption, absorbers with velocities less than ~1100 km s^{-1} could not be measured. This limit could also explain why there is no absorption in the lower velocity range of the Virgo Cluster (see sub-boxes 6 and 7 in Fig. 4.12a).

Furthermore, most absorbers in sub-boxes 2 to 4 and a couple in the other sub-boxes have large $\rho_{\rm fil}$ (> 5 Mpc). The velocity spread for those absorbers in the first sub-boxes is larger and trending towards slightly higher velocities than that of the galaxies. Most, however, fall within the standard deviation of the galaxy velocities.

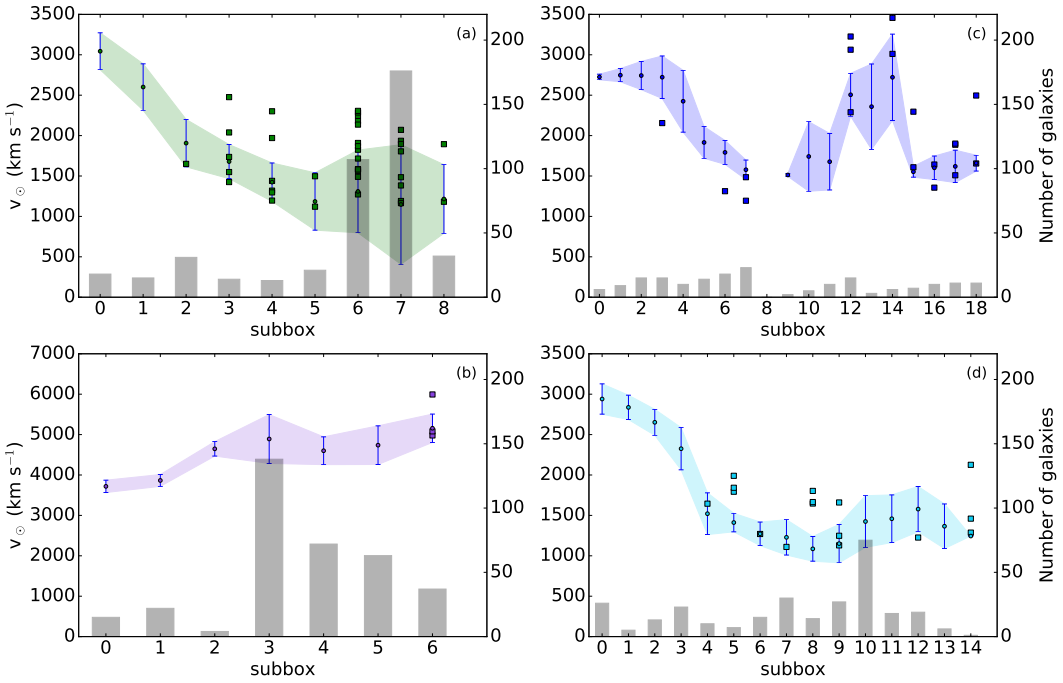

Figure 4.12 — Average galaxy velocities along four filaments (dots) – (a): green; (b): purple; (c): dark blue; (d): cyan – plotted together with the velocities of Lyα absorbers (squares) for each sub-box (segment). The velocity dispersion is indicated by the colour-shaded area. The grey bars indicate the numbers of galaxies belonging to each sub-box (segment) in the filament.

The purple filament contains only three absorbers, all belonging to the same sightline at the end of the filament, as can be seen in Fig. 4.12b. The plot underlines that this filament is well populated, with more than 50 galaxies in four out of seven sub-boxes.

Just like the filament axis in Fig. 4.6c, the velocity trend along the dark blue filament is irregular. This trend is also reflected in the absorber velocities. While there are only a few galaxies in each sub-box, the second part of the filament contains 14 absorbers, which is comparable to the total number of absorbers in the cyan filament.

4.7 Absorber statistics

In quasar-absorption spectroscopy, the observed relation between the number of H I absorption systems in the column density interval ΔN ($N_{\rm HI}$ to $N_{\rm HI} + dN$) and the absorption path length interval ΔX (X to $X + dX$) is commonly characterised by the differential CDDF, $f(N_{\rm HI})$. We used the formalism described in Lehner et al. (2007, and references therein) and adopted the following expression to describe the differential CDDF of our Lyα absorbers:

$$f(N_{\rm HI})\, dN_{\rm HI}\, dX = C_{\rm HI}\, N_{\rm HI}^{-\beta}\, dN_{\rm HI}\, dX. \tag{4.1}$$

Following, for example, Tytler (1987), absorption path ΔX and redshift path Δz at $z \approx 0$ can be approximated by the relation

$$\Delta X = 0.5[(1 + \Delta z)^2 - 1],$$

where we calculate the redshift path length Δz for the various sightline samples as described in Sect. 3.2. The slope of the CDDF is given by the exponent β, while the normalisation constant, $C_{\rm HI}$, can be calculated via the relation

$$C_{\rm HI} \equiv m_{tot}(1-\beta)/\{N_{max}^{1-\beta}[1-(N_{min}/N_{max})^{1-\beta}]\}.$$

Here, m_{tot} is the total number of absorbers in the column density interval N_{min} to N_{max}.

The column density distributions for our sample of Lyα absorbers are shown in Fig. 4.13. The CDDFs were fitted for Lyα components with log N(H I) $\geq$ 13.2 (maximum log N(H I) = 15.5). For the full filament sightline sample, we derive $\beta = 1.63 \pm 0.12$, while for the sub-sample of absorbers within 1000 km s^{-1} of the filament velocity we obtain $\beta = 1.47 \pm 0.24$. Using high-resolution Space Telescope Imaging Spectrograph (STIS) data, Lehner et al. (2007) derived $\beta = 1.76 \pm 0.06$ for their sample of narrow absorbers (b $\leq$ 40 km s^{-1}, 110 absorbers) and $\beta = 1.84 \pm 0.06$ for b $\leq$ 150 km s^{-1} (140 absorbers), thus slightly steeper slopes than the distributions found here. We note that we do not split our sample based on b-values as the fraction of absorbers with $b > 40$ km s^{-1} is small (≤ 5 %).

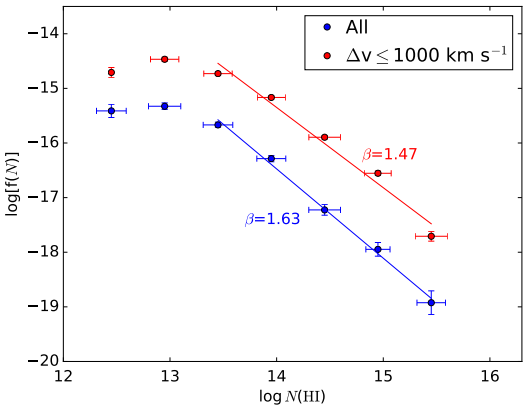

Figure 4.13 — H I CDDF for the Lyα absorbers in sightlines close to filaments (blue) and the absorbers falling within 1000 km s^{-1} of the filament velocity (red). Errors in log[f(N)] are from Poisson statistics.

A comparison with other recent studies can be made, for example with the Danforth et al. (2016) COS study of the low-redshift IGM, which yields $\beta = 1.65 \pm 0.02$ for a redshift-limited sub-sample of 2256 absorbers. Other results are: $\beta = 1.73 \pm 0.04$ from Danforth & Shull (2008, 650 absorbers from COS), $\beta = 1.65 \pm 0.07$ by Penton et al. (2000, 187 absorbers from the Goddard High Resolution Spectrograph, GHRS, and STIS), and $\beta = 1.68 \pm 0.03$ by Tilton et al. (2012, 746 absorbers from STIS). Most of these values are consistent with $\beta = 1.60 - 1.70$, whereas higher values ($\beta > 1.70$) may indicate a redshift evolution of the slope between $z = 0.0 - 0.4$. Such an evolution was discussed in Danforth et al. (2016), who find a steepening of the slope with decreasing z in this redshift range. For our study, with $z \leq 0.0223$, the slope should be close to the value valid for the universe at $z = 0$.

Furthermore, the spectral resolution may play a role in the determination of β. For instance, the spectral resolution of COS ($R \approx 20,000$) is substantially lower than the resolution of the STIS spectrograph ($R \approx 45,000$) used by Lehner et al. (2007); as such, some of our Lyα absorption components might be composed of several (unresolved) sub-components with lower column densities. The limited S/N in the COS data additionally hampers the detection of weak Lyα satellite components in the wings of stronger absorbers (see also Richter et al. 2006a, their Fig. 1).

In this series of results, the shallower CDDF ($\beta = 1.47 \pm 0.24$) for the sub-sample of velocity-selected absorbers within 1000 km s^{-1} of the filaments stands out. Although this low value is formally in agreement, within its error range, with the canonical value of

$\beta = 1.65$, it may hint at a larger relative fraction of high-column-density systems in the filaments, reflecting the spatial concentration of galaxies and the general matter over-density in these structures. A larger sample of Lyα absorbers associated with filaments would be required to further investigate this interesting aspect on a statistically secure basis.

Table 4.1 — Lyα line density for the full sample (filament- and non-filament-related sightlines), for filament-related sightlines, and for the velocity-selected absorber sample ($\Delta v < 1000$ km s^{-1}).

log$N$(H I)	$\mathcal{N}$	$d\mathcal{N}/dz$
Full sample		
	579	116 ± 5
Filament sample		
12.0 – 16.5	215	144 ± 11
13.2 – 14.0	132	88 ± 8
13.2 – 16.5	147	98 ± 8
Velocity-selected filament sample		
12.0 – 16.5	74	233 ± 27
13.2 – 14.0	46	145 ± 22
13.2 – 16.5	60	189 ± 25

In line with previous studies, our sample offers an opportunity to study the number of Lyα absorbers per unit redshift ($d\mathcal{N}/dz$). Table 4.1 gives the Lyα line density for the entire sample, as well as for several sub-samples. Those sub-samples separate the sample into different column density bins, allowing us to directly compare the results to the high-resolution Lehner et al. (2007) absorber sample and other studies.

For the full absorber sample (including filament- and non-filament-related sightlines), the Lyα line density is 116 ± 5 lines per unit redshift, but only for the filament-related sub-sample do we have column density information available (see Sect. 3.2). Taking this sub-sample in the ranges $13.2 \lesssim \log N(\mathrm{H\,I}) \lesssim 14.0$ and $13.2 \lesssim \log N(\mathrm{H\,I}) \lesssim 16.5$, we derive Ly$\alpha$ line densities of 88 ± 8 and 98 ± 8, respectively. These values are in good agreement with those reported by Lehner et al. (2007), who derived number densities of 80 ± 6 and 96 ± 7 for the same column density ranges.

Our results can also be compared with those obtained from the much larger COS absorber sample presented in Danforth et al. (2016). They derive a relation for $d\mathcal{N}/dz$ in the form $d\mathcal{N}(>N)/dz \approx 25\,(N/10^{14}\ \mathrm{cm}^{-2})^{-0.65}$. For absorbers with $\log N(\mathrm{H\,I}) \geq 13.2$, this leads to $d\mathcal{N}/dz \sim 83$, slightly lower than the values derived by us and Lehner et al. (2007), but still in fair agreement.

If we take the velocity-selected absorber sample, which potentially traces the Lyα gas associated with the filaments, we obtain a significantly higher line density of $d\mathcal{N}/dz = 189 \pm 25$. The redshift path length for the velocity-selected absorber sample was calculated for each sightline by considering a velocity range of ± 1000 km s^{-1} around the centre velocity for the filament segment that was closest to that sightline.

The value of 189 ± 25 for the velocity-selected filament sample is 93 percent higher than the value derived for the total filament-absorber sample (along the same lines of sight). This line over-density of the Lyα forest kinematically associated with filaments obviously reflects the matter over-density of baryons in the potential wells of these large-scale cosmological structures.

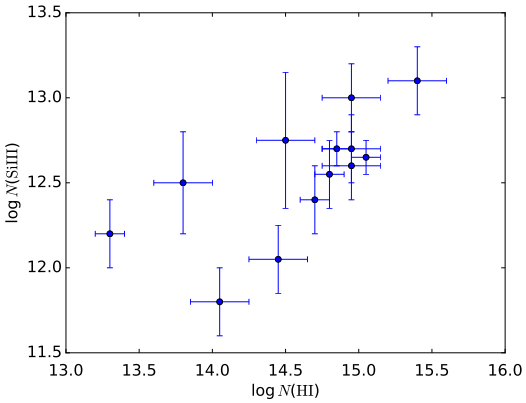

Figure 4.14 — Relation between log$N$(Si III) and log$N$(H I) for 13 systems in our absorber sample.

For the sake of completeness, we also show in Fig. 4.14 the relation between log$N$(Si III) and log$N$(H I) for absorbers in our sample for which both species are detected. Only for a small fraction (8.4 %) of the Lyα components can Si III be measured, which is partly because of the velocity-shifted Si III falling in the range of Galactic Lyα absorption. Generally, log$N$(Si III) increases with log$N$(H I), as expected from other Si III surveys in the IGM and CGM (e.g. Richter et al. 2016), but the scatter is substantial. The small number of Si III/H I absorbers in our sample does not allow us to draw any meaningful conclusions on the metal content of the absorbers in relation to their large-scale environment.

4.8 Discussion on Lyα absorbers and their environment

In their study, Prochaska et al. (2011) correlated galaxies and Lyα absorbers at $z = 0.06 - 0.57$ and found that for weak absorbers ($13 \leq \log N(\mathrm{H\,I}) \leq 14$), fewer than 20 % of the systems were associated with a known galaxy, while for strong absorbers ($\log N(\mathrm{H\,I}) \geq 15$), this fraction was 80 %. The criteria they used for associating a galaxy with an absorber were the following: i) a velocity difference between absorber and galaxy of ≤ 400 km s^{-1} and ii) an impact parameter of $\rho \leq 300$ kpc. Using the same criteria for our sample, we find that 10 % (40 %) of the low- (high-) column-density absorbers are associated with a galaxy in the V8k galaxy sample.

Therefore, and in agreement with Prochaska et al. (2011), we find that high-column-density Lyα absorbers are associated four times more often with a galaxy than are low-column-density absorbers; however, the overall percentage of absorbers for which an associated galaxy is found is only half of that in the Prochaska et al. (2011) sample. This can be attributed to the fact that the V8k catalogue is incomplete for $M_B < -16$ and $v > 1000$ km s^{-1}, while the Prochaska et al. (2011) galaxy sample is complete up to at least $z = 0.1$ for galaxies with $L < 0.1L_*$. By comparing their observed covering fractions with a filament model, Prochaska et al. (2011) conclude that all Lyα absorbers are associated with either a galaxy or a filament. This view is debated by Tejos et al. (2012), however, who argue that there is an additional population of 'random' Lyα absorbers that reside in the under-dense large-scale structure (voids).

The idea of Lyα absorbers belonging to different populations (and thus different environments) was proposed more than 25 years ago by Morris et al. (1993). By analysing Lyα absorbers in a single sightline and comparing the location of the absorbers with locations of galaxies, these authors found that the absorbers do not cluster around galaxies as strongly as galaxies cluster among themselves. On the other hand, they also found the trend that the absorbers do cluster around galaxies. From this, they concluded that there could be two populations of Lyα absorbers: one that is associated with galaxies and one that is more or less randomly distributed.

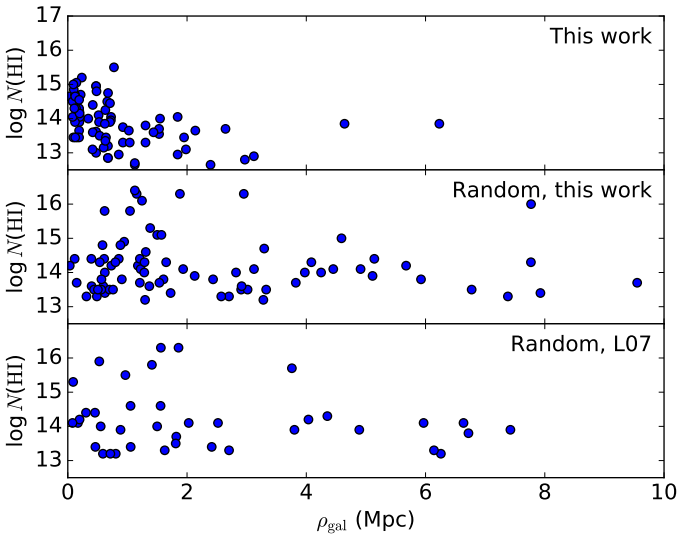

Figure 4.15 — H I column density versus $\rho_{\rm gal}$ for Lyα absorbers: as measured in the COS data (upper panel), for a randomised sample following the CDDF in this work (middle panel), and for a randomised sample following the number statistics and CDDF from Lehner et al. (2007, lower panel).

To test whether the Lyα absorbers in our sample resemble a 'random population', we generated two artificial populations of Lyα absorbers, both with random sky positions, random absorption velocities within the assumed $v_{\rm fil} \pm 1000$ km s^{-1} velocity range of a filament, and random H I column densities weighted by the H I CDDF. For the first population, we restricted the sample from Lehner et al. (2007, hereafter abbreviated with L07) to the redshift range spanned by the filaments in our study and used the slope of their CDDF (resulting in 39 absorbers, $\beta = 1.76$). For the other population, we used our own absorber sample and slope (74 absorbers, $\beta = 1.47$). The normalisation constant and absorber path length were calculated using the relations given above. All absorbers were assumed to be at a distance of ≤ 5 Mpc from the nearest galaxy belonging to a filament, which was also our original criterion to select absorbers inside a filament. The fraction of the simulated absorbers in each filament was adjusted to match the real fractions found in this study. Because the dark blue and purple filaments have an overlap on the sky, their randomised simulated counterparts were generated for both filaments combined.

Figure 4.15 shows a comparison of how column densities for the three different Lyα absorber samples (observed sample, random sample with own statistics, and random sample with L07 statistics) depend on $\rho_{\rm gal}$. As in Sect. 4.5, $\rho_{\rm gal}$ was calculated for the nearest galaxy on the sky within a velocity interval of 400 km s^{-1} from the absorber. Clearly, the measured absorbers cluster more strongly around galaxies than either random sample does. This indicates that at least some of the absorbers are associated with galaxies, as expected from previous studies (e.g. Morris & Jannuzi 2006; Prochaska et al. 2011; Tejos et al. 2014; French & Wakker 2017).

A very rough estimate of the fraction of absorbers associated with a galaxy can be made by comparing the fraction of absorbers within 1.5 Mpc of a galaxy in different samples. For the measured absorbers, 82 % have $\rho_{\rm gal} \leq 1.5$ Mpc, while the fraction for the randomised sample drawn from our own distribution is 53 % and for the L07 random sample it is 46 %. In conclusion, about a third of our absorbers cannot be explained by a random population and might be connected to a nearby galaxy.

When comparing the distance of the Lyα absorbers to the nearest filament axis, as shown in Fig. 4.16, a similar, albeit less pronounced, trend can be seen. Measured absorbers are generally found closer to the filament axis than a random distribution

shows. One may argue that this could be a selection effect, for example from targeting particularly interesting areas such as the Virgo Cluster, which would result in more sightlines near the Virgo filament. However, Fig. 4.11 shows the breakdown of absorbers into different filaments, demonstrating that the absorbers belonging to the Virgo Cluster filament (green) are in fact more spread out than absorbers in other regions, disproving such a selection effect.

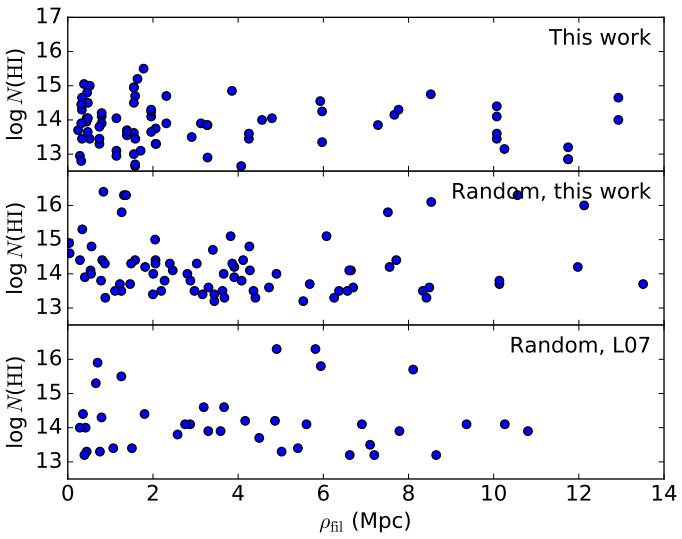

Figure 4.16 — Same as Fig. 4.15, but now for $\rho_{\rm fil}$.

To further investigate the possible clustering signal of Lyα absorbers near the filament axis, we plot, in Fig. 4.17, the cumulative distribution function for $\rho_{\rm fil}$ for the three previously mentioned absorber samples (observed sample, random sample with own statistics, and random sample with L07 statistics) as well as the galaxies that constitute the filament. We have also added another absorber test sample (D16) generated from the Lyα column density distribution of absorbers reported in Danforth et al. (2016). The cumulative distribution of galaxies sets the reference point as these define the filament. As can be seen, the observed distribution of absorbers clusters more strongly around the filament axis than do the three random absorber test distributions, but not as strongly as the galaxies. Within the inner 2 Mpc, in particular, the fraction of measured Lyα absorbers rises faster than the synthetic absorbers in the randomised samples.

The cumulative distribution function as shown in Fig. 4.17 can be compared with that for absorbers associated with galaxies. Figure 3 in Penton et al. (2002) shows this function for 46 Lyα absorbers and sub-samples thereof. Their full sample follows a distribution similar to that of our absorbers, with ~60 % found within 2 Mpc of the nearest galaxy (Penton et al. 2002) or filament (this study). Both studies show the galaxies more strongly clustered than the Lyα absorbers. Stocke et al. (2013) compared their absorber-galaxy cumulative distribution function with a random distribution and concluded that absorbers are associated with galaxies in a more general way, namely, they trace the large-scale structure instead of individual galaxies. Penton et al. (2002), Stocke et al. (2013), and Keeney et al. (2018) all conclude that high-column-density absorbers are more strongly correlated with galaxies than those with lower column densities. This is in agreement with what is found here: Lyα absorbers do not trace the same distribution as galaxies, but they are not randomly distributed around filaments either.

A Kolmogorov-Smirnov (KS) test confirms that the absorbers found in the COS data are not drawn from a random distribution. Table 4.2 lists the KS values and p-values for the different samples.

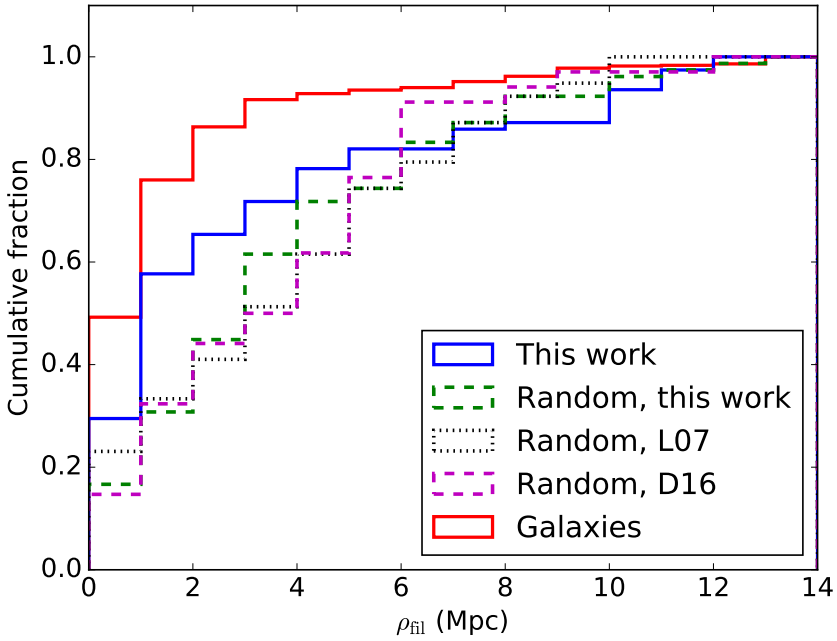

Figure 4.17 — Cumulative distribution function for $\rho_{\rm fil}$ for three different absorber samples. The measured absorbers in the COS data are indicated in blue, the random sample with its own statistics is plotted in dashed green, the random sample with the L07 statistics is indicated in dotted black, and the random sample from Danforth et al. (2016) is added in dashed magenta (D16). The distribution for the galaxies is shown in red.

A KS test can be used to compare two different samples to evaluate whether or not they are drawn from the same parent distribution. A high KS value (maximum of 1) indicates a high probability that this is true. The p-value instead indicates the significance that the null hypothesis is rejected. In this case, the null hypothesis is that $\rho_{\rm fil}$ for the absorbers measured in this study follows the same distribution as that of a random sample or of the galaxies in the filament. A p-value of < 0.05 means that the null hypothesis can be rejected with a probability of > 95 %. In all three comparisons between the measurements and the random absorber samples (our own sample, randomised, and the randomised L07 and D16 samples), the KS test indicates that they do not follow the same distribution.

The low p-value that we obtain from comparing the COS absorber sample with the V8k galaxy sample in the filaments further indicates that the Lyα absorbers are not drawn from the same distribution as the galaxies. To evaluate the hypothesis that there are two populations of Lyα absorbers (e.g. Morris et al. 1993; Tejos et al. 2012), we removed from

Table 4.2 — Kolmogorov-Smirnov test for impact-parameter distributions.

Sample compared	KS statistics	p-value
Random, this work	0.28	0.003
Random, L07	0.31	0.011
Random, D16	0.32	0.013
V8k galaxies	0.26	0.032

the sample (as a test) those absorbers that we had associated with galaxies. This had, however, no significant effect on the cumulative distribution function for $\rho_{\rm fil}$.

In conclusion, the cumulative distribution functions for $\rho_{\rm fil}$ show that galaxies are more strongly clustered in the filaments than are the Lyα absorbers that belong to the same cosmological structures. Lyα absorbers do not follow a random distribution, nor do they follow the same distribution as the galaxies that constitute large-scale filaments. There might be two (or more) separate populations of Lyα absorbers in filaments, but there is no evidence (from our study) that the Lyα absorbers that are not directly associated with large galaxies are randomly distributed in the field of the filament.

Deeper insights into these aspects (including other important cosmological issues such as over-density bias factors and how they affect the absorber-to-galaxy-to-filament statistics) are highly desirable. However, they will require a much larger observational dataset in combination with numerical cosmological simulations.

4.9 Summary and concluding remarks

In this study, we have combined galaxy data of more than 30,000 nearby galaxies from the V8k catalogue Courtois et al. (2013) with HST/COS UV spectral data of 302 distant AGN to investigate the relation between intervening H I Lyα absorbers and five nearby cosmological structures (galaxy filaments) at $z \approx 0$ ($v < 6700$ km s^{-1}).

(1) All in all, we identify 587 intervening Lyα absorbers along the 302 COS sightlines in the wavelength range between 1220 and 1243 Å. For the 91 sightlines that pass through the immediate environment of the examined galaxy filaments, we analysed 215 (227) Lyα absorption systems (components) in detail and derived column densities and b-values for H I (and associated metals, if available).

(2) For the individual galaxies in our sample, we have calculated the virial radii from their luminosities and the galaxy impact parameters, $\rho_{\rm gal}$, to the COS sightlines. We assume 29 Lyα absorbers to be directly associated with galaxies as they are located within 1.5 virial radii of their host galaxies and within 400 km s^{-1} of the galaxies' recession velocity.

(3) We characterise the geometry of the galaxy filament by considering the galaxy distribution in individual segments of the filaments. In this way, we define for each filament a geometrical axis that we use as reference for defining the filament impact parameters, $\rho_{\rm fil}$, for those Lyα absorbers that are located within 1000 km s^{-1} of the filament.

(4) We find that the absorption velocities of the Lyα absorbers reflect the large-scale velocity pattern of the four galaxy filaments, for which sufficient absorption line data are available. Seventy-four absorbers are aligned in position and velocity with the galaxy filaments, indicating that these absorbers and the galaxies trace the same large-scale structure .

(5) If we relate the measured Lyα equivalent widths (or H I column densities) with the galaxy and filament impact parameters, we find that the strongest absorbers (equivalent

widths $W_\lambda > 500$ mÅ) are preferentially located in the vicinity of individual galaxies (within 3 virial radii) and/or in the vicinity of the filament axes (within 5 Mpc). The observed relations between W and $\rho_{\rm gal}/\rho_{\rm fil}$ exhibit substantial scatter, however, disfavouring a simple equivalent width with impact parameter anti-correlation.

(6) We find that the measured H I components follow a CDDF with a slope of $-\beta = -1.63 \pm 0.12$, a value that is typical for the low-redshift Lyα forest. Only for the sub-sample of absorbers within 1000 km s^{-1} of the filament velocity do we obtain a shallower CDDF with $\beta = 1.47 \pm 0.24$, possibly indicating an excess of high-column-density absorbers in galaxy filaments when compared to the overall Lyα forest.

(7) The Lyα absorbers that lie within 1000 km s^{-1} of the nearest filament have a ~ 90 percent higher rate of incidence ($d\mathcal{N}/dz = 189 \pm 25$ for $\log N({\rm H\,I}) \geq 13.2$) than that of the general Lyα absorber population in our sample ($d\mathcal{N}/dz = 98 \pm 8$ for $\log N({\rm H\,I}) \geq 13.2$). This higher number density of Lyα absorbers per unit redshift most likely reflects the filaments' general matter over-density.

(8) We compare the filament impact-parameter distributions of the galaxies, measured Lyα absorbers, and a (synthetic) Lyα absorber sample with randomised locations on the sky with one another. We find that the galaxies are most strongly clustered around the filament axes, while the spatial clustering of the observed Lyα absorbers around the filament axes is evident but less pronounced. Using a KS test, we confirm that the Lyα absorbers neither follow the impact-parameter distribution of the galaxies nor a random distribution, but represent an individual, spatially confined sample of objects.

Taken together, the results of our study underline that the relation between intervening Lyα absorbers, large-scale cosmological filaments, and individual galaxies (that constitute the filaments) in the local universe is complex and manifold, and difficult to reconstruct with existing data.

This complexity is not surprising, of course, if we recall what Lyα absorbers actually are: They are objects that trace local gas over-densities in an extremely extended, diffuse medium that is gravitationally confined in hierarchically structured potential wells and stirred up by large-scale matter flows and galaxy feedback. In this picture, the spatial distribution of Lyα absorbers in cosmological filaments is governed by both the distribution of individual sinks in the large-scale gravitational potential energy distribution (i.e. galaxies, galaxy groups, etc.) and more (or less) stochastically distributed density fluctuations at larger scales that reflect the internal dynamics of the IGM.

For the future, we are planning to extend our study of the relation between intervening absorbers and cosmological filaments in the local universe. We will use a larger (and deeper) galaxy sample and additional HST/COS spectra, in combination with constrained magneto-hydrodynamic cosmological simulations of nearby cosmological structures.

5 Summary and Conclusions

With the majority of baryons in the Universe being in the IGM, this diffuse medium plays a key role in cosmological structure formation. It is thought to contain a large fraction of the baryons in the Universe in various phases (e.g. Shull et al. 2012; Nicastro et al. 2005, 2018). Despite its importance, however, there remain many unanswered questions regarding the exact relation between the IGM and the large-scale structure traced by galaxies. By analysing absorption systems found in QSO sightlines and combining these data with that of galaxies, this thesis' aim was to improve our understanding of the nearby CGM and the IGM and the connection to their environment.

In order to better understand these aspects, this thesis started with several questions (Sect. 1.6). Here, we will summarise the two studies that compose this thesis and revisit the questions posed before. The results will be discussed in the context of other studies, both theoretical and observational, and a brief outlook will be given at the end.

5.1 The Local Group

The first study (Chapter 3) focused on the LG gas environment by analysing *HST*/COS archival data from 29 QSOs. Of these QSOs, 19 were in the LG's barycentre direction and the remaining 10 in the anti-barycentre direction. We used synthetic spectra to measure Si II, Si III, Si IV, C II and C IV absorption between $-400 \leq v_{\rm LSR} \leq -100$ km s^{-1} for the barycentre sample and between $+100 \leq v_{\rm LSR} \leq +400$ km s^{-1} for the anti-barycentre sample. This gave a total of 69 absorbing systems.

For each absorption system, we combined the measured abundances with a Cloudy model to obtain local gas densities, $\log n_{\rm H}$. For the anti-barycentre sample, we found $-2.6 \leq \log n_{\rm H} \leq -3.15$, while the barycentre sample spanned a slightly larger range of densities: $-2.5 \leq \log n_{\rm H} \leq -4.0$. Based on the pressure-distance relation described in the pressure model of the Galactic halo from Miller & Bregman (2015), the absorbers with $\log n_{\rm H} \leq -3.54$ are likely located at distances $r > 200$ kpc. This places those absorbers outside of the virial radius of the Milky Way, thereby possibly making them part of the LG's intra-group medium.

This leads us to the first sub-question posed in Sect. 1.6:

What is the origin of HVCs around the Milky Way?

As discussed in Chapter 3, 27 HVCs found in the barycentre direction of the LG have an origin within the Galactic halo, at distances $\lesssim 200$ kpc, but 14 other absorption systems may reside outside of the halo, in the intra-group medium towards M31. The clouds at larger distances have low $\log n_{\rm H}$ and relatively high velocities and are located mainly in the region of Complex GCN. To provide further evidence for two distinct populations, we applied the Lee statistic on the absorber sample, which confirmed that there is a low density population and one with higher densities. The separation value given by this statistic is $\log n_{\rm H} = -3.44$, which is similar to the value suggested from the pressure-distance relation ($\log n_{\rm H} = -3.54$). In conclusion, the large variation in abundances and distances hint at various origins for the HVCs in this region, though what exactly those origins are remains a matter of debate.

Diaz & Bekki (2011) show that Complex GCN might be connected to the Leading Arm of the Magellanic System and the origin of this stripped gas would be the Small Magellanic Cloud. The low metallicity of some of these clouds is in agreement with this theory (For et al. 2016), as is the lack of a pronounced core-envelope structure in many of the clouds belonging to Complex CGM (Winkel et al. 2011).

However, Winkel et al. (2011) found that the HVCs of Complex GCN likely have various origins and are a transient phenomenon, as they are not stable in the turbulent surrounding medium. This would fit with them being the result of ongoing accretion of warm gas from a source outside of the MW halo (see also Bland-Hawthorn 2009). In addition to this, Qu et al. (2020a) find in their simulations of warm gas (traced by Si IV) that, while most clouds found in observations can be explained by feedback processes from the disc, there are several high-velocity features that cannot be the result of these processes. One of these is a population of absorbers in the direction of the LG barycentre. Further observations in X-ray hint at a bridge of hot gas between the MW and M31 (Qu et al. 2020b).

Our location inside of the MW makes it difficult to obtain an overview of the gas distribution. Constrained simulations of the LG can help provide us with an outside perspective. As a part of the CLUES project, Nuza et al. (2014) modelled gas densities within the LG. A comparison between those densities and the ones obtained in our study is shown in Fig. 5.1. The red squares give the densities and distances found here, with those below the dashed blue line assumed to be outside of the MW's virial radius and with $\log n_{\rm H} \leq -3.54$. Distances of the HVCs above this line are upper limits, they may be located closer to the MW than indicated here. The densities of the population thought to be located outside of the MW's virial radius are higher than the average value expected from simulations (dashed black line) and also higher than the expected gas density in the direction of M31. The difference with the simulation's densities in the direction of M31 is about a factor five in most places, decreasing at larger distances. This difference makes sense when considering that the densest clumps of gas form the HVCs that have been observed here, while the results from Nuza et al. (2014) give the *average* gas densities in low-resolution simulations. Within those simulations, small-scale clumps like HVCs will not be resolved. High-resolution simulations are desired to model structure on these scales. Despite this, Fig. 5.1 does show that there is a pressure platform between MW and M31, which results in higher hydrogen densities in this region than expected for other directions. HVCs in this direction having an even higher density is in agreement with them tracing the densest regions of gas.

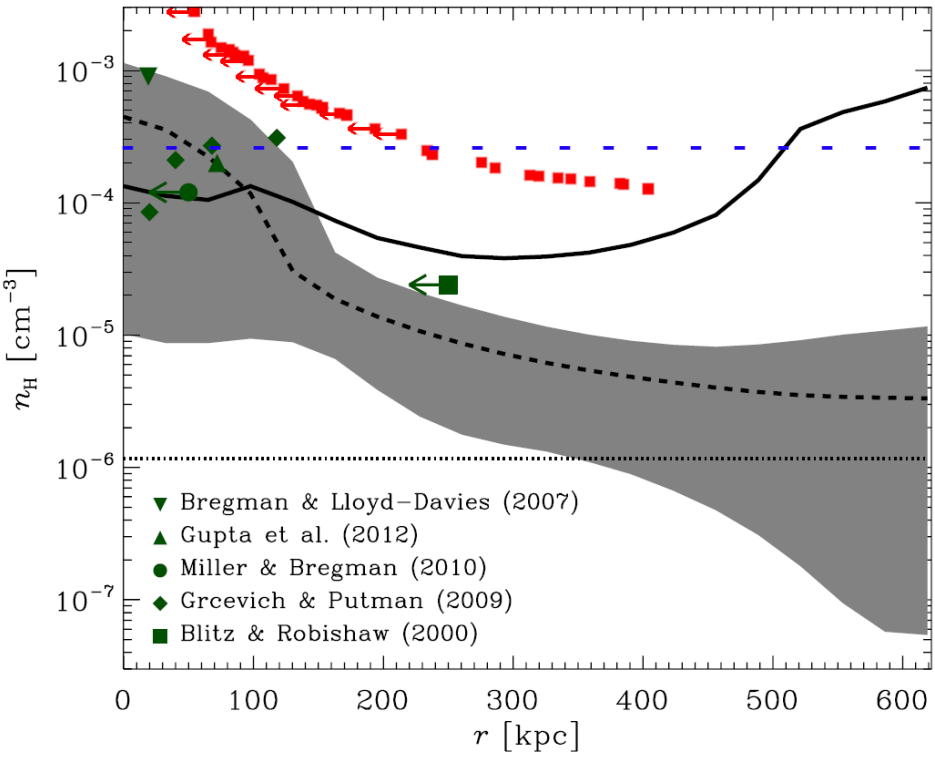

Figure 5.1 — Hydrogen number density as function of distance from the MW for as found in the simulations by Nuza et al. (2014, their Fig. 16) overplotted with the approximate values found in this study for the HVCs in the barycentre direction (red squares). The blue dashed line is the division between HVCs within the MW's virial radius (above, distances are all upper limits) and outside of it (below). The black dashed line gives the mean hydrogen number density from the simulations, with the standard deviation indicated by the shaded area. The solid black line gives the density in the direction of M31. Electron number densities found in various studies have been included by green symbols.

In conclusion, our study underlines that HVCs do not have a single origin. Interactions between gas from various sources make it difficult to disentangle the various sources of the gas. Our results indicate that some of the HVCs may trace gas outside of the MW halo that is associated with the intra-group medium of the LG.

To obtain more precise distance estimates of HVCs, spectroscopic observations of distant globular clusters can be used together with QSO sightlines passing near those clusters. The bracketing method can then be used to determine whether some HVCs are indeed outside of the MW's virial radius. Spectra of globular clusters are needed because these objects can probe larger distances than bright halo stars, but to obtain those spectra, more sensitive UV instruments are required than currently available.

5.2 Gas and filaments in the local Universe

After studying gas at scales of the MW and the LG, we looked at gas at larger scales, namely that of cosmological filaments in the local Universe, which have typical lengths of $50-80$ Mpc h^{-1} and widths of ~ 10 Mpc h^{-1} (Sheth et al. 2003; Bharadwaj et al. 2004; Wakker et al. 2015). In order to find a possible connection between the gas and the large-scale structure traced by galaxies, we used a combination of 302 QSO spectra from the *HST*/COS data archive and the V8k catalogue of galaxies. Using the V8k data, Courtois et al. (2013) defined several filaments in the local Universe. After selecting the galaxies assigned to a filament by Courtois et al. (2013), we determined axes for the 6 filaments, together with the velocity gradient along those axes. Out of the 302 COS spectra, 79 were close enough to a filament to possibly trace the gas residing in that filament and within those 79 spectra, we identified a total of 215 Lyα absorption systems in the wavelength range $1220-1243$ Å. We measured the equivalent width for those systems and also construed synthetic spectra in order to obtain column densities. A subsample was made of absorbers whose velocity was within 1000 km s^{-1} of the mean velocity of the nearest filament segment. These 74 absorbers are close enough in velocity to the filament to be tracing the gas belonging to the filament.

The CDDF, which gives information about the number of absorbers in a certain column density interval per absorption-path length interval, for the full sample of Lyα absorbers has a slope of $\beta = 1.63 \pm 0.12$, which is in accordance with other studies (e.g. Penton et al. 2000; Lehner et al. 2007; Danforth et al. 2016). The subsample with $\Delta v \leq 1000$ km s^{-1} has a slightly shallower slope: $\beta = 1.47 \pm 0.24$. This shallower slope indicates there are relatively more absorbers with higher densities than in the full sample, which could be the result of a matter overdensity in the filaments.

The results from this second study can be used to address the two remaining sub-questions from Sect. 1.6:

Do Lyα absorbers trace individual galaxies or the large-scale structure they reside in?

In Chapter 4, we plotted the EW against galaxy and filament impact parameter to find possible correlations between absorber strength and impact parameter. We found some of the strongest absorbers are either close to galaxies or to the filament axis, but there is no clear anti-correlation between equivalent width and either impact parameter. Thus, the connection between gas and galaxies is not as straight-forward as a one-on-one relation.

Similar to the results in Chapter 4, Wakker et al. (2015) analysed Lyα absorbers in relation to filaments and individual galaxies and found that stronger absorbers trace the CGM of individual galaxies, whereas weaker ones follow the large-scale structure (see also Bowen et al. 2002; Wakker & Savage 2009; Stocke et al. 2013; Prochaska et al. 2011; Tejos et al. 2014). By looking at the clustering between absorbers and galaxies and galaxies with galaxies, Penton et al. (2002) found that the nearest galaxy distance distribution for stronger absorbers ($W_\lambda > 68$ mÅ) is more similar to that of galaxies, while weaker absorbers show a weaker clustering relation. Danforth et al. (2016) also found that clustering between strong Lyα absorbers ($\log N > 13.5$) is as strong as or stronger than the clustering between galaxies, whereas the clustering between weaker absorbers is less strong.

The conclusion that weaker absorbers trace the large-scale IGM, while stronger absorbers trace more dense structures–in which galaxies are located–is also shown in the model from Davé et al. (1999). They do not find a clear distinction between absorbers related to galaxies and those in the IGM, however. This is in line with the results shown in Chapter 4 as well as various other studies that show a gradual decline and large scatter in the relation between equivalent width and galaxy impact parameter (Chen et al. 2001; Bowen et al. 2002; Wakker & Savage 2009; French & Wakker 2017).

By using sightlines close to each other on the sky, Lee et al. (2018) made a 3D map of the Lyα forest at $2.0 \lesssim z \lesssim 2.5$ and compared this with a map of galaxies. The over- and underdensities of their gas distribution seem to visually agree with the structures traced by galaxies. An analysis of the IllustrisTNG simulations by Martizzi et al. (2019) shows that in filaments and knots, the majority of the baryons is in the WHIM, while the less dense voids and sheets are dominated by cooler gas at T$\leq 10^5$ K. This can be seen in Fig 5.2. Since only a small fraction of hydrogen remains neutral in the WHIM, it is difficult to trace in Lyα absorption and other tracers have to be used, such as O VI.

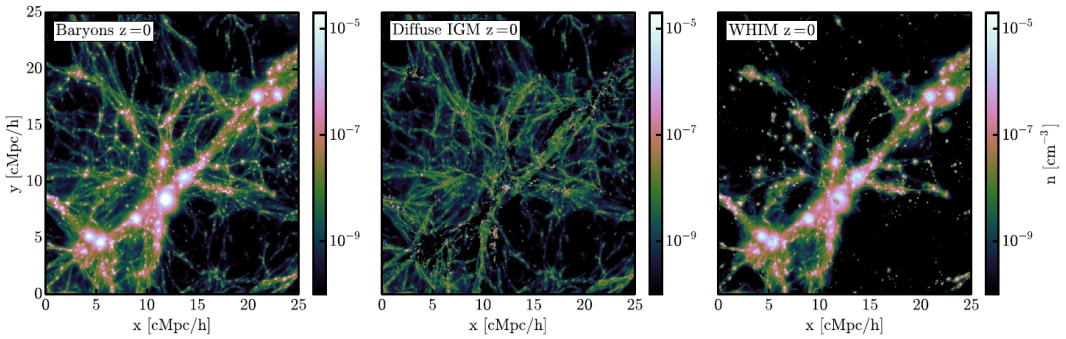

Figure 5.2 — Baryons in the Cosmic Web at $z = 0$ in the IllustrisTNG simulations. Left panel shows all baryons, middle panel shows baryons in the diffuse IGM and right panel shows baryons in the WHIM (Fig. 8, Martizzi et al. 2019).

In addition to predicting the state of the gas in the local Universe, simulations can aid observations by showing how the gas distribution evolved over time. Martizzi et al. (2019) follow the evolution of baryons in gas from $z = 8$ to $z = 0$ in the IllustrisTNG simulations. Baryons are divided into different groups like star-forming gas, WHIM and diffuse IGM based on density and temperature. This way, the fraction of baryons in these different phases can be traced over time. Similarly, cosmological structures like knots, filaments and sheets are defined in the simulations in order to follow their evolution. This makes it possible to trace the flow of matter from one component to others and the results can be used to predict what observations of different regions are expected to show, if the assumptions used in the simulations used are correct. Fumagalli et al. (2011b) also studied the flow of matter in simulations, finding cold streams which might be detected as LLS in observations. They find that the fraction of neutral gas increases at higher redshift ($z > 3$), resulting in DLAs that are not directly associated with galaxies.

To understand the relation between Lyα absorbers, galaxies and the underlying dark matter distribution, simulations on different scales are needed. Whereas the studies mentioned above focus on large volumes of the Cosmic Web, Wakker et al. (2015) compared their observations of gas along a single filamentary structure with the distribution of matter along a simulated filament. They then applied various background

radiation fields and plot the resulting column density along the minor axis of the filaments, concluding the densities are strongly dependent on the radiation field. While observations will always be limited by the number of sightlines, simulations are not restricted in this way and can thus give a more complete view of where baryons reside. Furthermore, simulations can show the dark matter distribution together with that of the gas. Villaescusa-Navarro et al. (2018) showed that most H I gas resides in dark matter halos. At $z > 2$, they find this fraction decreases and the IGM becomes more dense.

Another method of studying the matter distribution of the Universe is to use the two- and three-point correlation functions, which can be calculated for Lyα absorbers as well as for galaxies. Two-point correlation functions have been used by e.g. Penton et al. (2002); Tejos et al. (2014); Danforth et al. (2016) to compare clustering of absorbers with that of galaxies as well as with cluttering found in random samples. In addition to this correlation function, the three-point correlation function can be used to study non-Gaussian variations in the density field. This is a relatively new field and most studies so far have been done by measuring the three-point correlation function in simulations (Tie et al. 2019; Maitra et al. 2020a), but Maitra et al. (2020b) used the absorber sample of Danforth et al. (2016) to measure the correlation function in observations. Both simulations and large observational surveys can be used to advance this field.

A new approach by Burchett et al. (2020) uses a method inspired by the *Physarum polycephalum* slime mold to find structures in the Cosmic Web. The original method aims to find the optimal transport network between discrete objects and, by adding probabilistic sampling and selection, Burchett et al. (2020) obtain a probabilistic density distribution of filaments. They applied this method to galaxy surveys and H I absorption line data and found that most baryons in the IGM are in the Cosmic Web.

Despite the many absorption line studies done over the years, the question in which way Lyα absorbers trace the large-scale structure of the Universe does not have a straightforward answer. It appears there are different populations of absorbers, some of which are associated with galaxies, while others trace cosmological filaments.

A possible successor to *HST*/COS will be the World Space Observatory Ultraviolet (WSO-UV), which is scheduled to launch in 2025 (Shustov et al. 2020). It will be equipped with two echelle spectrographs, one in the near UV and one in the far UV, and a long slit spectrograph. Among its main topics will be the study of the WHIM and of Lyα absorbers (Shustov et al. 2018). Data from the WSO-UV will hopefully expand our current knowledge.

With the advance in instrumentation, future work on the IGM will be able to focus more on detection of the IGM in emission, in addition to absorption. A recent paper by Reiprich et al. (2021) showed X-ray emission from a filament extending out from a galaxy cluster system, observed by the *eROSITA* instrument. Observing large-scale structure in X-ray emission is also one of the aims of the upcoming ESA mission *Athena* (e.g. Nandra et al. 2013). Another project aiming to study the IGM in emission is BlueMUSE, a medium resolution spectrograph which will operate at wavelengths 350–580 nm and is to be installed on the ESO Very Large Telescope (VLT) (Richard et al. 2019). One of the science goals of BlueMUSE is to study Lyα emission from the Cosmic Web at $z \sim 2-3$.

Is there a population of Lyα absorbers following a random distribution, as found in various studies?

Tejos et al. (2012) find that, in addition to Lyα absorbers tracing galaxies and those following the large-scale structure, there is a population that is associated with neither, instead following a random distribution. This result is further supported by Tejos et al. (2014), who compare correlation functions between Lyα absorbers and galaxies, galaxies and galaxies, and Lyα absorbers with themselves. Danforth et al. (2016) find a similar result in their survey and conclude that absorbers with $\log N(\mathrm{H\,I}) < 13.5$ are distributed in a more random fashion.

In this study, we looked at the impact parameter to the nearest filament, ρ_{fil}, for our sample of Lyα absorbers, the galaxies that constitute the filaments and several random populations. One random population of absorbers was generated for the column density distribution function found by Lehner et al. (2015) and one for the column density distribution function found by Danforth et al. (2016). The results of a KS-test for ρ_{fil} of the different samples point out that our measured Lyα absorbers are not drawn from the same parent population as the galaxies, with galaxies generally existing closer to the filament axis than absorbers. The absorbers, however, do not follow a random distribution either, instead falling in between the distribution of galaxies and a random one.

5.3 Tying it together

Now that we have tackled the sub-questions, we can focus on our main question, which was: **How does the wider gas environment connect to the cosmological structure in which galaxies reside?**

We studied gas on the relatively small scale of the LG, as well as in large-scale filaments in order to get a more complete view of how these different scales fit together. Our result that Lyα absorbers are not drawn from the same distribution as the galaxies that constitute filaments, but are not distributed randomly either suggests that at least part of the Lyα absorbers is tied to the large-scale structure in the local Universe. Similarly to the different populations of Lyα absorbers, some of the HVCs around the MW appear to exist outside of the virial radius of the MW and may be a part of the larger gas structure of the LG. These HVCs would be observed as intervening metal-line absorbers/H I LLSs if seen from an outside vantage point (Richter 2012; Herenz et al. 2013).

This complex relation between absorbers and their larger environment is expected, as the diffuse medium of the IGM is influenced both by stochastical gas density fluctuations in the large-scale filaments and the more local gravitationally confined structures such as galaxies and galaxy groups.

Simulations on different scales can help our understanding of how galaxies influence their surroundings and vice versa. The RomulusC simulation of Tremmel et al. (2019) is a high-resolution hydrodynamic simulation of a galaxy cluster. Tremmel et al. (2019) show that the cooling times of the ICM do not seem to be affected by the AGN feedback. However, a major merger event leads to an increase in the cooling timescale. This, in turn, could influence the star formation rates in the member galaxies.

Looking at the large-scale structure, the Illustris TNG simulation shows the majority of baryons is indeed located in the IGM at $z = 0$ (Martizzi et al. 2019). More specifically, the WHIM, which is located mostly in filaments and sheets, is predicted to contribute

most of the baryons. Martizzi et al. (2019) predict that O VII and Ne IX absorption could be detected by X-ray absorption instruments. The first is primarily located in filaments, whereas the latter is distributed equally over filaments and knots.

The simulations of Cui et al. (2018) predict that the gas filaments can be used to infer the underlying dark matter filaments almost unbiased. Their simulations imply that the velocity fields in gas and dark matter filaments are almost identical, and the densities of gas filaments are linearly proportional to the density fields of dark matter filaments. This means that H I emission from filaments can indeed be used to trace the dark matter distribution. This 21 cm emission may be detected with future radio telescopes (Kooistra et al. 2017).

5.4 Outlook

While much work has gone into mapping the gas around and in between galaxies, its exact distribution and connection to the large-scale structure of the Universe are not yet fully understood. From an observational point of view, more QSO sightlines are needed so that a larger part of the sky can be probed and compared with more complete galaxy surveys. New, more sensitive instruments like *Athena*, BlueMUSE, and WSO-UV will help advance the field. In addition to absorption spectroscopy, the IGM might be detected in emission as well.

Together with these advances in observational studies, simulations can play an important role. By studying simulations that model structure formation in the Universe, like the Illustris and the Millennium simulation, the flow of matter can be mapped out. This helps understand how the CGM and IGM are connected to galaxies. Furthermore, the the gas flows in magneto-hydrodynamic cosmological simulations of structures in the nearby Universe can give a better view on how the environment influences the gas.

Just like this study went from the relatively small scale of the LG to the larger-scale structure in the local Universe, simulations will also need to cover a range of scales. Gas on the scale of HVCs and substructures in the IGM require a high resolution, while simulations of large volumes are needed to study the connection of IGM and the large-scale structure defined by dark matter. In conclusion, many open questions remain, leaving us with many areas to study.

Acknowledgements

This thesis would not have come about without the support of many people and first among those is Philipp. Thank you for giving me the opportunity to work on this projects and for your support and enthusiasm throughout. Our meetings always helped to get me excited to continue with my research and see what the results would be. Also many thanks to Andrea for all your help and always being there to answer questions regarding paperwork and regulations. I don't know how I would have managed without your help.

Many thanks to the people of the research group Extragalactic Astrophysics as well, for your help with papers, this thesis and for the discussions during group meetings. Special thanks to Martin Wendt, Martin Sparre and Gábor for your helpful feedback on the thesis and to Kirill for translating the summary into German. Many, many thanks to Helge for helping with computer issues, including two PCs dying shortly after each other. And to all the others at the University, thank you, too, especially for all the delicious cake through the years and the Christmas dinners!

Outside of University, I would like to thank Anke, for the dinners we had together (I miss the poffertjes) and for being my friend for all these years! You're a great person and I'm really glad we met back in Groningen. Thank you Frederike, you're the best sister and I love you. To Heit, for starting my interest in astronomy by introducing me to Star Trek. To Mem, because you're always there and for all your support. I also want to thank the friends I've made here and those back in the Netherlands, I hope we'll be able to see each other more again soon! Thank you, lovely people from the Writers' Workshop and in the DA and TWC communities, you have brightened my day countless times with your stories.

Finally, thank you, Leah. For knowing when I needed to talk, for all your "Leah-uitspraken", for making me smile and for always being there. For everything.

Bibliography

Anderson, M. E., Bregman, J. N., & Dai, X. 2013, ApJ, 762, 106

Bahcall, J. N., Bergeron, J., Boksenberg, A., et al. 1996, ApJ, 457, 19

Baugh, C. M., Cole, S., Frenk, C. S., & Lacey, C. G. 1998, ApJ, 498, 504

Bharadwaj, S., Bhavsar, S. P., & Sheth, J. V. 2004, ApJ, 606, 25

Binggeli, B., Popescu, C. C., & Tammann, G. A. 1993, AApS, 98, 275

Binggeli, B., Tammann, G. A., & Sandage, A. 1987, AJ, 94, 251

Binney, J. 2004, MNRAS, 347, 1093

Birnboim, Y. & Dekel, A. 2003, MNRAS, 345, 349

Bland-Hawthorn, J. 2009, in The Galaxy Disk in Cosmological Context, ed. J. Andersen, Nordströara, B. m, & J. Bland-Hawthorn, Vol. 254, 241–254

Blitz, L., Spergel, D. N., Teuben, P. J., Hartmann, D., & Burton, W. B. 1999, ApJ, 514, 818

Böhringer, H., Briel, U. G., Schwarz, R. A., et al. 1994, Nature, 368, 828

Bond, N. A., Strauss, M. A., & Cen, R. 2010, MNRAS, 409, 156

Bondi, H. 1952, Cosmology.

Borisova, E., Cantalupo, S., Lilly, S. J., et al. 2016, ApJ, 831, 39

Bowen, D. V., Pettini, M., & Blades, J. C. 2002, ApJ, 580, 169

Bower, R. G., Benson, A. J., Malbon, R., et al. 2006, MNRAS, 370, 645

Boylan-Kolchin, M., Springel, V., White, S. D. M., Jenkins, A., & Lemson, G. 2009, MNRAS, 398, 1150

Brüns, C., Kerp, J., Kalberla, P. M. W., & Mebold, U. 2000, A&A, 357, 120

Burchett, J. N., Elek, O., Tejos, N., et al. 2020, ApJ, 891, L35

Cantalupo, S., Arrigoni-Battaia, F., Prochaska, J. X., Hennawi, J. F., & Madau, P. 2014, Nature, 506, 63

Carroll, B. & Ostlie, D. 2007, An Introduction to Modern Astrophysics (Pearson Addison-Wesley)

Catling, D. C. & Kasting, J. F. 2017, Energy and Radiation in Planetary Atmospheres (Cambridge University Press), 27–72

Cen, R. & Ostriker, J. P. 1999, ApJ, 514, 1

Chen, H.-W., Johnson, S. D., Zahedy, F. S., Rauch, M., & Mulchaey, J. S. 2017, ApJ, 842, L19

Chen, H.-W., Lanzetta, K. M., & Webb, J. K. 2001, ApJ, 556, 158

Chon, G., Böhringer, H., & Zaroubi, S. 2015, A&A, 575, L14

Chung, A., van Gorkom, J. H., Kenney, J. D. P., Crowl, H., & Vollmer, B. 2009, AJ, 138, 1741

Colless, M., Dalton, G., Maddox, S., et al. 2001, MNRAS, 328, 1039

Collins, J. A., Shull, J. M., & Giroux, M. L. 2004, ApJ, 605, 216

Collins, J. A., Shull, J. M., & Giroux, M. L. 2005, ApJ, 623, 196

Collins, J. A., Shull, J. M., & Giroux, M. L. 2007, ApJ, 657, 271

Cooper, T. J., Simcoe, R. A., Cooksey, K. L., O'Meara, J. M., & Torrey, P. 2015, ApJ, 812, 58

Courtois, H. M., Pomarède, D., Tully, R. B., Hoffman, Y., & Courtois, D. 2013, AJ, 146, 69

Cram, T. R. & Giovanelli, R. 1976, A&A, 48, 39

Cui, W., Knebe, A., Yepes, G., et al. 2018, MNRAS, 473, 68

Danforth, C. W., Keeney, B. A., Tilton, E. M., et al. 2016, ApJ, 817, 111

Danforth, C. W. & Shull, J. M. 2008, ApJ, 679, 194

Danforth, C. W., Stocke, J. T., & Shull, J. M. 2010, ApJ, 710, 613

Dashtamirova, D., Fischer, W. J., et al. 2018, Cosmic Origins Spectrograph Instrument Handbook, Version 12.0 (Baltimore: STScI)

Dashtamirova, D., Fischer, W. J., et al. 2020, Cosmic Origins Spectrograph Instrument Handbook, Version 12.1 (Baltimore: STScI)

Davé, R., Cen, R., Ostriker, J. P., et al. 2001, ApJ, 552, 473

Davé, R., Hernquist, L., Katz, N., & Weinberg, D. H. 1999, ApJ, 511, 521

Davies, J. J., Crain, R. A., McCarthy, I. G., et al. 2019, MNRAS, 485, 3783

Davis, T. M., Hinton, S. R., Howlett, C., & Calcino, J. 2019, MNRAS, 490, 2948

Dawson, K. 2020, No need to Mind the Gap: Astrophysicists fill in 11 billion years of our universe's expansion history, https://www.sdss.org/press-releases/no-need-to-mind-the-gap/, accessed: 2021-03-05

de Graaff, A., Cai, Y.-C., Heymans, C., & Peacock, J. A. 2019, A&A, 624, A48

de Vaucouleurs, G. 1953, AJ, 58, 30

de Vaucouleurs, G. 1956, Vistas in Astronomy, 2, 1584

Dekel, A. & Birnboim, Y. 2006, MNRAS, 368, 2

Di Teodoro, E. M. & Fraternali, F. 2014, A&A, 567, A68

Diaz, J. & Bekki, K. 2011, MNRAS, 413, 2015

Draine, B. T. 2011, Physics of the Interstellar and Intergalactic Medium

Dressler, A., Faber, S. M., Burstein, D., et al. 1987, ApJ, 313, L37

Drinkwater, M. J., Gregg, M. D., & Colless, M. 2001, ApJ, 548, L139

Eggen, O. J., Lynden-Bell, D., & Sandage, A. R. 1962, ApJ, 136, 748

Emerick, A., Bryan, G., & Putman, M. E. 2015, MNRAS, 453, 4051

Erb, D. K. 2008, ApJ, 674, 151

Fairall, A. P., Woudt, P. A., & Kraan-Korteweg, R. C. 1998, AApS, 127, 463

Ferland, G. J., Chatzikos, M., Guzmán, F., et al. 2017, Revista Mexicana de Astronomia y Astrofisica, 53, 385

Ferland, G. J., Porter, R. L., van Hoof, P. A. M., et al. 2013, Revista Mexicana de Astronomia y Astrofisica, 49, 137

Fischer, W. J. et al. 2018, Cosmic Origins Spectrograph Instrument Handbook, Version 10.0 (Baltimore: STScI)

Fitchett, M. & Merritt, D. 1988, ApJ, 335, 18

Fontana, A. & Ballester, P. 1995, The Messenger, 80, 37

For, B. Q., Staveley-Smith, L., McClure-Griffiths, N. M., Westmeier, T., & Bekki, K. 2016, MNRAS, 461, 892

Fox, A. J., Richter, P., Wakker, B. P., et al. 2013, ApJ, 772, 110

Fox, A. J., Savage, B. D., & Wakker, B. P. 2006, ApJS, 165, 229

Fox, A. J., Wakker, B. P., Barger, K. A., et al. 2014, ApJ, 787, 147

Fox, A. J., Wakker, B. P., Savage, B. D., et al. 2005, ApJ, 630, 332

Fox, A. J., Wakker, B. P., Smoker, J. V., et al. 2010, ApJ, 718, 1046

Fraternali, F. 2017, Astrophysics and Space Science Library, Vol. 430, Gas Accretion via Condensation and Fountains, ed. A. Fox & R. Davé, 323

Fraternali, F. & Binney, J. J. 2008, MNRAS, 386, 935

French, D. M. & Wakker, B. P. 2017, ApJ, 837, 138

Fukugita, M., Hogan, C. J., & Peebles, P. J. E. 1998, ApJ, 503, 518

Fumagalli, M., O'Meara, J. M., & Prochaska, J. X. 2011a, Science, 334, 1245

Fumagalli, M., Prochaska, J. X., Kasen, D., et al. 2011b, MNRAS, 418, 1796

Furlanetto, S. R., Schaye, J., Springel, V., & Hernquist, L. 2004, ApJ, 606, 221

Gamow, G. 1953, AJ, 58, 39

Genzel, R., Tacconi, L. J., Gracia-Carpio, J., et al. 2010, MNRAS, 407, 2091

Gibson, B. K., Giroux, M. L., Penton, S. V., et al. 2000, AJ, 120, 1830

Giovanelli, R., Verschuur, G. L., & Cram, T. R. 1973, AApS, 12, 209

Glidden, A., Cooper, T. J., Cooksey, K. L., Simcoe, R. A., & O'Meara, J. M. 2016, ApJ, 833, 270

Grcevich, J. & Putman, M. E. 2009, ApJ, 696, 385
Green, J. C., Froning, C. S., Osterman, S., et al. 2012, ApJ, 744, 60
Grevesse, N., Asplund, M., Sauval, A. J., & Scott, P. 2010, Ap&SS, 328, 179
Gunn, J. E. & Peterson, B. A. 1965, ApJ, 142, 1633
Haardt, F. & Madau, P. 1996, ApJ, 461, 20
Haardt, F. & Madau, P. 2001, in Clusters of Galaxies and the High Redshift Universe Observed in X-rays, ed. D. M. Neumann & J. T. V. Tran, 64
Haardt, F. & Madau, P. 2012, ApJ, 746, 125
Haider, M., Steinhauser, D., Vogelsberger, M., et al. 2016, MNRAS, 457, 3024
Haud, U. 1992, MNRAS, 257, 707
Hennawi, J. F., Prochaska, J. X., Cantalupo, S., & Arrigoni-Battaia, F. 2015, Science, 348, 779
Herenz, P., Richter, P., Charlton, J. C., & Masiero, J. R. 2013, A&A, 550, A87
Hopp, U., Schulte-Ladbeck, R. E., & Kerp, J. 2003, MNRAS, 339, 33
Hubble, E. 1929, Proceedings of the National Academy of Science, 15, 168
Jin, S. 2010, MNRAS, 408, L85
Joung, M. R., Bryan, G. L., & Putman, M. E. 2012, ApJ, 745, 148
Kalberla, P. M. W., Burton, W. B., Hartmann, D., et al. 2005, A&A, 440, 775
Kalberla, P. M. W., Dedes, L., Kerp, J., & Haud, U. 2007, A&A, 469, 511
Kalberla, P. M. W. & Haud, U. 2006, A&A, 455, 481
Karachentsev, I. D. & Nasonova, O. G. 2010, MNRAS, 405, 1075
Kauffmann, G., White, S. D. M., & Guiderdoni, B. 1993, MNRAS, 264, 201
Keeney, B. A., Stocke, J. T., Pratt, C. T., et al. 2018, ApJS, 237, 11
Kelly, R. 2005, No need to Mind the Gap: Astrophysicists fill in 11 billion years of our universe's expansion history, astronomy.com/magazine/2005/02/dominating-the-local-group, accessed: 2021-01-07
Kereš, D. & Hernquist, L. 2009, ApJ, 700, L1
Kereš, D., Katz, N., Weinberg, D. H., & Davé, R. 2005, MNRAS, 363, 2
Kollmeier, J. A., Weinberg, D. H., Oppenheimer, B. D., et al. 2014, ApJ, 789, L32
Kooistra, R., Silva, M. B., & Zaroubi, S. 2017, MNRAS, 468, 857
Kovács, O. E., Bogdán, Á., Smith, R. K., Kraft, R. P., & Forman, W. R. 2019, ApJ, 872, 83
Lau, E. T., Kravtsov, A. V., & Nagai, D. 2009, ApJ, 705, 1129
Lee, K.-G., Krolewski, A., White, M., et al. 2018, ApJS, 237, 31
Lee, K. L. 1979, Journal of the American Statistical Association, 74, 708
Lehner, N., Howk, J. C., Tripp, T. M., et al. 2013, ApJ, 770, 138
Lehner, N., Howk, J. C., & Wakker, B. P. 2015, ApJ, 804, 79
Lehner, N., Savage, B. D., Richter, P., et al. 2007, ApJ, 658, 680
Lofthouse, E. K., Fumagalli, M., Fossati, M., et al. 2020, MNRAS, 491, 2057
Lynds, R. 1971, ApJ, 164, L73
Mackenzie, R., Pezzulli, G., Cantalupo, S., et al. 2020, MNRAS
Madau, P., Ferrara, A., & Rees, M. J. 2001, ApJ, 555, 92
Maitra, S., Srianand, R., Gaikwad, P., et al. 2020a, MNRAS, 498, 6100
Maitra, S., Srianand, R., Gaikwad, P., & Khandai, N. 2020b, arXiv e-prints, arXiv:2012.05926
Marasco, A., Fraternali, F., & Binney, J. J. 2012, MNRAS, 419, 1107
Martizzi, D., Vogelsberger, M., Artale, M. C., et al. 2019, MNRAS, 486, 3766
Mathews, W. G. & Brighenti, F. 2003, ARA&A, 41, 191
Mei, S., Blakeslee, J. P., Côté, P., et al. 2007, ApJ, 655, 144
Miller, M. J. & Bregman, J. N. 2015, ApJ, 800, 14
Morris, S. L. & Jannuzi, B. T. 2006, MNRAS, 367, 1261
Morris, S. L., Weymann, R. J., Dressler, A., et al. 1993, ApJ, 419, 524

Morton, D. C. 2003, ApJS, 149, 205
Muller, C. A., Oort, J. H., & Raimond, E. 1963, Academie des Sciences Paris Comptes Rendus, 257, 1661
Münch, G. & Zirin, H. 1961, ApJ, 133, 11
Nandra, K., Barret, D., Barcons, X., et al. 2013, arXiv e-prints, arXiv:1306.2307
Nelson, D., Vogelsberger, M., Genel, S., et al. 2013, MNRAS, 429, 3353
Nicastro, F., Kaastra, J., Krongold, Y., et al. 2018, Nature, 558, 406
Nicastro, F., Mathur, S., Elvis, M., et al. 2005, Nature, 433, 495
Nicastro, F., Zezas, A., Elvis, M., et al. 2003, Nature, 421, 719
Nuza, S. E., Parisi, F., Scannapieco, C., et al. 2014, MNRAS, 441, 2593
Oort, J. H. 1966, Bulletin Astronomical Institute of the Netherlands, 18, 421
Osterbrock, D. E. & Ferland, G. J. 2006, Astrophysics of gaseous nebulae and active galactic nuclei
Pallottini, A., Gallerani, S., & Ferrara, A. 2014, MNRAS, 444, L105
Peebles, P. J. E. 1965, ApJ, 142, 1317
Peebles, P. J. E. 1967, ApJ, 147, 859
Peek, J. 2018, QuaStar: The first unobscured view of the Milky Way's Circumgalactic Medium, HST Cycle 26 Abstract Catalog
Penton, S. V., Shull, J. M., & Stocke, J. T. 2000, ApJ, 544, 150
Penton, S. V., Stocke, J. T., & Shull, J. M. 2002, ApJ, 565, 720
Penzias, A. A. & Wilson, R. W. 1965, ApJ, 142, 419
Péroux, C., McMahon, R. G., Storrie-Lombardi, L. J., & Irwin, M. J. 2003, MNRAS, 346, 1103
Persic, M. & Salucci, P. 1992, MNRAS, 258, 14P
Press, W. H. & Schechter, P. 1974, ApJ, 187, 425
Prochaska, J. X., Weiner, B., Chen, H. W., Mulchaey, J., & Cooksey, K. 2011, ApJ, 740, 91
Prochaska, J. X. & Wolfe, A. M. 2009, ApJ, 696, 1543
Putman, M. E. 2017, Astrophysics and Space Science Library, Vol. 430, An Introduction to Gas Accretion onto Galaxies, ed. A. Fox & R. Davé, 1
Putman, M. E., Gibson, B. K., Staveley-Smith, L., et al. 1998, Nature, 394, 752
Qu, Z., Bregman, J. N., Hodges-Kluck, E., Li, J.-T., & Lindley, R. 2020a, ApJ, 894, 142
Qu, Z., Huang, R., Bregman, J. N., & Li, J.-T. 2020b, arXiv e-prints, arXiv:2011.02125
Reiprich, T. H., Veronica, A., Pacaud, F., et al. 2021, A&A, 647, A2
Richard, J., Bacon, R., Blaizot, J., et al. 2019, arXiv e-prints, arXiv:1906.01657
Richter, P. 2012, ApJ, 750, 165
Richter, P. 2017, Gas Accretion onto the Milky Way, ed. A. Fox & R. Davé, Vol. 430, 15
Richter, P., Charlton, J. C., Fangano, A. P. M., Bekhti, N. B., & Masiero, J. R. 2009, ApJ, 695, 1631
Richter, P., de Boer, K. S., Werner, K., & Rauch, T. 2015, A&A, 584, L6
Richter, P., Fang, T., & Bryan, G. L. 2006a, A&A, 451, 767
Richter, P., Fox, A. J., Wakker, B. P., et al. 2013, ApJ, 772, 111
Richter, P., Krause, F., Fechner, C., Charlton, J. C., & Murphy, M. T. 2011, A&A, 528, A12
Richter, P., Nuza, S. E., Fox, A. J., et al. 2017, A&A, 607, A48
Richter, P., Paerels, F. B. S., & Kaastra, J. S. 2008, Space Science Reviews, 134, 25
Richter, P., Savage, B. D., Sembach, K. R., & Tripp, T. M. 2006b, A&A, 445, 827
Richter, P., Savage, B. D., Tripp, T. M., & Sembach, K. R. 2004, ApJS, 153, 165
Richter, P., Sembach, K. R., Wakker, B. P., et al. 2001, ApJ, 559, 318
Richter, P., Wakker, B. P., Fechner, C., et al. 2016, A&A, 590, A68
Sancisi, R., Fraternali, F., Oosterloo, T., & van der Hulst, T. 2008, A&ARv, 15, 189
Saunders, W., d'Mellow, K. J., Tully, R. B., et al. 2000a, in Astronomical Society of the Pacific Conference Series, Vol. 218, Mapping the Hidden Universe: The Universe behind the Mily Way - The Universe in HI, ed. R. C. Kraan-Korteweg, P. A. Henning, & H. Andernach, 153

Saunders, W., Sutherland, W. J., Maddox, S. J., et al. 2000b, MNRAS, 317, 55
Schmidt, M. 1963, Nature, 197, 1040
Sciama, D. W. 1955, MNRAS, 115, 3
Sembach, K. R., Savage, B. D., Lu, L., & Murphy, E. M. 1999, ApJ, 515, 108
Sembach, K. R., Wakker, B. P., Savage, B. D., et al. 2003, ApJS, 146, 165
Sembach, K. R., Wakker, B. P., Tripp, T. M., et al. 2004, ApJS, 150, 387
Shapiro, P. R. & Field, G. B. 1976, ApJ, 205, 762
Shaya, E. J., Peebles, P. J. E., & Tully, R. B. 1995, ApJ, 454, 15
Sheth, J. V., Sahni, V., Shandarin, S. F., & Sathyaprakash, B. S. 2003, MNRAS, 343, 22
Shull, J. M. 2003, in Astrophysics and Space Science Library, Vol. 281, The IGM/Galaxy Connection. The Distribution of Baryons at z=0, ed. J. L. Rosenberg & M. E. Putman, 1
Shull, J. M. 2014, ApJ, 784, 142
Shull, J. M., Moloney, J., Danforth, C. W., & Tilton, E. M. 2015, ApJ, 811, 3
Shull, J. M., Smith, B. D., & Danforth, C. W. 2012, ApJ, 759, 23
Shull, J. M., Stevans, M., Danforth, C., et al. 2011, ApJ, 739, 105
Shustov, B., Gómez de Castro, A. I., Sachkov, M., et al. 2018, Ap&SS, 363, 62
Shustov, B. M., Sachkov, M. E., Sichevsky, S. G., et al. 2020, INASAN Science Reports, 5, 306
Silk, J. 1968, ApJ, 151, 459
Simon, J. D. & Blitz, L. 2002, ApJ, 574, 726
Spitzer, Lyman, J. 1956, ApJ, 124, 20
Steinmetz, M. & Navarro, J. F. 2002, New Astronomy, 7, 155
Stetson, P. B. & Pancino, E. 2008, PASP, 120, 1332
Stewart, K. R., Kaufmann, T., Bullock, J. S., et al. 2011, ApJ, 738, 39
Stocke, J. T., Keeney, B. A., Danforth, C. W., et al. 2013, ApJ, 763, 148
Tanimura, H., Hinshaw, G., McCarthy, I. G., et al. 2019, MNRAS, 483, 223
Tejos, N., Morris, S. L., Crighton, N. H. M., et al. 2012, MNRAS, 425, 245
Tejos, N., Morris, S. L., Finn, C. W., et al. 2014, MNRAS, 437, 2017
Tejos, N., Prochaska, J. X., Crighton, N. H. M., et al. 2016, MNRAS, 455, 2662
Thom, C., Peek, J. E. G., Putman, M. E., et al. 2008, ApJ, 684, 364
Thom, C., Putman, M. E., Gibson, B. K., et al. 2006, ApJ, 638, L97
Tie, S. S., Weinberg, D. H., Martini, P., et al. 2019, MNRAS, 487, 5346
Tilton, E. M., Danforth, C. W., Shull, J. M., & Ross, T. L. 2012, ApJ, 759, 112
Tremmel, M., Quinn, T. R., Ricarte, A., et al. 2019, MNRAS, 483, 3336
Tully, R. B., Courtois, H., Hoffman, Y., & Pomarède, D. 2014, Nature, 513, 71
Tully, R. B., Rizzi, L., Shaya, E. J., et al. 2009, AJ, 138, 323
Tumlinson, J., Peeples, M. S., & Werk, J. K. 2017, ARA&A, 55, 389
Tumlinson, J., Shull, J. M., Rachford, B. L., et al. 2002, ApJ, 566, 857
Tumlinson, J., Thom, C., Werk, J. K., et al. 2013, ApJ, 777, 59
Tytler, D. 1987, ApJ, 321, 49
Villaescusa-Navarro, F., Genel, S., Castorina, E., et al. 2018, ApJ, 866, 135
Wakker, B. P. 2001, ApJS, 136, 463
Wakker, B. P., Hernandez, A. K., French, D. M., et al. 2015, ApJ, 814, 40
Wakker, B. P., Howk, J. C., Savage, B. D., et al. 1999, Nature, 402, 388
Wakker, B. P. & Savage, B. D. 2009, ApJS, 182, 378
Wakker, B. P., Savage, B. D., Sembach, K. R., et al. 2003, ApJS, 146, 1
Wakker, B. P. & van Woerden, H. 1997, ARA&A, 35, 217
Wakker, B. P., York, D. G., Howk, J. C., et al. 2007, ApJ, 670, L113
Wakker, B. P., York, D. G., Wilhelm, R., et al. 2008, ApJ, 672, 298
Wang, F., Yang, J., Fan, X., et al. 2021, ApJ, 907, L1

Werk, J. K., Prochaska, J. X., Tumlinson, J., et al. 2014, ApJ, 792, 8
Westmeier, T. 2018, MNRAS, 474, 289
Westmeier, T., Brüns, C., & Kerp, J. 2008, MNRAS, 390, 1691
Weymann, R. J., Jannuzi, B. T., Lu, L., et al. 1998, ApJ, 506, 1
White, S. D. M. & Frenk, C. S. 1991, ApJ, 379, 52
White, S. D. M. & Rees, M. J. 1978, MNRAS, 183, 341
Winkel, B., Ben Bekhti, N., Darmstädter, V., et al. 2011, A&A, 533, A105
Wisotzki, L., Bacon, R., Brinchmann, J., et al. 2018, Nature, 562, 229
Wolfe, A. M., Turnshek, D. A., Smith, H. E., & Cohen, R. D. 1986, ApJS, 61, 249
Wolfe, S. A., Pisano, D. J., Lockman, F. J., McGaugh, S. S., & Shaya, E. J. 2013, Nature, 497, 224
Wolfire, M. G., McKee, C. F., Hollenbach, D., & Tielens, A. G. G. M. 1995, ApJ, 453, 673
Wotta, C. B., Lehner, N., Howk, J. C., et al. 2019, ApJ, 872, 81
Yoon, J. H. & Putman, M. E. 2013, ApJ, 772, L29
Yoon, J. H. & Putman, M. E. 2017, ApJ, 839, 117
Yoon, J. H., Putman, M. E., Thom, C., Chen, H.-W., & Bryan, G. L. 2012, ApJ, 754, 84
York, D. G., Adelman, J., Anderson, John E., J., et al. 2000, AJ, 120, 1579

A Appendix A

A.1 Chemical abundances

Table A1 — Chemical abundances

AGN name	l (°)	b (°)	$v_{\rm LSR}$ (km s^{-1})	log N(Si II)	log N(Si III)	log N(Si IV)	log N(C II)	log N(C IV)	log $n_{\rm H}$
2MASX-J01013113+4229356	124.9	-20.3	-231	13.71	13.40	13.21	14.59	13.50	-2.75
			-193	13.24	12.69	13.04	14.52	13.90	-3.80
AKN-564	92.1	-25.3	-432	12.79	13.39	13.21	13.90	13.40	-3.60
HS-0033+4300	120.0	-19.5	-202	...	13.15	13.18	14.03	13.98	-3.40
			-156	13.32	12.85	...	14.25	13.20	-2.62
			-119	13.78	13.05	...	14.86	...	-2.30
LBQS-0107-0235	134.0	-64.8	-268	...	12.63	12.67	13.20	13.65	-3.80
			-193	13.02	12.56	...	13.27	13.00	-2.60
			-103	13.14	12.66	...	13.76	13.44	-2.55
MR2251-178	46.2	-61.3	-257	12.45	13.03	13.11	13.35	13.81	-3.78
MRK335	108.8	-41.4	-413	12.18	12.49	...	13.32	...	-3.37
			-338	12.19	12.80	...	13.34	13.28	-3.73
			-294	...	12.58	...	...	13.29	-3.88
			-240	...	12.37	...	...	13.27	-3.96
			-121	11.98	12.54	...	13.50	...	-3.70
			-97	13.28	13.18	...	14.16	...	-2.94
MRK-509	36.0	-29.9	-300	12.15	13.20	13.10	13.58	14.07	-3.92
			-249	...	12.56	...	12.93	13.49	-3.96
MRK1513	63.7	-29.1	-294	...	13.01	13.09	13.39	14.02	-3.83
			-223	...	12.76	...	13.22	12.98	-3.58
NGC-7469	83.1	-45.5	-373	13.04	13.20	12.66	13.97	...	-3.23
			-334	13.45	13.62	13.21	14.12	...	-3.28
			-252	...	12.70	12.80	13.23	...	-3.85
			-185	...	12.40	12.85	13.12	...	-4.18
PG0003+158	107.3	-45.3	-431	...	12.40	13.06	13.12	...	-4.40
			-396	12.76	12.78	...	13.70	13.35	-3.09

Table A1 — Chemical abundances

			-327	13.25	13.19	...	14.10	...	-3.05
			-234	...	12.53	...	13.53	13.39	-2.90
			-360	...	...	12.78	...	13.76	-4.18[1]
PHL1811	47.5	-44.8	-358	...	12.61	12.67	...	13.78	-3.80
			-261	...	13.03	12.57	13.31	13.47	-3.93
			-213	13.70	13.94	12.88	14.38	...	-3.30
			-169	12.90	13.12	13.43	13.76	14.10	-3.30
PKS2155-304	17.7	-52.2	-275	...	12.22	...	...	13.56[2]	-4.15
			-138	12.73	13.18	12.62	13.78	13.48[2]	-3.50
Q2251+155	86.1	-38.2	-419	13.98	13.90	13.28	14.56	...	-2.98
			-372[3]	13.90[3]	14.53[3]	14.38[3]	14.78[3]	13.79[3]	-3.68[3]
			-326	13.54	13.90	13.65	14.49	13.74	-3.45
QSO0045+3926	122.3	-23.2	-380	12.86	13.14	...	14.15	13.12	-3.36
			-327	...	12.26	...	13.46	...	-2.71
			-246	12.78	13.36	13.14	13.87	14.02	-3.60
			-185	13.50	13.68	12.83	14.70	13.57	-3.21
QSO-B0026+129	114.6	-49.2	-187	...	12.46	...	...	...	-3.30
			-289	...	12.81	12.30	13.45	...	-3.03
			-241	12.78	12.73	...	13.54	...	-2.85
QSO-B2214+139	76.0	-34.2	-360	...	13.22	12.65	13.42	...	-3.18
			-327	...	13.01	...	13.26	...	-3.95
SDSSJ001224.01-102226.5	92.3	-70.9	-280	13.44	13.53	12.81	14.35	...	-3.15
			-243	13.22	13.53	13.48	13.96	14.17	-3.37
			-180	13.40	13.27	...	14.17	13.33	-2.91
SDSSJ004222.29-103743.8	115.1	-73.4	-147	...	12.82	...	...	...	-2.85
			-102	13.32	13.10	...	14.09	13.40	-2.83
SDSSJ225738.20+134045.4	85.3	-40.7	-421	...	13.00	...	13.70	...	-3.17

Table A1 — Chemical abundances

			-374	13.72	13.48	13.37	14.25	13.79	-2.86
			-329	13.33	13.48	13.25	14.17	13.80	-3.25
RXJ1230	291.3	63.7	119	12.68	12.68	...	13.88	12.83	-3.07
			299	13.06	12.77	...	14.01	12.77	-2.78
SDSSJ121640	278.9	68.4	215	12.58	12.55	...	...	...	-3.02
SDSSJ121850	276.9	71.5	110	13.14	13.25	...	14.05	...	-3.15
			151	12.94	12.93	...	14.10	...	-3.07
SDSSJ122018	281.6	68.3	208	13.00	12.85	13.10	...	...	-2.93
			273	12.87	12.72	...	...	...	-2.91
SDSSJ122102	269.2	76.8	143	13.38	13.52	...	14.15	...	-3.20
SDSSJ122312	280.5	71.5	172	13.10	12.85	...	13.80	...	-2.82
SDSSJ122317	281.1	71.1	188	12.80	12.58	...	13.59	...	-2.84
SDSSJ123304	293.1	62.0	125	12.71	12.59	12.68	13.35	13.30	-2.96
SDSSJ123426	290.6	69.9	199	13.00	12.95	...	...	...	-2.99
			239	14.34	14.50	...	...	...	-3.25
VV2006J131545	329.9	77.0	238	...	12.93	...	...	...	-2.68

(1) $\log n_{\mathrm{H}}$ from Si IV and C IV

(2) from Collins et al. (2004)

(3) No reliable measurement due to blending and low S/N

B Appendix B

B.1 Signal-to-noise

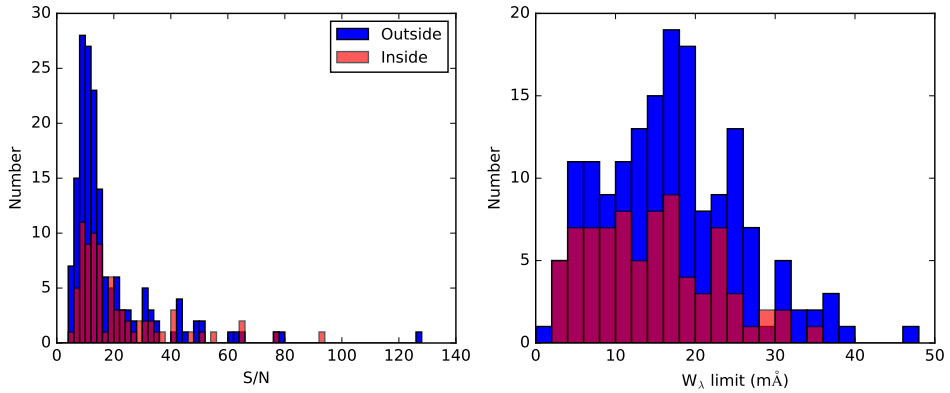

Figure B.1 — Information on the S/N of the COS spectra used in this study. *Left panel:* Distribution of the measured S/N per resolution element near Å 1240 for the COS spectra that are filament-related and those outside of filaments. *Right panel:* Formal 3σ detection limits for H I Ly α absorption in these spectra, based on the equation given in Tumlinson et al. (2002). We note that these values reflect the detectability of Ly α absorption as a function of the local S/N under idealised conditions (no blending, no fixed-pattern noise, perfectly known continuum flux).

B.2 Absorbers associated with galaxies

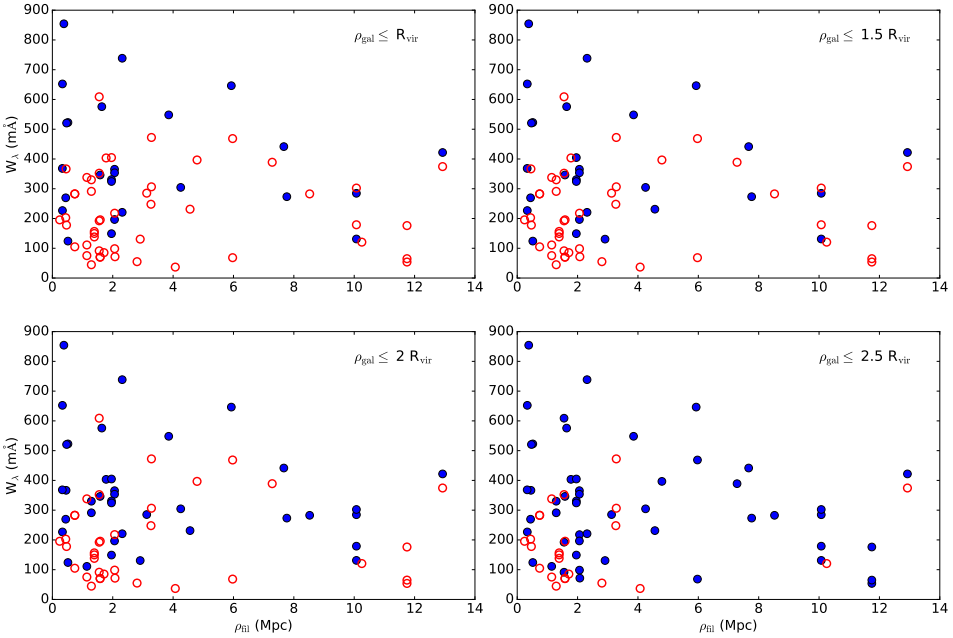

Figure B.2 — Same as Fig. 4.11, but now using different impact-parameter criteria, ρ_{gal}, for absorbers to be associated with a galaxy. Filled blue dots are absorbers associated with a galaxy, while open red dots are absorbers that are not.